Nanophotonic approaches to colourful solar cells and modules

Roberto Speranza

School of Science

Espoo 30.07.2018

Supervisor and advisor

Prof. Janne Halme

Aalto University
School of Science

Aalto University
School of Science

Aalto University, P.O. BOX 11000, 00076 AALTO
www.aalto.fi

Author Roberto Speranza

Title Nanophotonic approaches to colourful solar cells and modules

Degree programme Nanotechnologies for ICT's

Major **Code of major**

Supervisor and advisor Prof. Janne Halme

Date 30.07.2018 **Number of pages** 94 **Language** English

Abstract

The focus of this work was first to compile a literature review of the most relevant nanophotonic approaches proposed to realize structural colours for decorative and building-integrated solar cells and modules. Then, based on the gathered information, an alternative fabrication technique was proposed and experimentally investigated. From the literature review it was observed that the fabrication of colourful solar cells had been successfully achieved by integrating light filtering structures showing reflective structural colours (as opposed to light absorbing colours, e.g. dyes and pigments or metals), with different photovoltaic technologies. In general, the exploited light filtering mechanisms can be divided in multilayer interference, thin-film interference, diffraction gratins, plasmonic resonance and photonic bandgap in photonic crystals. The best results in terms of performance of the fabricated coloured devices had been obtained when the colouring structures had been integrated with standard, industrial crystalline silicon solar cells. On the other hand, advantages in terms of device thickness (amount of needed material) and colour purity had been obtained when the coloring structures had been used with a customized fabricated device (thin-film amorphous silicon solar cells, dye sensitized solar cells and perovskite solar cells). In the experimental part, a proof-of-concept was presented for the fabrication of a colour filter by inkjet-printing three dimensional photonic crystals on glass. A colour filter fabricated in this way could be used with all photovoltaic technologies, since it consist of a separate semi-transparent layer that can placed over any kind of solar cell. The structure was realized by inkjet printing, which allows flexible control over pattern design and accurate material deposition, allowing for the possibility of printing multi- and single-coloured patterns on a photovoltaic device. According to the preliminary results, further research would be needed to intensity of the coloured reflection and weaken the broad-band light scattering by the inkjet-printed photonic crystals.

Keywords colourful solar cells , structural colours , photonic crystals, building-integrated photovoltiacs , reflective colours

Aalto University
School of Science

Aalto-yliopisto, PL 11000, 00076 AALTO
www.aalto.fi

Tekijä Roberto Speranza

Työn nimi Nanofotoniikkaa hyödyntävät värilliset aurinkokennot ja -moduulit

Koulutusohjelma Nanotechnologies for ICT's

Pääaine **Pääaineen koodi**

Työn valvoja Prof. Janne Halme

Työn ohjaaja Prof. Janne Halme

Päivämäärä 30.07.2018 **Sivumäärä** 94 **Kieli** Englanti

Tiivistelmä

Työssä tehtiin ensin kirjallisuuskatsaus tärkeimpiin nanofotoniikkaa hyödyntäviin tapoihin tuottaa rakennevärejä koristeellisiin ja rakennuksiin integroituihin aurinkokennoihin ja -moduuleihin. Kerätyn tiedon perusteella esitettiin vaihtoehtoinen valmistustekniikka, jota tutkittiin kokeellisesti. Kirjallisuuskatsauksessa havaittiin, että värillisiä aurinkokennoja oli onnistuttu valmistamaan liittämällä aurinkennoihin ja -moduuleihin näkyvää valoa suodattavia ja heijastavia rakennevärejä, erotuksena esimerkiksi väriaineisiin, pigmentteihin, ja metalleihin, jotka absorboivat valoa. Kirjallisuudessa esitetyt valoa suodattavat ja väriä tuottavat mekanismit voidaan jakaa monikerrosinterferenssiin, ohutkalvointerferenssiin, diffraktioon hilarakenteissa, plasmoniseen resonanssiin, ja valon kiellettyyn energiaväliin fotonikiderakenteissa. Suorituskyvyn kannalta parhaat tulokset oli saatu, kun väriä tuottavat rakenteet oli liitetty tavallisiin teollisessa valmistuksessa oleviin kiteiseen piihin perustuviin aurinkokennoihin. Liittämällä väriä tuottavia rakenteita erikseen tätä tarkoitusta varten valmistettuihin kennoihin, kuten amorfiseen piihin perustuviin ohutkalvokennoihin, väriaineaurinkokennoihin tai perovskiittikennoihin, oli saatu etuja tarvittavien materiaalien määrässä ja värin puhtaudessa. Kokeellisessa osassa esitettiin alustavat tulokset värisuodattimen valmistamisesta mustesuihkutulostamalla kolmiuloitteisia fotonikiderakenteita lasille. Tällä tavalla valmistettua värisuodatinta voitaisiin käyttää kaikkien aurinkokennoteknologioiden yhteydessä, sillä se koostuu erillisestä puoliläpäisevästä kerroksesta, joka voidaan asettaa minkä tahansa aurinkokennon päälle. Rakenteen valmistukseen käytetty mustesuihkutulos mahdollistaa joustavan tulostuskuvion säätelyn ja tarkan materiaalien pinnoittamisen, ja soveltuu siten moni- tai yksiväristen kuvioiden tulostamiseen aurinkokennoihin ja -moduuleihin. Alustavien tulosten perusteella tarvittaisiin lisää tutkimusta rakenteen värillisen heijastuksen vahvistamiseksi ja sen aiheuttaman laaja-kaistaisen valon siroamisen heikentämiseksi.

Avainsanat Värilliset aurinkokennot, rakennevärit, fotonikiteet, rakennuksiin integroitu aurinkosähkö, heijastavat värit, mustesuihkutulostus

Preface

First of all, I would like to thank my supervisor, docent Janne Halme, for being a kind, capable and careful guide during the whole thesis work. There were many moments in which his experience helped me to overcome the various problems encountered during the work, allowing me to increase my scientific knowledge and improve my experience "on the field".

I would also like to thank all the members of the New Energy Technologies group for their kind assistance during my stay at Aalto University, as well as all researchers belonging to other research groups whose collaboration was fundamental to the success of the experimental work.

I would like to thank my referent Prof. Fabrizio Pirri and the Politecnico di Torino for giving me the opportunity to spend this period of study at Aalto University.

Finally I would like to thank my parents, my sister and all my friends for being, as always, a fundamental moral support during the whole time spent on this work.

Otaniemi, 30.7.2018

Roberto Speranza

Contents

1 Introduction

The sun is the biggest, clean primary energy source available on Earth in terms of power capacity. With its five million exajoules (1EJ = 10^{18}) reaching the planet every year, it could meet the global energy demand seven thousands times. Unfortunately, only a small percentage of the solar power can be actually harvested with the current technologies. For a long time, the idea of producing electricity through photovoltaic (PV) cells and module have established among the best possible solutions to face the problem of meeting the humankind's energy demand without having an impact on the environment. Well known is the urgent need to stabilise and then reduce the global greenhouse emissions, to achieve the goal of keeping the temperature rise well below 2°C, as established by the COP21 Climate Change conference in the Paris Agreement, in 2015.

The Renewable Energy Policy Network for the 21st Century (REN21) reported in its Renewables 2018 Global Status Report that 2017 was a record year for increase in the installed renewables power capacity, with an overall of 70% of net additions. A big role was played by solar PV, which installed power capacity accounted for 55% with respect to the previous year. This figures fits the trend observed for the last 10 years, in which the installed solar PV power capacity has been constantly increasing. This is the natural consequence of the fact that production of electricity through solar PV is becoming more and more cost-competitive with respect to the fossil fuels-based power generating systems. On the other hand, in the same report, the REN21 estimated that the renewable share of the global electricity production at the end of 2017 was 26.5% of which only 1.9% from solar PV. It is clear then how new solutions aimed to increase this percentage, boosting even more the positive trend of installed solar PV power capacity are needed to allow this power production technique to express its true potential.

One of the crucial limitations of solar cells and modules is their power conversion efficiency. The range of reported values in the market is various and it goes from around 10-20% for domestic panels to efficiencies between 20% and 30% for more expensive products. As an example, solar panels with cells showing a maximum efficiency of 24.3% are commercialized by SunPower^{TM} (2018). The correlation between costs and high levels of efficiencies has always been a limiting factor for the large scale implementation of solar panels. Efforts have been made to study different materials and technologies to realize less expensive solar cells, e.g. thin-film solar cells, perovskite solar cells and dye-sensitized solar cells, but the record efficiencies of the well established silicon-based panels remain still unbeaten.

One way to increase the power that can be produced by solar panels is to increase their efficiency but apparently this cannot be done without increasing their price. On the other hand, if the efficiency remains the same, but the number of panels increase, more electricity will be produced. This way of thinking is clearly oversimplified but still gives a clue about what is one of the directions that in the last few years has been investigated to allow to achieve a wider degree of solar PV integration.

Around one third of the global final energy consumption can be connected to buildings which is why lately, the possibility of increasing their energy efficiency

has attracted more and more attention. In this scenario, solar panels and modules can represent a huge breakthrough. By integrating them within the buildings, electricity can be produced near the end user, without any transmission losses and costs, contributing in a clean way to the energy efficiency of the construction. Naturally this idea does not strike as something new since for years solar panels have been installed on buildings roofs all around the world. In this case, one talks about building-applied photovoltaics (BAPV). The turning point can be seen if one starts to think about solar modules as multifunctional objects, playing the role of both energy generators and building materials. This is the case of the so called building-integrated photovoltaics (BIPV).

At the present moment, in the usual photovoltaic installations on buildings, the panels are applied mostly on roofs, combining the need for an optimized position and orientation (to maximize illumination) to the need of making them visible as less as possible. In this scenario, PV panels are viewed by architects as an additional feature to be considered later in the design or renovation process because they are not enough visually appealing. Moreover, there can be protected areas where standard looking PV are even forbidden to preserve the architectural style of the location. As a matter of fact, commercially available PV are usually lacking of variety in sizes, shapes and more importantly appearance (colour and textures). As a consequence, the possibility of integration for solar panels is drastically reduced. Problems related to the lack of building codes and standards regulating the use of BIPV as materials on the buildings façades also represents an impediment in this direction, as well as the fact that the low number of projects involving BIPV lead to higher costs of production and installations.

Unfortunately, all these barriers can prevent solar modules to be considered as construction materials for the buildings façades, acting as multifunctional elements and substituting materials as glass, stone or marmor. Naturally, this substitution has to be cost-effective, providing that a customizable BIPV product has a cost that is comparable with one of the corresponding substituted materials. With a higher requests of these multifunctional elements, their cost could decrease and becomes even lower than most of the material often used for building façades. [1].

Nevertheless, in recent times, PV panel manufacturers are trying to introduce in the market a higher degree of freedom in terms of the appearance of their products, and different trends of PV integration in roofs and façades have been observed. One of these is the realization of coloured solar façades. The possibility of realizing coloured PV panels represent a mandatory requirement when it comes to integrating them in building façades. This comes from the idea of having the active materials on the sides of the building without being visible or recognizable from the dummy elements (the elements not producing power).

In the Product Overview for Solar Building Skins released in 2017 by the Swiss BIPV Competence Centre (SUPSI) and by the Solar Energy Application Centre (SEAC), different customization techniques, proposed by different companies, were reported. In general, all these techniques consider the integration in the usual solar cell design of a colouring layer, and can be divided depending on where this layer is implemented, within the cell. One option is to change the colour of the cell by

engineering the thickness of the anti-reflecting coating, setting the reflection minimum to the wavelength corresponding to the desired colour. Another option is to change the colour of the front glass, which can be done through different procedures such as the application of a ceramic paste before tempering the glass, realizing digital ceramic-based printing, sandblasting the glass surface to generate a milky white appearance or even applying a multi-layer reflective coating on the glass. Finally the cell colour can be changed inserting a foil with the desired colour appearance inside the module.[2]

In recent years, thanks to the progress in the field of material manipulation at the nanoscale, innovative approaches have been proposed for the fabrication of colourful solar cells and modules. In all these cases, the peculiar optical behaviour of nanostructures with respect to light propagation and interaction is exploited to realize the so-called structural colours, which are colours that arise not from the usual light absorption processes observed in pigments, dyes and metals, but from the specific nanoscopic structural conformation of materials.

Based on this scenario, in the first part of this work, different nanophotonic approaches used for realizing reflective colours for decorative solar cells and modules were investigated, compiling a literature review of the most relevant techniques and solutions. The review will be mainly technical, focusing on the photonic principles applied, the realized optical structures and the used materials and fabrication techniques. Then, based on the information gathered from the literature review, an experimental procedure realizable by inkjet printing in the New Energy Technologies group's lab in Aalto University was identified. It was proposed to investigate the possibility of realizing colourful solar cells by exploiting the colour filtering properties of inkjet-printed three dimensional photonic crystals. Then an experiment was carried out to give a first proof-of-concept of the proposed solution: an optical filter was realized by inkjet printing and the optical and electrical characteristics of the solar cell integrated with the fabricated filter were investigated.

2 Theory background

2.1 Solar cells

How they work

A solar cell is an electronic device that is able to convert the energy carried by the radiation emitted by the sun into electric power. All solar cells are characterized by the presence of a so-called photoactive material or layer, which is the main part of the cell where sunlight is absorbed. Different types of cell have been realized and studied using different materials as absorbing layers. In general, in the active layer the solar radiation cause a chemical reaction that produce a pair of negative and positive charges, which will then contribute to the generated electrical current. So the energy carried by the radiation is transferred to the charge carriers and then dissipated in the external circuit connected to the cell. In figure 2.1.1 is shown a schematic representation of the general structure of a solar cell.

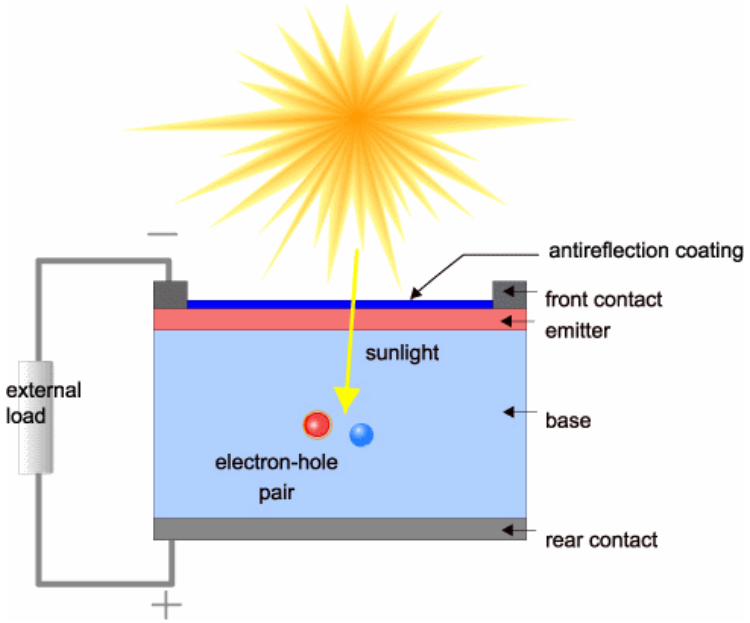

Figure 2.1.1: Schematic representation of the general structure of a solar cell. (figure from [3])

Sunlight is absorbed by the photoactive layer, which is usually represented by the junction between two materials (base-emitter) and opposite charge carriers pairs are formed. These carriers are separated and then collected by the front and rear contact, to which the external load is connected. A potential difference appear at the contact of the cell and the generated carriers contribute to the current flowing through the load, so that electrical power can be produced. The conversion process can then be divided in carrier generation, separation and and collection and it remains the same regardless the technology or materials used in different types of solar cells.

The light absorption process is strictly connected to the energy of the incoming radiation. A photon can be absorbed if its energy is higher than the energy band

gap of the photoactive material of a certain cell. In semiconductor-based solar cells, this band gap is the energy difference between conduction and valance band while in dye-sensitized solar cells, e.g., this is the difference between the excited state and the ground state of the dye particles. The charge separation is modelled by the carrier lifetime which is the time interval before the carriers will recombine with their opposite counterparts. For this reason a potential must act as a separating force for the generated charge. Usually, this role is played by the electric field existing at the junction between p-doped and n-doped regions in semiconductor-based solar cells. The generated charges are then collected at the electric contacts.

The external quantum efficiency (EQE), sometimes also called incident photon to converted electron (IPCE) ratio, is the parameter that model the capability of a solar cell to absorb light generating charge carriers. It is the ratio between the number of carriers collected by the cell to the number of incident photons with a given energy. It depends on the wavelength of the incoming light and it is different for each different type of solar cells. In figure 2.1.2 is shown the EQE reported for a commercially available monocrystalline solar cell compared to the AM1.5G standard solar spectrum (cut at 1200 nm), which is one of the international standards used to compare different photovoltaic devices. It considers an integrated sun power over the whole spectrum of 1000 W/m^2[4].

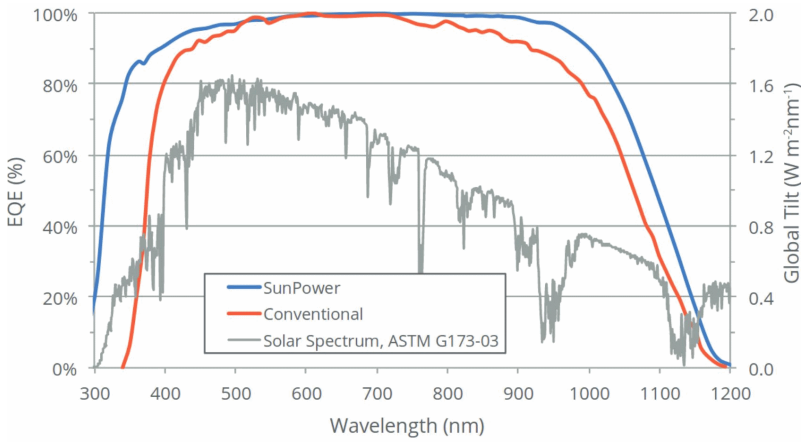

Figure 2.1.2: External quantum efficiency reported for a monocrystalline silicon solar cell compared to the AM1.5 standard solar spectrum (figure from [5])

Below a certain photon energy (or below the corresponding photon wavelength), the cell is not able to absorb light anymore because the energy of the photon is lower than the band gap energy of the absorber material. In addition to this, the EQE of a cell varies depending on the recombination phenomena within the cell and on the optical losses caused, e.g., by transmission and reflection of light within the additional layers added on the surface of the active material (anti-reflective coatings, front protecting glass etc.).

If the optical response of a solar cell can be represented with its EQE, the electrical performances and parameters are extracted from its current-voltage (I-V) characteristic. A solar cell is usually modelled as a light generating diode, superposing

to the usual diode equation the light generated current. The solar cell equation then becomes:

$$I = I_0[e^{\left(\frac{qV}{kT}\right)} - 1] - I_L \tag{1}$$

where I_0 is the diode reverse bias saturation current, V is the voltage, k is the Boltzmann constant, T is the temperature and I_L is the photogenerated current. From the I-V curve all the fundamental parameters characterizing the device are extracted. In figure 2.1.3 the typical I-V curve of a solar cell is reported.

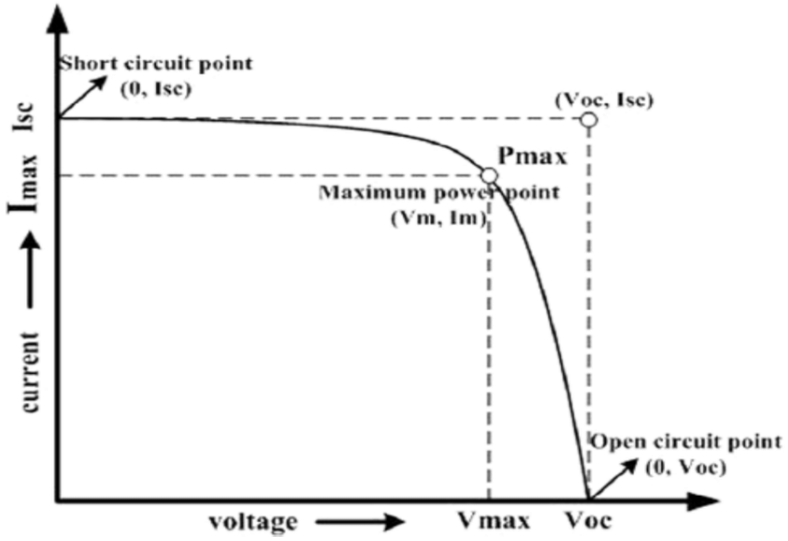

Figure 2.1.3: Typical I-V characteristic of a solar cell. The most important parameters characterizing a solar cell are indicated (short circuit current I_{sc}, open circuit voltage V_{oc}, maximum power point P_{max}).(figure from [6])

In the figure, the most important parameters characterizing a solar cell are indicated. The short circuit current I_{sc} is the current that flows when the cell is short circuited and the voltage across the cell is null. From the solar cell equation it can be seen that when the voltage across the cell is zero, the short circuit current is equal to the light generated current. This is not exactly true because, in this equation, the parasitic resistive effects are not yet considered. Nevertheless, usually the difference between I_{sc} and I_L is very low and these two current are often used interchangeably.

Often, instead of this value, to characterize the cell the short circuit current density is considered, reported in milliampere per square centimetre (mA/cm^2), so that two cells with different collecting areas can be compared. This value determine the highest current that can be generated by the cell and is mainly related to the optical processes and properties of the cell being a function of the incoming light spectrum and of the quantum efficiency of the cell. The short circuit current density can be calculated as:

$$J_{sc} = q \int_{\lambda} \Phi(\lambda) EQE(\lambda) d\lambda \tag{2}$$

where Φ is the photon flux of the incident light and EQE is the external quantum efficiency of the cell.

The other important parameter to characterize different solar cells is the open circuit voltage, which is the maximum voltage that can be generated under illumination and is the potential across the cell when it is non connected (zero current). By putting the solar cell equation equal to zero, an equation for the open circuit voltage V_{oc} can be calculated:

$$V_{oc} = \frac{kT}{q} \ln(\frac{I_L}{I_0} + 1). \tag{3}$$

The light generated current and the saturation current then influences V_{oc}.

In figure 2.1.3 the maximum power point is also indicated which is the point where the current (I_m) and the voltage (V_m) have such values that the cell is generating the maximum possible power. These values are used to calculate the so-called fill factor of the cell (FF):

$$FF = \frac{I_m V_m}{I_{sc} V_{oc}}. \tag{4}$$

which is a parameter often used to determine the quality of the cell performance since it tells how much the cell is different from its ideal counterpart, since it is the ratio between the rectangular area determined by I_m, V_m and I_{sc}, V_{oc}. Usually the fill factor can range from 0.5 to around 0.8, the latter being the case of silicon based solar cells.

Finally the most important parameter to compare different cells is the power efficiency η which is the ratio between the maximum power that can be generated by the cell and the power of the incoming light illuminating the cell. Usually it is expressed as a function of the parameters described before:

$$\eta = \frac{V_{oc} I_{sc} FF}{P_{in}}. \tag{5}$$

For efficiency estimations the incoming power is considered to be 1000 W/m^2.

The theoretical model presented here can be completed considering the parasitic resistive effects caused by the series and shunt resistance (R_s and R_{sh}). The circuit model of a solar cell, considering also these effects is represented in figure 2.1.4.

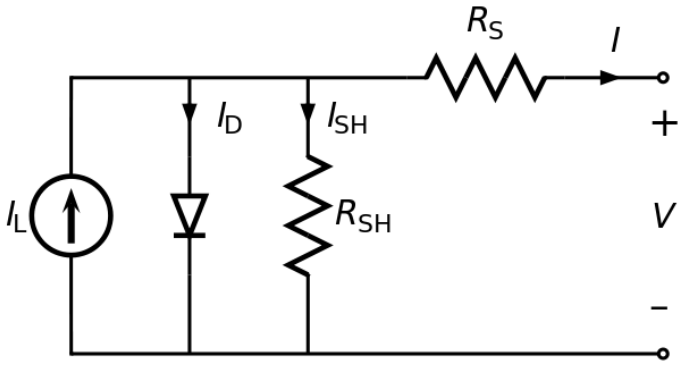

Figure 2.1.4: Schematic representation of the circuit of a solar cell. The cell is represented as the combination of the diode with a current generator accounting for the photogenerated current and the series and shunt parasitic resistances. (figure from [7])

These parasitic effect are mainly caused by the bulk resistance of the active material, the bulk resistance of the metal electrodes and the contact resistance between the previous two, when it comes to series resistance. The shunt resistance effects are mostly due to the presence of defects or impurities that may cause current leakage within the cell. The final cell equation considering both R_s and R_{sh} is:

$$I = I_L - I_0[e^{\left(\frac{q(V+IR_s)}{kT}\right)}] - \frac{V + IR_s}{R_{sh}} \tag{6}$$

There are different factors that can affect the performances of a solar cell (e.g. temperature, parasitic resistances, light intensity etc.). On the other hand, this work is focused on colourful photovoltaics so the most relevant in this case is the one related to the change in the cell performance caused by the addition of a colouring layer or structure of any sort. In common solar cells, usually an anti-reflective layer is added to reduce as much as possible the amount of light reflected by the cell, maximizing the quantity of light converted to electricity. The effect of this layer in terms of appearance, is that the cells look usually black or dark blue.

To change the colour af a cell, ideally, an element must be added with the function of optical filter, reflecting a certain amount of the visible part of the solar spectrum and allowing the rest to reach the active layer of the cell and be absorbed by it. The effect of such a layer or structure will be simply optical, since only the amount of light reaching the cell will change. The first parameter to be affected is the EQE of the cell since the amount of photons being absorbed will be lower. If the EQE of a cell is known, the effect of a colouring layer can be theoretically calculated. The new EQE will be:

$$EQE_{col}(\lambda) = T(\lambda)EQE_{cell}(\lambda) = [1 - R(\lambda) - A_{loss}(\lambda)]EQE_{cell} \tag{7}$$

where EQE_{col} is the external quantum efficiency of the coloured cell, $T(\lambda)$ is the transmittance of the colouring layer and EQE_{cell} is the EQE of the standard cell. The transmittance $T(\lambda)$ determine the amount of light that pass through the filter reaching the cell, and it can be calculated as:

$$T(\lambda) = [1 - R(\lambda) - A_{loss}(\lambda)] \tag{8}$$

where $R(\lambda)$ is the total hemispherical spectral reflectance of the colouring filter and A_{loss} is the parasitic absorption loss caused by the same colour coating.

The main consequences of the addition of a colouring coating/structure will be then to decrease the light generated current I_L. From the previous equations it is clear how this variation will affect the short circuit current the most. In fact, for small values of series resistance, the I_{sc} is usually equal to I_L. This is confirmed by the equation used to calculate the short circuit current of a solar cell (2). The variation of the EQE of the coloured cell will affect roughly proportionally the J_{sc}. The effect on the other parameters, e.g. V_{oc}, FF and consequently cell efficiency, will come indirectly from the photocurrent variation (equations 3, 4 and 5). For this reason, it is common tendency to discuss the effect of the colour one the cell performances principally in terms of light generated current, with the J_{sc} being the reference parameter.

Photovoltaic technologies

From the mid 1950's, when the construction of the first silicon solar cell was reported by the Bell Laboratories, up to now, a constant effort was put in the development of photovoltaic devices that could combine a high level of power efficiency with factors such as performance stability, time durability, production cost effectiveness and so on. Different technologies were studied and developed and, based on the used materials and the market penetration level, they can be divided into three groups.

The first group is the one that include the so-called first-generation solar cells. This is the class of solar cells that dominates the photovoltaic markets with more than 80% of the total installed solar panels falling in this category, all based on the use of silicon as photoactive material. The choice of silicon as light absorbing materials comes from the combination of the fact that it is a material whose properties and manufacturing processes are well known thanks to its large use in the electronic device industry, and from the fact that until now, it has provided the highest level of power conversion efficiency. Depending on the crystallinity of the material, three types of cell have been developed. The traditional and more efficient solar cells are the one based on thin wafers of mono-crystalline silicon (mono c-Si). The latest reported efficiency for mono c-Si solar cells is 26.7% [8]. On the other hand, these high efficiency cells are the most expansive to produce with the high cost coming from the high level of purification needed in the fabrication process. Less expansive are poly-crystalline (poly c-Si) solar cells where, with a less complex manufacturing process, silicon wafers with a lower level of purity are produced. The record efficiency reported for these cell is to 22.3[8].

The second generation of PV technologies is the one that include the so called thin-film solar cells. These devices use as active layers, materials different from crystalline silicon, with the goal of realizing devices that need less material to still achieve high level of efficiency. Usually, direct band gap semiconductors are used (opposed to crystalline silicon that have an indirect band gap), such as amorphous silicon, cadmium telluride (CdTe), copper-indium-selenide (CIS) and copper-indium-gallium-diselenide (CIGS). The direct band gap allows to achieve higher absorption coefficients than crystalline silicon, reducing the amount of material needed for the cell production and consequently reducing the manufacturing costs. The efficiency levels for thin-film solar cells range between around 10% for amorphous silicon up to 21.7% for CIGS cell[8]. The drawbacks of second-generation solar cells is the fact that often some of the used materials are becoming rare and more expensive or highly toxic which is the case of indium and cadmium, respectively.[9]

The third generation of solar cells include all the technologies that emerged in recent times and are attracting more and more attention from the scientific community and PV industry. The goal is to substitute the use of semiconductors as absorbing material, exploring the use of the combination of organic and inorganic materials as well as nano-structured materials, trying to find a way of producing photovoltaic energy with reduced costs as well as the level of toxicity, the main problems showed by the previous generation of PV. In this category fall dye-sensitized solar cells (DSSC), where the photon absorption is carried out by an organic or metal-organic

dye with which a nanoporous conducting structure (usually titanium dioxide) is infiltrated. The energy generation simulates the photosysthesis process used by plants to convert solar energy into chemical energy. Another types of solar cells that has attracted more and more attention in recent times are perovskite solar cells. Here the active layer is represented by a perovskite structured compound which usually is a organic-inorganic material based on lead or tin-halide. To be mentioned in this category there are also organic or polymer solar cells, where the active layer is made by the combination of completely organic acceptor and donor materials up to more futuristic solutions involving nanostructured materials like quantum dots. The reported efficiencies for third-generation solar cells range from 12.2% for organic cells, 11.9% for DSSC up to 20.9% for perovskite solar cells[8], but these technologies are not ready to be inserted in the market yet, because of problems like lifetime duration and operational stability.

2.2 Drop-On-Demand inkjet printing

Inkjet printing is the most commonly used technique to transfer digital readable images or text onto physical substrates as paper or plastic. In recent times, this technique have found additional applications as a material deposition techniques in the fabrication of electronic and optical devices (e.g. organic transistors, light emitting diodes, ceramics, solar cells).[10][11] This is due to the fact that by inkjet printing it is possible, at low cost, to deposit on ideally any substrate, single or multiple layers of material, realize patterns with easily controllable designs and reduce the material waste to a minimum. Furthermore, it represents a deposition technique suitable to be scaled to large area manufacturing.

Liquid phase materials are used as inks. An ink is usually prepared dissolving the material that need to be deposited into a liquid solvent but sometimes also hot melt solid inks can be printed as well as UV-curable ink made of UV reactive monomers. Depending on the way by which the ink is deposited on the substrate, different inkjet printing techniques can be defined. If the ink is ejected in the form of a continuous stream of droplets one talks about continuous inkjet. In the case of drop-on-demand (DOD) inkjet, instead, it is possible to independently control the ejection of each single drop of ink. This is usually the preferred technique for material deposition in electronics since it gives an higher control on the amount of deposited material and it is also the most relevant for the objectives of this work, since a DOD piezoelectric inkjet printer will be used as a deposition instrument.

The DOD piezoelectric inkjet technique is based on the presence of an piezoelectric transducer able to react with a deformation when subjected to an electric potential variation. In figure 2.2.5 it is represented the schematic representation of the drop formation in a piezoelectric DOD inkjet printer. The deformation of the piezoelectric element can be controlled by the electric signal applied to it. When a positive potential is applied, a deformation is induced in the piezoelectric element that increases the pressure inside the chamber or cavity. The ink is pushed out of the nozzle and the ink drop start to form under the effect of the surface tension of the liquid. Then by reducing the potential, the piezoelectric element returns to its rest

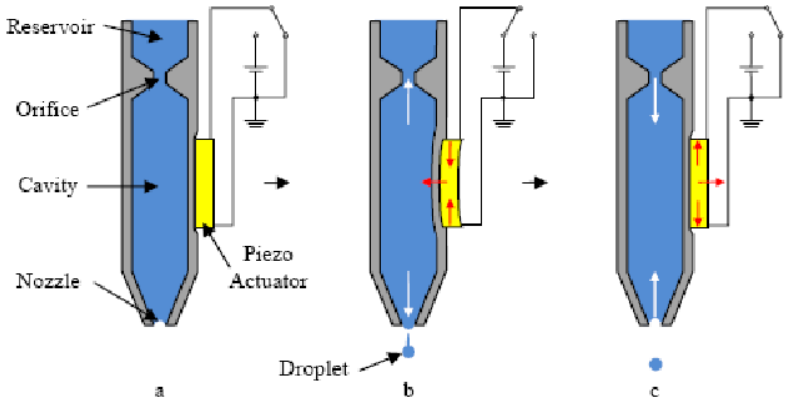

Figure 2.2.5: Schematic representation of the drop formation in a piezoelectric DOD inkjet printer. The applied potential difference causes the deformation of the piezoelectric element that change the pressure inside the chamber causing the drop ejection (figure from [12])

position, allowing the cavity to refill. When low viscosity inks are printed, controlling the electric potential applied to the piezoelectric transducer, it is possible to impose in the idle time (when the nozzle is not firing) a negative deformation so that the pressure inside the cavity will avoid the ink to drop out of the nozzle (meniscus formation). Once the drop is ejected, it falls on the substrate driven by the gravity force. When it touches the substrate, the droplet can assume different behaviours, influenced by factors such as the distance between the nozzles and the substrate and the substrate contact angle. In figure 2.2.6 a schematic representation of these behaviours is shown. After the impact, the drop start to spread under the influence

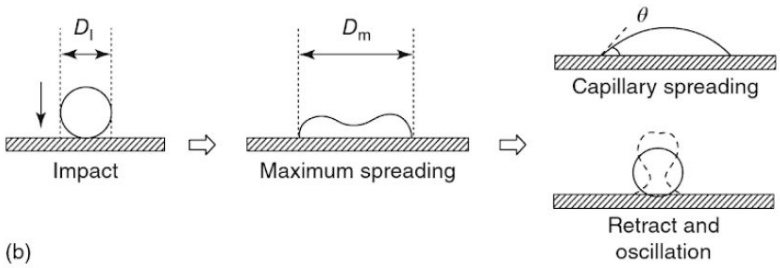

Figure 2.2.6: Schematic representation of the drop behaviour at the impact with the substrate. (figure from [13])

of inertial force, reaching the maximum spreading. Then the capillary forces start to dominate and the drop starts to spread according to the substrate wettability with respect to the ink. Between these two processes, the drop is subjected to oscillations as depicted in the third stage in the picture (retract and oscillation).

As soon as the drop is ejected, the drying process starts. Nevertheless, normally the solvent evaporation is a much slower process with respect to the impact stages explained before. For this reason, it can be assumed that the evaporation starts after the drop has reached its equilibrium spreading area. Then the drying process depend both on the ink composition (surface tension, viscosity) as well as the ink-substrate

wettability. For this reason, a correct characterization of the printed ink allows to determine and control the ink behaviour on the substrate. It is also needed to understand the printability of the ink, since different printers may have different requirements, in particular in terms of viscosity and surface tension, since these parameters affect the drop formation at the nozzle (see figure 2.2.7).

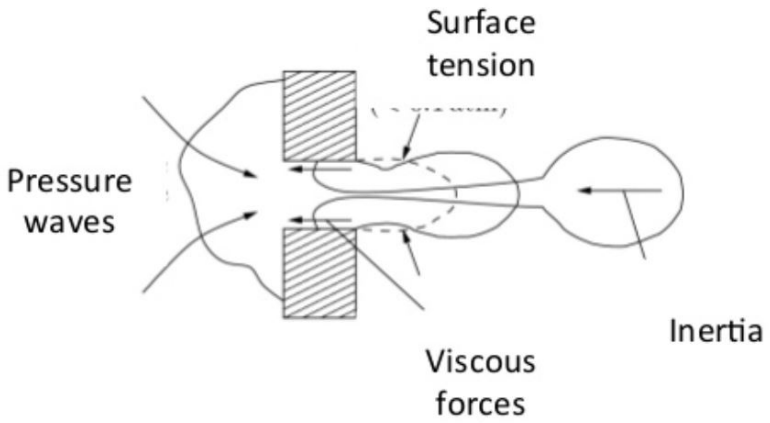

Figure 2.2.7: Forces involved in the drop formation at the cartridge nozzle. The ink surface tension gives the drop its rounded shape. A too high value of this parameter may cause a drop formation to be more difficult since a higher force will be needed. At the same time, the viscosity of the ink must be controlled as viscous forces are important in the last stage of the drop ejection (figure from [14])

2.3 Structural colours

The perception of colour that we have is the result of an electromagnetic radiation stimulating the cone cells of our eye, producing a specific reaction, directly correlated to the wavelength(s) of the light. In general, the colour of objects depends on the portion of the visible light spectrum that is reflected and reaches our eyes with the rest being absorbed by the material. This is what happens in pigments, dyes and metals, where the energy carried by the illuminating radiation is transferred to the electrons that shift to an excited state, with the process determining the colour depending on the chemical composition of the material. In this case, the absorbed portion of the light spectrum can be considered lost, unless it serves some other specific purpose, like generating charge carriers in a solar cell.

On the other hand, there are cases when the visual appearance of an object do not depend on its chemical composition but is related to the effect of specific nanoscopic structural features. This is the case of what is usually called structural colours. Many are the example of these phenomena found in nature (e.g. peacock feathers and morpho butterfly wings [15]). In all these cases, the particular conformation of a certain structure causes inhomogeneity in the refractive index, leading to the appearance of fundamental optical phenomena like refraction and diffraction of light as well as interference and scattering processes. In figure 2.3.8 are shown some examples where in nature the colour is related to these mechanisms. It can be

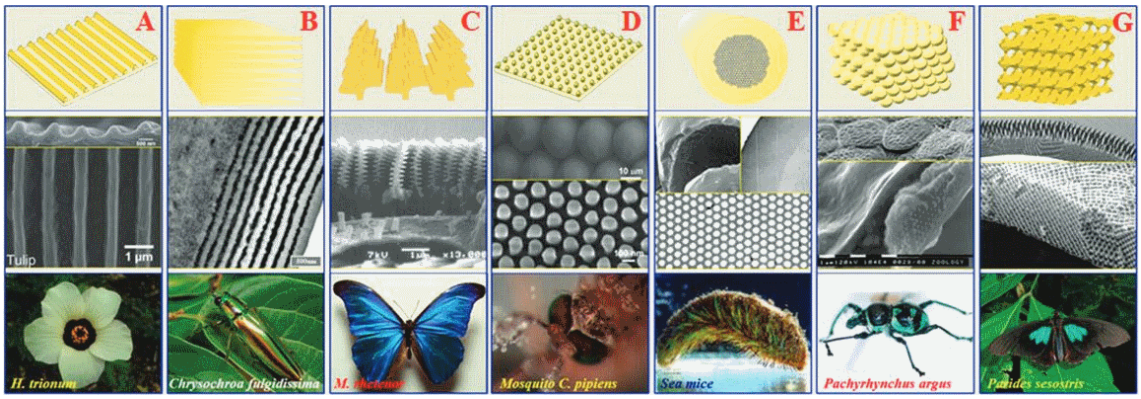

Figure 2.3.8: Examples of structural colours in nature. The photographs are associated with the scanning electron microscopic images (SEM) showing the characteristic structure of each species(second row), represented schematically in the first row. (figure from [16])

seen how in all these cases, the colour is associated with a particular structural conformation, showing a high level of symmetry. Thanks to the advances in the field of nanotechnology, now it is possible to manipulate the matter at the nanoscale, and consequently, a high number of research studies are focusing on nano-structures capable of moulding the flow of light as shown by nature.

In general, the mechanisms of structural colors are categorized into several optical phenomena such as thin-film interference, multilayer interference, diffraction grating and photonic crystals. In the following section, the most relevant nanophotonic approaches proposed to realize colourful solar cells by means of structural colours will be analysed.

3 Literature review

In the previous sections, the growing interest in colourful solar cells and modules for building-integrated photovoltaics was introduced. In this direction, structural colours represent a promising route to achieve an higher degree of design freedom for solar panels, without the optical losses derived by usual colouring techniques (pigments, dyes). In this section a literature review will be presented, giving an overview on the most relevant examples of PV applied colour production techniques based on the manipulation of matter at the nanoscale. The goal is to understand what are the most promising routes focusing on how each technique influence the solar cell performances and what is the degree of scalability for a future integration in industrial solar cell production. The review will be mainly technical, focusing on what materials have been used, what are the structures and how they have been fabricated.

Moreover, it is in the interest of this work to build a scientific background on nanophotonic approaches for colourful solar cells in order to identify the possibility of realizing structural colours by inkjet printing, which will be the main focus on the experimental part of this work.

3.1 Double-layer anti-reflective coating on m-Si solar cells

The most common approach to select the colour of a solar cell is by changing the thickness of the anti-reflection coating (ARC). This layer is usually optimized to reduce the portion of the light spectrum that is reflected from the cell, increase the light absorption and achieve surface passivation [17]. For industrial mass production of silicon solar cells, usually a layer of hydrogenated silicon nitrate $SiN_x : H$ is deposited on the front surface. [18] The effect is the well known dull blue appearance.

In this case, the colour is the result of the interference phenomena to which light undergoes when traveling through the layers composing the cell. Each layer, made of a different material, has a different refractive index so the light will travel with different speed, according to the Fresnel equations.[19]. Changing the thickness and the refractive index of the ARC the perceived colour of the cell can be selectively changed.[20] However this method is not very efficient since it reduces significantly the short circuit current J_{sc} of the cell. For this reason an alternative have been proposed and it involves realizing a double anti-reflective coating (DARC) depositing an additional layer of material, with a different refractive index, on top of the already existent ARC. Then modulating the thickness of this second layer the perceived colour of the cell is varied.

In 2013 Minghua Li et al. reported this method achieving grey yellow, purple, deep blue and green solar cells. The efficiency of the coloured cells were comparable to the standard cell with the single ARC.[21] The structure under study is reported in Figure 3.1.1:

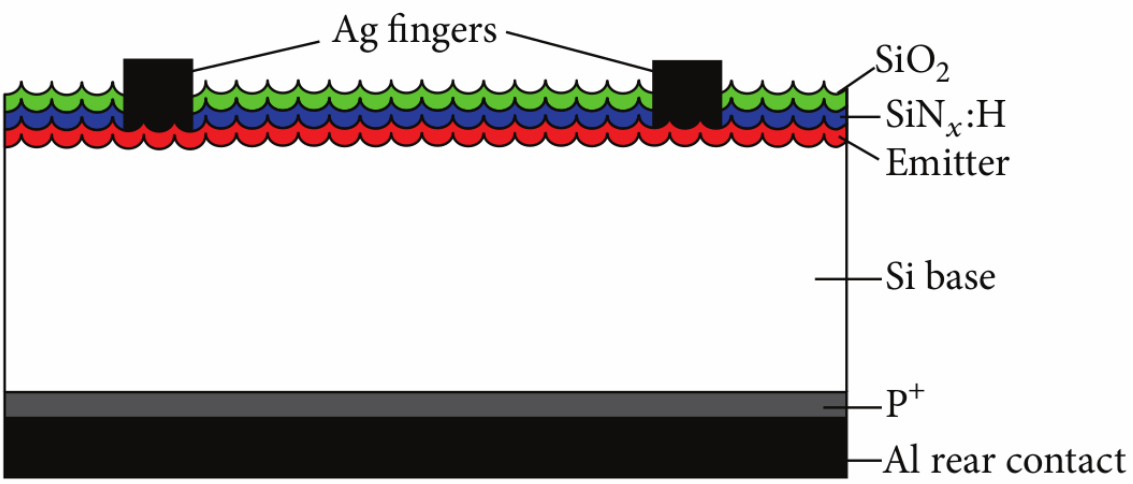

Figure 3.1.1: The schematic representation of the proposed design is showed. To the common design of a silicon solar cell, a DARC is added, composed by a layer of $SiN_x : H$ combined with a layer of SiO_2. (figure from [21])

In this case, a multicrystalline silicon (mono c-Si) cell was studied, with a dimension of 156 x 156 mm^2. First the structure depicted in figure 3.1.1 was simulated by Monte Carlo ray tracing method [22], and the reflectivity of the structure with and without the additional SiO_2 layer was calculated. Furthermore the the short-circuit current density (J_{sc}) was calculated.

In figure 3.1.2a and 3.1.2b the expected perceived colour and the J_{sc} as a function of the thickness of the covering layer(s) are reported. In figure 3.1.2a the results for the structure with the single ARC show that there is a peak in the current density when the $SiN_x : H$ layer has the optimum thickness of 80 nm, with a maximum current density of 35 mA/cm^2. For this value it is also clear how the perceived colour of the cell correspond to the typical blue of mono c-Si cells. When deviating from this value, a consequent decrease in the J_{sc} is observed. In particular, the maximum relative change is observed for a thickness of 200 nm, where the current density decrease to 31.7 mA/cm^2, with a relative loss of around 10%. This confirm that to change the colour of the solar cell by varying the thickness of the single ARC is not the best solution. In fact, figure 3.1.2.b shows that a DARC can allow to obtain colours like green and deep blue with small losses in the J_{sc} (up to 0.5 mA/cm^2) when the thickness of the SiO_2 is close to 250 nm. Moreover, a slight boost in the current density is observed with thicknesses between 50 and 150 nm, yielding colours like grey yellow, red and purple. In this case, the structure with the DARC was simulated with the bottom layer fixed to $SiN_x : H$ (thickness = 80 nm, n = 2.1). The refractive index of the SiO_2 layer is n = 1.46.

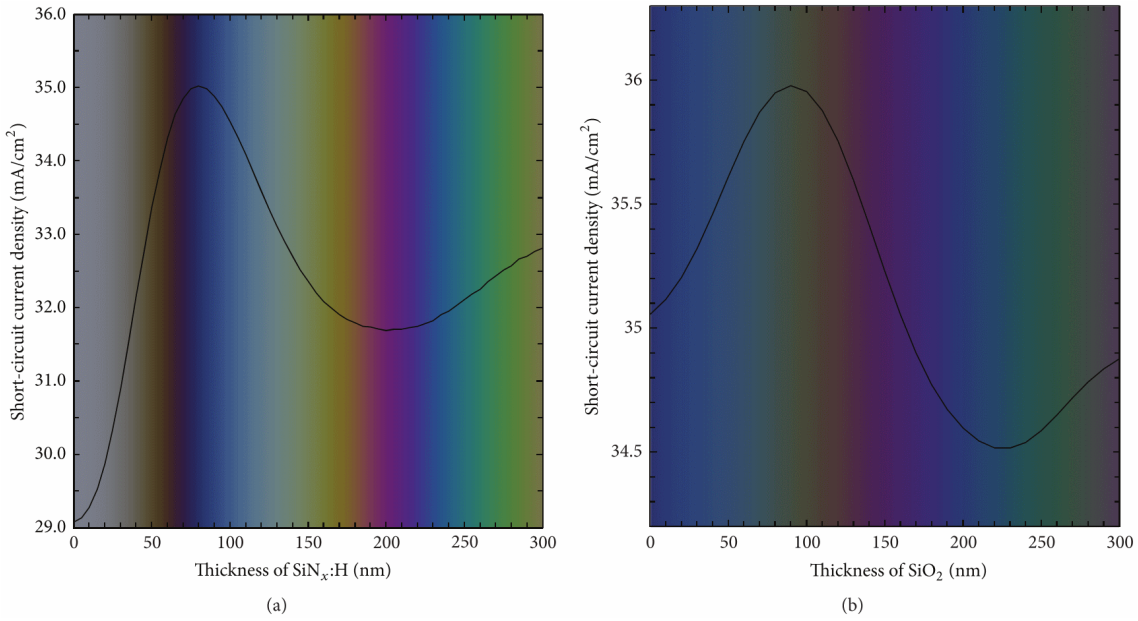

Figure 3.1.2: The short circuit current variation with respect to the coating thickness is showed, combined with the corresponding theoretical perceived colours for the case with a standard $SiN_2 : H$ ARC (a) and for the case with the $SiO_2/SiN_2 : H$ DARC (b) (figure from [21])

The simulated structure (figure 3.1.1) was then realized on an industrial p-type mono c-Si wafer with dimension 156 mm x 156 mm, with a wafer resistivity between 1 and 3 Ωcm. The emitter was realized with a standard $POCl_3$ diffusion in a quartz tube, achieving a sheet resistivity of 80Ω/□. Then the $SiN_2 : H$ coating was realized with PECVD, controlled to keep the refractive index to n = 2.1 and its thickness to 80nm. The metalizations was realized by screen printing. To form the additional AR layer, a SiO_2 was deposited on top of the fabricated cell by electron beam evaporation. The top metalizations must be protected during this phase.

The $SiO_2/SiN_2 : H$ double layer is reported to be one of the best solution for coloured solar cells using DARC, because of the good mechanical, structural and dielectric properties of the two materials. The realized $SiO_2/SiN_2 : H$ structure does not need further high temperature treatments or encapsulation. Moreover, when the silicon nitrate layers are deposited, a tensile strength can appear, while silicon dioxide exhibits compressing force. This could reduce the stress between the two layers. Also, SiO_2 has a smaller thermal expansion coefficient than silicon, so the interface stress in $SiO_2/SiN_2 : H$ is smaller than that of $SiN_2 : H/SiO_2$[23]. Finally, it is reported that $SiN_2 : H$ and SiO_2 have good thermal stability[24]. On the other hand, the deposition process of silicon dioxide must be controlled to obtain good thin film adhesion force on the substrate[25][26][27].

With this procedure, four cells were realized with four different thicknesses of the SiO_2 layer, keeping the $SiN_2 : H$ layer at the optimal thickness of 80 nm. The performances of the five cells are reported in figure 3.1.3.

Samples	Color	Eff. (%)	FF (%)	J_{sc} (mA/cm^2)	V_{oc} (mV)
SiN_x : H (80 nm) (reference)	Light blue	16.87	76.89	35.18	623.6
SiO_2 (84 nm)/SiN_x : H (80 nm)	Grey yellow	16.97	76.66	35.77	618.6
SiO_2 (136 nm)/SiN_x : H (80 nm)	Purple	16.75	77.07	34.91	622.4
SiO_2 (190 nm)/SiN_x : H (80 nm)	Deep blue	16.13	76.93	33.86	619.2
SiO_2 (220 nm)/SiN_x : H (80 nm)	Green	16.43	77.05	34.30	621.6

Figure 3.1.3: Reported performances for the fabricated coloured cells compared to single ARC cell (standard measurement conditions AM1.5G, 100 mW/cm^2, 25 °C). (figure from [21])

The coloured cells are compared with the reference cell without the SiO_2 coating (light blue). Four colours are reported. Both the V_{oc} and the J_{sc} shows degradation for the coloured cells with respect to the reference. The best results are obtained with the grey yellow cells, showing an higher efficiency and short circuit current. The worst results are obtained with the deep blue cells. In general the results show that it is possible to obtain coloured solar cells by modulating a DARC, without significant degradations in the performance of the cell. The main loss comes from the J_{sc} loss, which shows that the optical losses represent the main efficiency limit for coloured solar cells.

In figure 3.1.4 the reflectivity curves are reported whereas in figure 3.1.5 the photographs of the produced coloured solar cells are shown.

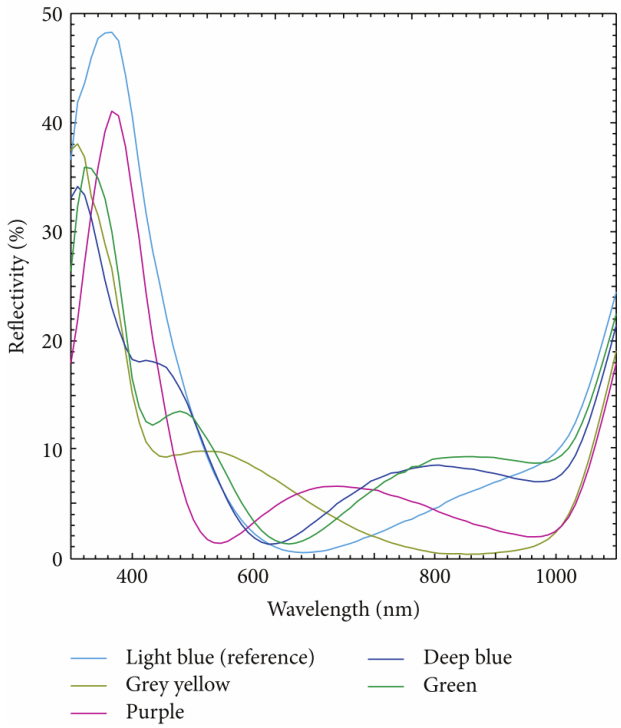

Figure 3.1.4: Measured reflectivities for the fabricated coloured cells compared to the reference ARC cell. The thickness of the $SiN_2 : H$ standard layer was kept constant at 80 nm while the thickness of the SiO_2 was changed to 84 nm, 136 nm, 190 nm and 220 nm for the grey-yellow, purple, deep blue and green cells. (figure from [21])

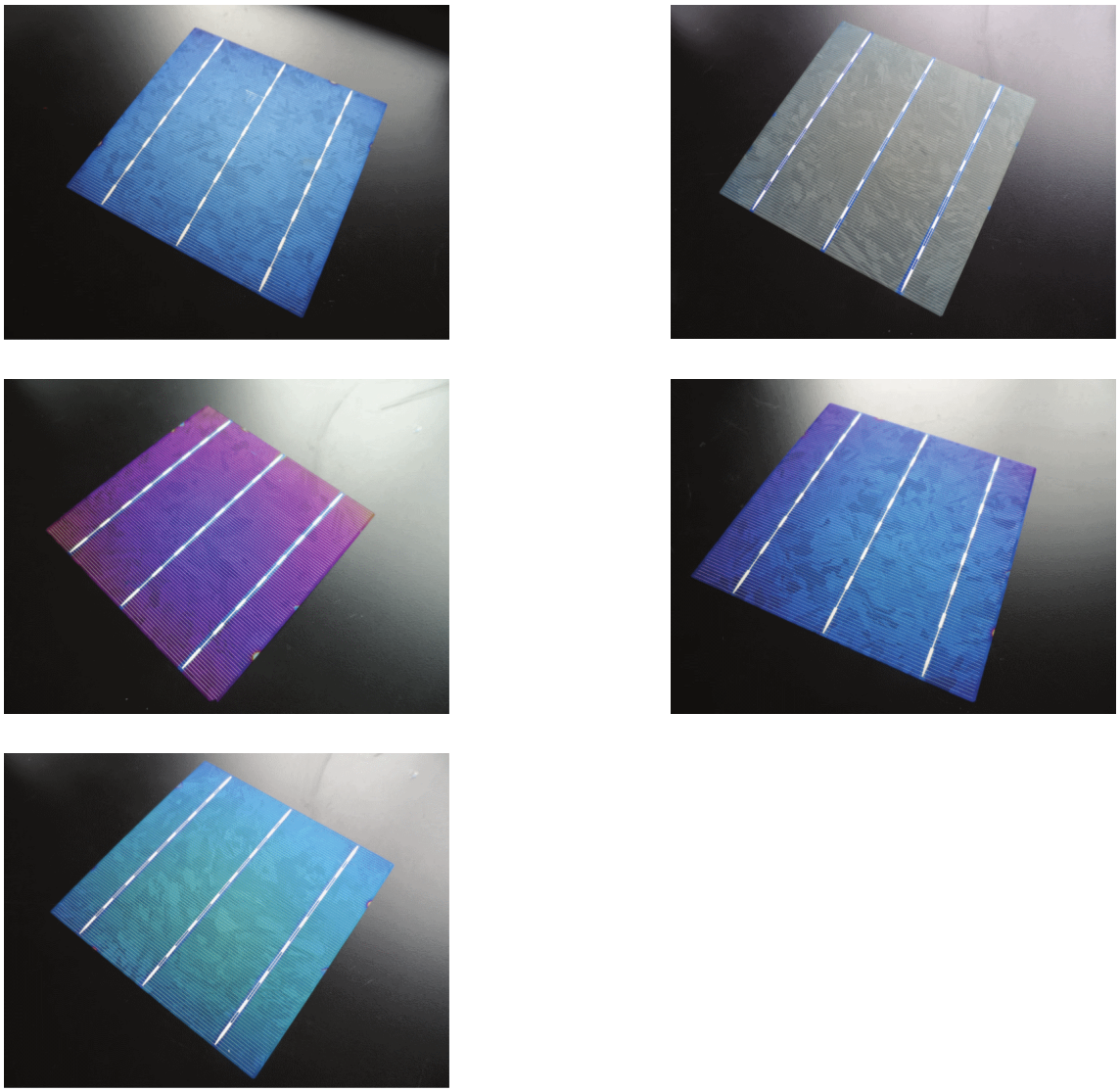

Figure 3.1.5: Photographs of the fabricated cells. (a) Reference cell with a single, 80 nm thick $SiN_x : H$ ARC. (b) Grey-yellow cell with a 84 nm thick SiO_2 layer. (c) Purple cell with a 136 nm thick SiO_2 layer. (d) Deep blue cell with a 190 nm thick SiO_2 layer. (e) Green cell with a 220 nm thick SiO_2 layer. All the SiO_2 layer were deposited on top of the standard 80 nm $SiN_x : H$ layer. (figure from [21])

As shown in the pictures, four coloured cells were obtained, with a certain uniformity in the appearance. There are small chromatic aberrations in the edges, probably due to a not perfect spatial uniformity during the deposition. Apart from the purple cell, whose colour show a certain level of purity, the other cells show colours which are more a combinations of different hues, as confirmed by the reflectivity curves. This characteristic may be interesting in terms of aesthetics applications if earthlike colours are preferred but could represent a disadvantage if a higher freedom of design on the colour reflected is required.

Other examples of DARC and multilayer interference for coloured solar cells The exploitation of light interference phenomena appearing in multilayer structures to generate colour is certainly the technique most commonly found in the literature. This is due to the fact that the fabrication of single and double anti-reflective coating rely on a well known and developed technology, since the presence of an anti-reflective layer is a constant feature found in every type of solar cells. The advantage of this colouring technique is that it can be integrated virtually with any PV technology.

As an example, in 2017, Arinze et al. reported the fabrication of coloured colloidal quantum dots solar cells, exploiting an optimization algorithm to determine a tradeoff between photocurrent reduction and colour tunability.[28] The solar cell structure was based on a standard heterojuction architecture, with an n-type layer of TiO_2, a p-type layer if PbS colloidal quantum dots and a buffer layer of MoO_3 sandwiched between a top Ag electrode and a bottom glass covered indium tin oxide contact. The preparation of blue, green, red and yellow cells was reported, with a power conversion efficiency ranging between 3.5 and 2 % for the blue and red cells, respectively. The solar cells showed a short circuit current density between 14.5 mA/cm^2 for the blue cells and 10.2 mA/cm^2 for the red cells.

Another example where the colour of a common c-Si solar cell was modulated by depositing an additional SiO_2 layer on top of the standard SiN_x:H anti-reflective coating was reported in 2012 by Chen et al.[29] Here red, green and yellow cell were fabricated by plasma-enhanced chemical vapour deposition on a standard c-Si solar cell. The reflectance spectra of the prepared cell were measured, showing reflectance peaks in the visible range of around 5%. The reflectance spectra were used to calculate the expected short circuit current density of the fabricated cells, obtaining remarkable values of 36.52, 36.4 and 36.63 mA/cm^2 for yellow, red and green cells, respectively, compared to the value of the reference, single ARC silicon cell of 36.74 mA/cm^2.

3.2 Coloured ultrathin solar cells by means of an optical cavity

The realization of a coloured power producing solar cell exploiting the interference phenomena observed in a Fabry-Perot (F-P) resonator have been suggested by Kyu-Tae Lee et al. in 2014.[30] This technique was proposed as an alternative to the previous attempt to realize colour filter using the concepts of structural colours, e.g. realizing an optical filter by nano-structured gratings [31] or exploiting plasmonic effects observed for nano-particle based coatings [32].

A F-P resonator is a linear optical cavity made by two partially transmissive mirrors. Light is reflected multiple times in the cavity between the reflective surfaces and undergoes interference phenomena. Depending on the properties of the resonator (distance between mirrors, reflectivity/transmittivity of the mirrors) sharp resonances at certain wavelengths appear and the cavity can function as an optical filter, showing dips in the reflection profile.[33]. The realized structure is shown in figure 3.2.6. Here the F-P resonator was realized by sandwiching a ultrathin layer of amorphous

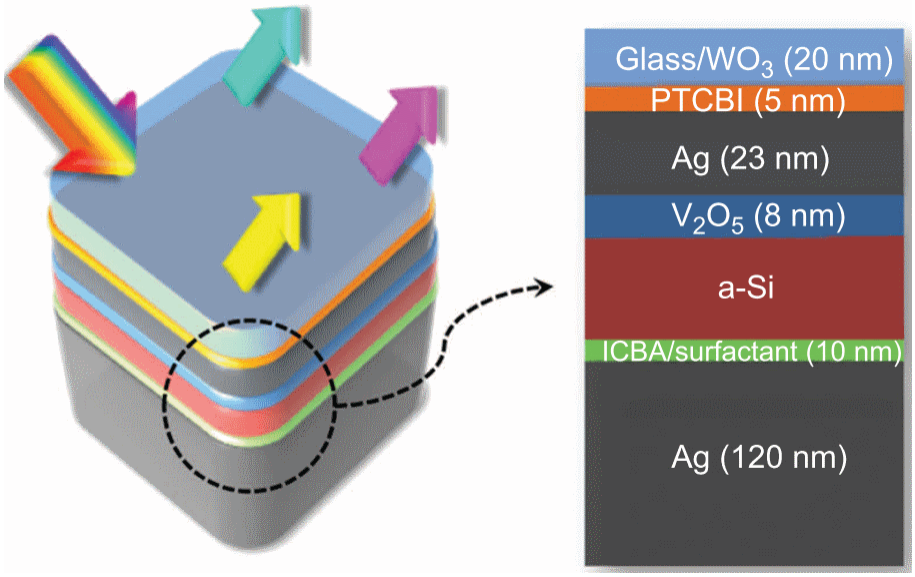

Figure 3.2.6: Schematic representation of the proposed design. A thin layer of a-Si act as light absorbing material and is sandwiched between two silver (Ag) electrodes by means of organic carrier transporting materials (ICBA/surfactant and V_2O_5). (figure from [30])

silicon (a-Si) between two charge transporting layer, combining organic and inorganic material to obtain a new structure able to overcome the intrinsic problems of the metal-semiconductor-metal configuration needed to achieve optical resonance.

The main issue is that, in order to have optical reflection in the visible range, the a-Si layer should not exceed a thickness of 10-30 nm. This is in contrast with the thickness requirement of a traditional a-Si solar cell, for which the doped regions are already thicker than 40 nm.[34] For this reason the doped regions were replaced by two organic semi-permeable membranes. As shown in figure 3.2.6, on top of a thick Ag cathode (120 nm), an electron-transporting organic layer of indene-C_{60} bisadduct

(ICBA)[35] is deposited. A C60 surfactant is used to lower the Ag work function and form the contact between the ICBA layer and the cathode. Then the thin a-Si layer (10-27 nm) works as the active layer. On top of it a vanadium oxide (V_2O_5)[36] layer work as a hole-transporting membrane thanks to its high work function. Then the top anode was realized combining Ag and tungsten trioxide to obtain high transmission. The deposition techniques and the used material are summarized in table 1

Layer	Material	Technique	Details
Cathode (bottom)	Ag	Thermal evaporation	Last step
Electron-transport layer	ICBA/chlorobenzene solution	Spin cast on top of a-Si	C_{60} surfactant added
Active layer	a-Si	Plasma-enhanced CVD	240 °C , SiH_4 gasm 13.56-MHz-radiofrequency
Hole-transport layer	V_2O_5	Thermal deposition	high vacuum (10^{-6} mbar), rate of 0.2 $Å s^{-1}$
Anode(top)	WO_3/Ag	Thermal deposition	deposited onto a silica substrate, final sheet resistance $< 6\ \Omega sq^{-1}$

Table 1: Table representation of the deposition techniques as well as the material used to realize the layers composing the structure.

With the described design, it was possible to overcame the thickness requirements for the active layer. It is known that the n- and p- doped regions cause a significant charge recombination [37], so by substituting them with the mentioned organic materials, the optical losses can be lowered matching the absorption of the active a-Si layer. Power conversion efficiency close to 3% was reported thanks to this design.

Another issue of using a F-P resonator with a transparent medium is that the resonance wavelength is dependent on the angle of incidence of the light. This is due to the fact that when the radiation propagates through the transparent medium, it accumulates a certain phase shift, causing a blue shift in the resonance when the incident angle increases. The ultra-thin cavity discussed above allowed to achieve angle independence by combining two facts. First, in the a-Si, the phase change due to propagation, for different incidence angle, is lower with respect to the transparent medium case. Second, at the interface between the a-Si and the metal (Ag), a non-trivial phase change is observed due to the reflection phenomena. It was observed that the phase propagation change in the Si layer was reduced and partially cancelled out by the reflection phase shifts at the interface between the a-Si and the metal, with a consequent reduction in the angle dependency.[38] Another reported benefits of using this design is the low sensitivity to the polarization of the incident light. It was observed that the devices kept their angle independence both with p- and with s- polarized light.

Yellow, cyan and magenta cells were prepared and tested to obtain their reflectance spectrum, EQE and current-voltage (J-V) behaviour. The reported results and the obtained coloured cells are shown in figure 3.2.7.

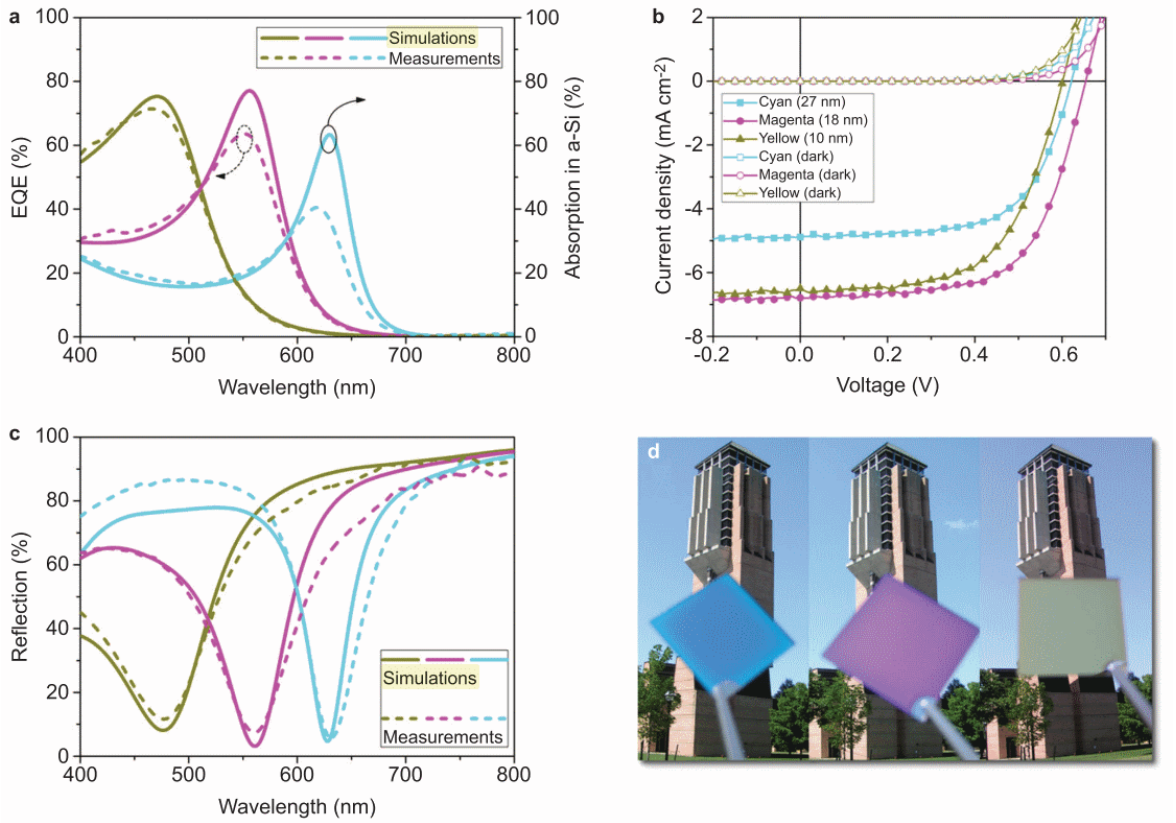

Figure 3.2.7: The electrical and optical behaviour of the fabricated coloured cell. (a) Measured and simulated EQE, (b) measured current-Voltage curves under illumination (standard AM1.5G measurements conditions) and in dark, (c) measured and simulated reflectance spectra at normal incidence and (d) photographs of the fabricated devices. All the figures reports the data for cyan, magenta and yellow cells having a thickness of the a-Si layer of 27, 18 and 10 nm, respectively. (figure from [30])

As reported (figure 3.2.7.a), the three coloured cells shows absorption peaks at three different resonance wavelengths, depending on the thickness of the absorbing layer. The simulated absorption profiles match nicely the EQE for the yellow cell while the magenta and cyan ones show lower absorption efficiency. This discrepancy was attributed to fabrication imperfections and physical defects: longer wavelengths are less absorbed by a-Si and have a stronger resonance causing more round trips between the two electrode and an higher sensitivity to defects and imperfections.

This results is also observed in the J-V characteristic of the cells. Yellow and magenta cells show similar short circuit currents J_{sc} (6.50 mA cm^{-2} and 6.79 mA cm^{-1} respectively). The lower power efficiency of cyan cells is confirmed by the lower J_{sc} of 4.87 mA cm^{-2}. For the three devices, regardless the different thickness (10, 18 and 27 nm for yellow, magenta and cyan respectively), a fill factor higher than 60% have been reported.

To further prove the benefit of using this structure, the highest power efficiency of nearly 3%, reported to be obtained for the magenta cell, can be compared with the record obtained for a single-junction cell using an intrinsic a-Si layer.[39] For this cell an efficiency of 10% was obtained with an active layer of 250 nm, 10 times

thicker than the one used in this work.

In figure 3.2.7.c, the simulated and measured reflection spectra of the CMY devices are reported. In this case, the devices show reflection dips at the resonance wavelengths of the F-P resonators. The dips wavelengths depend on the thickness of the active layers and were reported to be 630, 560 and 480 nm for cyan (27 nm), magenta (18 nm) and yellow cells (10 nm) respectively. The colour is the results of the reflected light, complementary of the absorbed wavelengths. The reflection spectra agree quite well with the perceived colours shown in the photograph reported in figure 3.2.7.c.

Finally, the angle independence of the obtained device is shown in figure 3.2.8, where the measured reflection spectra with respect to the angle of incidence and the wavelength of the incident light (p-polarized) is reported (in colour maps), for the three fabricated devices. As reported, for angle going from 0° to 60°, the reflectance of the device stays sable, for different wavelengths.

The same is observed if s-polarized light is considered, as shown in figure 3.2.9. This confirms that these device, for angles in the range 0°- 60°, shows a certain independence from the angle of incidence and from the polarization of the incident light.

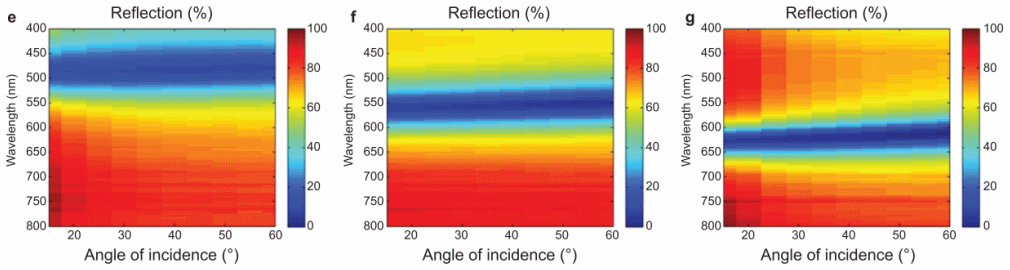

Figure 3.2.8: Colour maps of the reflected light intensity with respect to the wavelength and angle of incidence, for p-polaryzed light. (e)yellow, (f) magenta and g (cyan). (figure from [30])

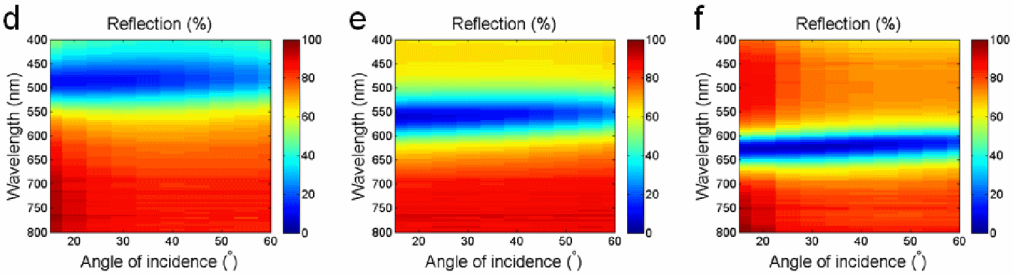

Figure 3.2.9: Colour maps of the reflected light intensity with respect to the wavelength and angle of incidence, for s-polaryzed light. (e)yellow, (f) magenta and g (cyan). (figure from [30])

In figure 3.2.10 is shown a demonstrative device (3 inches X 2.3 inches), proposed to show the possibility of realizing a coloured image combining shadow masks and coloured cells.

Figure 3.2.10: Photograph of a power producing device with the form of a colourful logo of the University of Michigan realized with the proposed design. (figure from [30])

Other examples of optical resonating cavity for coloured solar cells and colouring filters. The fabrication of coloured optical filter by means of the Fabry-Perot resonating properties of nanometric optical cavity was already reported in 2012 in a work by Kats et al.[40] Here again, ultra-thin optical coatings were prepared by depositing by electron-beam evaporation, small quantities of germanium (Ge) on a gold (Au) thin film. Ge was used for its highly absorbance in the visible range. The situation is very similar to the case analysed in the previous section, with the combination of a lossy dielectric with a metal lead non-trivial phase changes at the interface between the two media, leading to the appearance of an absorption resonance in the visible range, leading to the modification of the reflectance spectrum, and so the displayed colour, of the Au film. Yellow, orange, pink, blue and green samples were obtained changing the thickness of the Ge film, showing a good angle independence.

A similar approach was reported in 2011 by Park et al.[41]. Here the Fabry-Perot resonating structure was realized with the goal of producing colourful electricity-generating devices. The device was fabricated sandwiching between an Au nanograting and a Al film, two conjugated polymer organic layers of poly(3,4-ethylenedioxythiophene):poly(styrenesulfonate) (PEDOT:PSS) and poly(3-hexylthiophene):[6,6]-phenyl C61 butyric acid methyl ester (P3HT:PCBM). By

changing the thickness of the P3HT:PCBM blend, the reflectance spectra of the devices showed a dip at different wavelengths. This way, cyan magenta and yellow devices were prepared showing a power conversion efficiency of 1.55, 0.82 and 0.6 %, respectively.

3.3 Coloured silicon solar modules using integrated resonant dielectric nanoscatterers

In 2017, Verena Neder et al., reported the possibility of turning the appearance of a photovoltaic module by exploiting the properties of dielectric Mie scatterers.[42] The interaction of light with dielectric particles having a dimension smaller than the wavelength of the incident radiation can be described by the Mie solution of the Maxwell equation, proposed by G. Mie in 1908.[43] Here the scattered field depend on the radius of the particle and on its refractive index[44]. With this theory it has been demonstrated that dielectric nanostructures build with low-loss materials show resonant spectra with a narrow line-width, whose position can be connected to the geometry of the structure and to its building material. [45][46].

In this work an optical filtering layer was realized on top of a textured crystalline silicon (c-Si) solar cell, by patterning a sapphire slide with Si nanocylinders. The two proposed designs are shown in figure 3.3.11.a and 3.3.11.b.

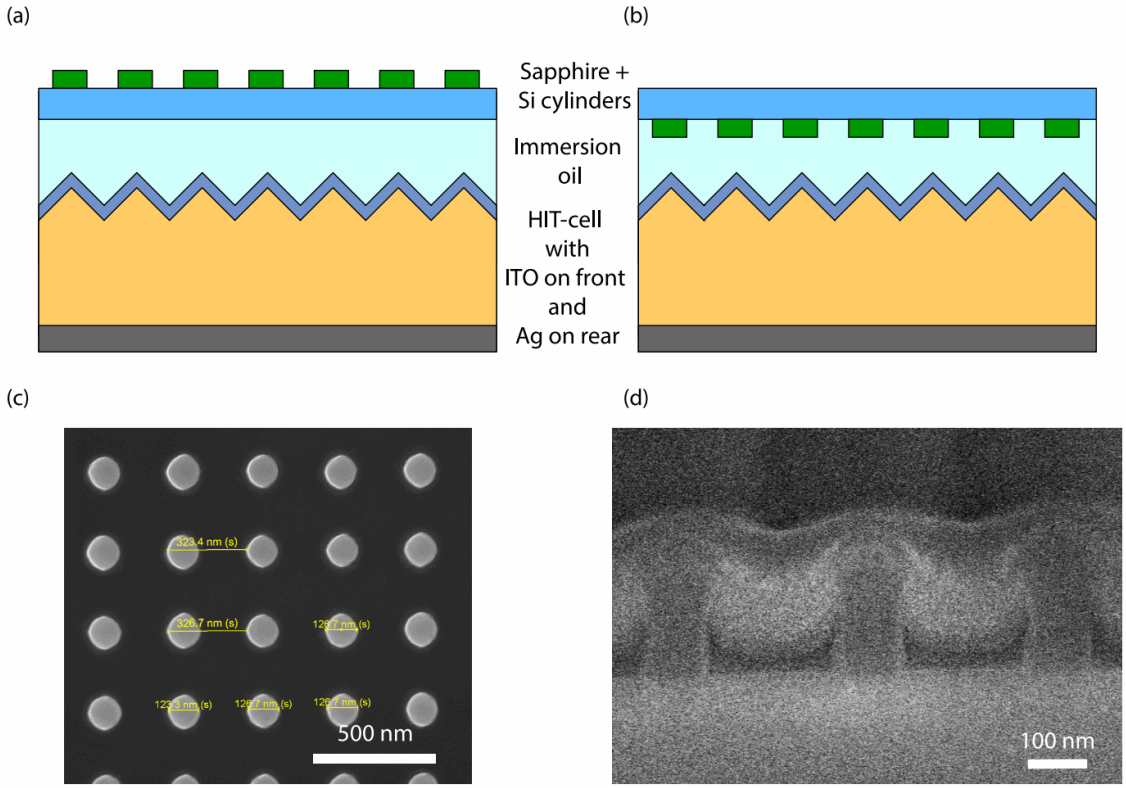

Figure 3.3.11: Schematic representation of the the proposed design where an array of silicon nanocylinders is realized on a sapphire slide and applied on top of a textured crystalline silicon solar cell, in top (a) and bottom (b) configurations. The top(c) and side (d) scanning electron microscopy images of the patterned region are reported. (figure from [42])

The starting solar cell was a textured silicon heterojunction solar cell, covered with an indium tin oxide (ITO) layer that works as a transparent conductor and acts as an anti-reflection (AC) coating, with a thickness of 80nm. The back contact is realized with a silver (Ag) metallization. Immersion oil was used to match the index of the refractive index of the top layer, allowing the coupling with the underlying solar cell. The light scattering layer was realized starting from a silicon-on-sapphire substrate (500nm Si on 0,46 mm sapphire). By reactive ion etching (RIE) in a HBr_2 (25 sccm) and O_2 (2 sccm) plasma, the sapphire layer was lowered to 200 nm. Then the pattern of silicon cylinders was realized by substrate conformal imprint lithography (SCIL). In figure 3.3.11.c a SEM image shows the final pattern while in figure 3.3.11 a side view is reported: 100-120 nm wide cylinder, with an height of 240 nm were imprinted with a pitch of 325 nm.

Two different designs were studied by placing the patterned side on the bottom of the sapphire slide, facing the cell (bottom) or on the top facing the air (top). In figure 3.3.12 the measured scattering efficiency of both patterned (top and bottom) and unpatterned modules are shown. Measurements were performed collecting, with a spectrometer, all the reflected light from the sample which was illuminated with a collimated beam from a supercontinuum light source, coupled in at incidence angle of 8°. Both structures showed a resonance peak in the green region, for a wavelength of 528 nm (see figure 3.3.12.a and 3.3.12.b insights). In the "bottom" configuration, the resonance was red shifted because of the higher refractive index of the matching fluid. This result is in accordance with the photograph of the patterned module (bottom), shown in figure 3.3.12.d where a bright green colour is observed, showing a remarkably high level of visible homogeneity over the whole area (5 x 5 mm^2). In both configurations, the reflectance was enhanced for patterned modules with respect to unpatterned ones, for incidence angles between 8° and 75°, as shown in figure 3.3.12.a and 3.3.12.b (main panels).

The electrical characterization of the patterned modules, compared with the bare and unpatterned ones, is shown in figure 3.3.13. The measured external quantum efficiency for "top" and "bottom" configurations shows important dips (25 % - 30 %) near the resonance wavelengths due to the amount of light being scattered and absorbed by the Si nanoscatterers. The absorption process causes the EQE to be reduced also in the range of wavelengths below resonance. These losses decrease the short circuit current by a relative 16 % and 17 % with respect to the base Si cell (figure 3.3.13, inset). From the I-V curves, an efficiencies of 13.7 % and 12.9 % were calculated for the top and bottom configurations. Compared to the base Si cell (17 %), relative reduction in efficiency of 14 % and 19 % (top and bottom, respectively) were reported. The top configuration shows better performances due to the fact that the front-nanopattern behaves like an (effective-index) AR coating.

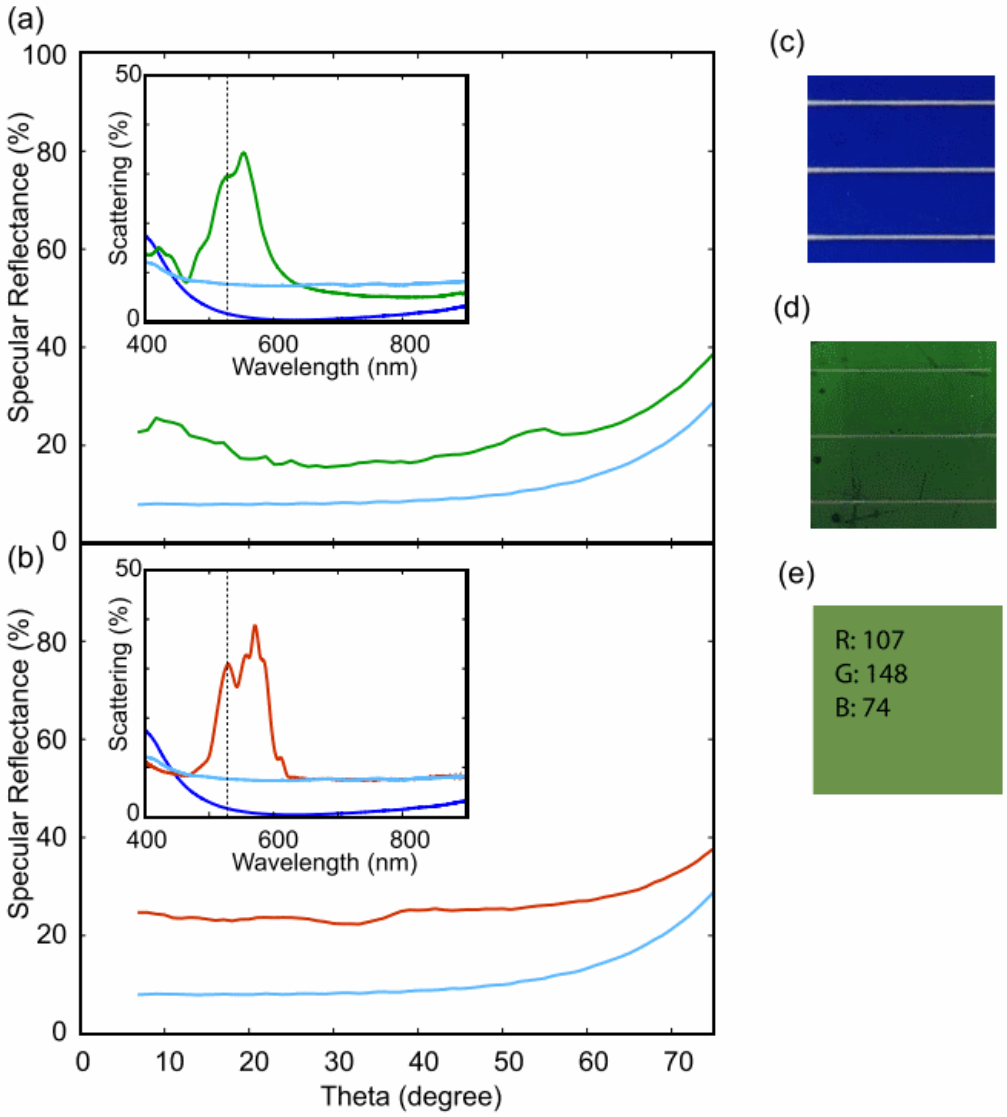

Figure 3.3.12: Measurements of the specular reflectance with respect to the angle of incidence (theta) for top (a, green line) and bottom (b, red line) configurations. The reference values for unpatterned module are also shown (light blue line). In the insets also the intensity (in percentage) of the light scattered back from the array of nanocylinders is shown for top (a, green) and bottom(b, red) configurations. Again the reference values for an upatterned module are shown (light blue) as well as the value for a bare Si heterojunction solar cell (dark blue). The photographs of the unpatterned (c) and patterned modules (d) are shown with the calculated visual color defined in RGB coordinates (e). The dimension of the photos are 5 x 5 mm^2. (figure from [42])

In figure 3.3.13.b, the effect on the transmittance profile (inset) of a nanopatterned (front) sapphire slide, on the effective solar spectrum reaching the cell is shown. The spectral intensity is clearly reduced (green line) near the resonance wavelength and below, in accordance with the results reported for the EQE. It was reported that the total integrated power is reduced from 1000 W/m^2 (AM1.5G) to 776 W/m^2. For this reason, the Shockley-Queisser efficiency limit for a Si solar cell in this configuration is reduced to 32.8 %.

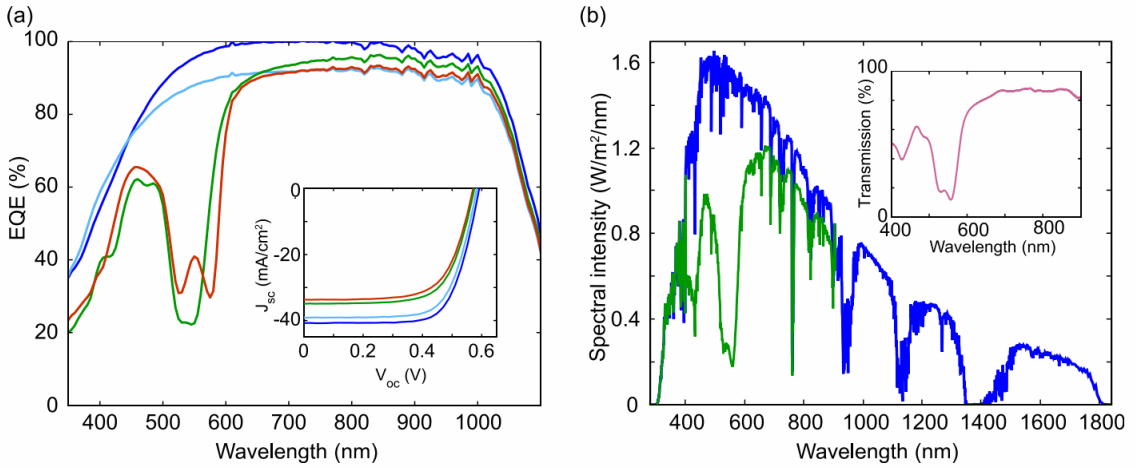

Figure 3.3.13: Electrical characterization of the produced solar cells and effect of the colouring layer on the spectral intensity impinging on the cell. (a) Measured EQE of bare silicon solar cell (dark blue), unpatterned module (light blue), and nanopatterned module in top (green) and bottom (red) configuration. In the inset the corresponding current-voltage behaviour for the same cells is reported. (b) AM1.5G solar spectrum (dark blue) and calculated modified spectrum after correction using the measured transimssion spectrum (inset) of a nanopatterned sapphire slide (front configuration, green).(figure from [42])

The reported results shows the possibility of realizing an optical filter to be applied directly on top of a power producing solar module, allowing to select a narrow interval of wavelength for which light is reflected, displaying the corresponding colour. By engineering the geometry of the patterned array of nanocylinders, the resonance wavelength could be varied, allowing in principle to tune the visible appearance of the cell. By doing this, relatively low losses in the EQE and consequently in the I-V performances would be observed. It was mentioned that by using a non-absorbing dielectrics such as TiO_2, the short-wavelength absorbance caused by the Si nanocylinders could be avoided. The use of Si was motivated with the fact that it is a material with an high dielectric constant (high-index, low-loss material needed) which nanofabrication parameters are well known so easier to process.

It was reported that the SCIL nano-imprint technique is a valid option to full area patterning of solar cells with a dimension of $150x$ 150 mm^2, so scaling up to roll-to-roll processes represent a feasible option.

3.4 Colouring c-Si solar cells by exploiting plasmonic effects

In 2016, G. Peharz et al., reported an experimental study, performed on industrial mono- and poly-crystalline Si solar cells, with the goal of exploiting the plasmonic effect of resonance creating at the interface between metal nanoparticles and a dielectric substrate (or encapsulant).[47] By coating the surface of the Si solar cells with a layer of nanosized silver (Ag) particles, resonance peaks were observed in the reflection spectra of the coated area. These position of the peaks depended on the size and shape of the deposited nanoparticles so, by varying the sputtering parameter it was possible to shift the resonance peak to a desired wavelength, obtaining different colours. Si solar cells with green, yellow-green, green-brownish and magenta-brownish colours with a certain degree of independence from the viewing angle were obtained. No electrical characterization was reported for the produced solar cells.

The particles were deposited by pulsed DC sputtering thin films of silver onto different substrates (polished silicon, mono- and poly-crystalline Si cells). A sputtering power of 700 W and an Argon flow rate of 30 sccm were used. To change the thickness of the deposited layer, the sputtering time was varied and for plane substrates an effective deposition rate of 7.5 nm/minute was derived. Then by annealing the coated substrates at 300°C for 10 minutes in standard atmosphere the nano-particles were formed. In figure 3.4.14 the sputtered particles (different sputtering time) on polished silicon substrate are shown.

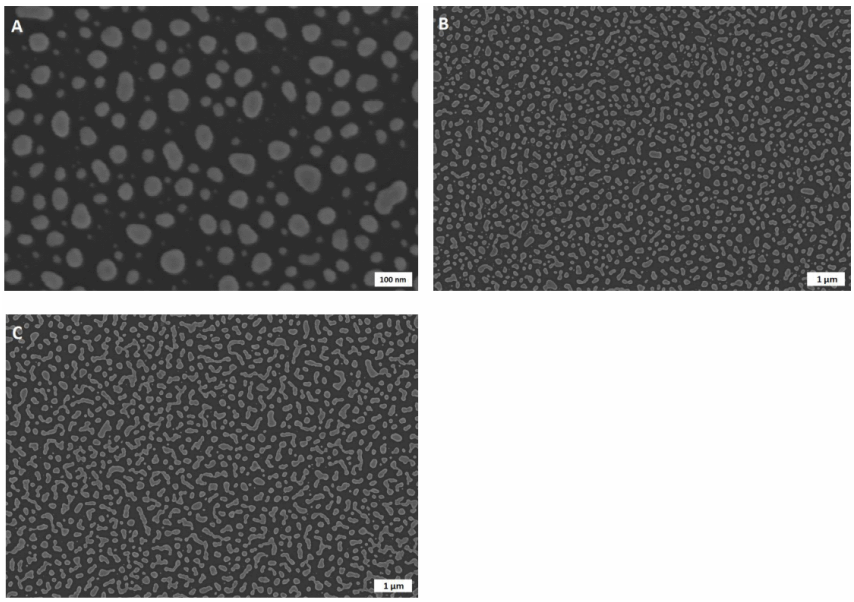

Figure 3.4.14: SEM images of the silicon substrate patterned with silver nano-particles, with a sputtering time of 40 seconds (A, scale bar 100 μm), 80 seconds (B, scale bar 1 μm) and 120 seconds (C, scale bar 1 μm). (figure from [47])

For different sputtering time different particles size and shapes are observed: as shown in figure 3.4.14.A, for 40 seconds, a 5nm thickness film is deposited and, after annealing, nano-particles with diameters ranging from 10 to 100 nm and shapes mostly hemispherical are observed. Increasing the sputtering time to 80 seconds, the

variety of sizes and shapes increase, mostly due to the aggregation of hemispherical particles. If the sputtering time is increased to 120 seconds, aggregations with irregular shapes and sizes close to 1 μm start to form. In figure 3.4.15, the optical characterization of the coated polished silicon substrates is shown.

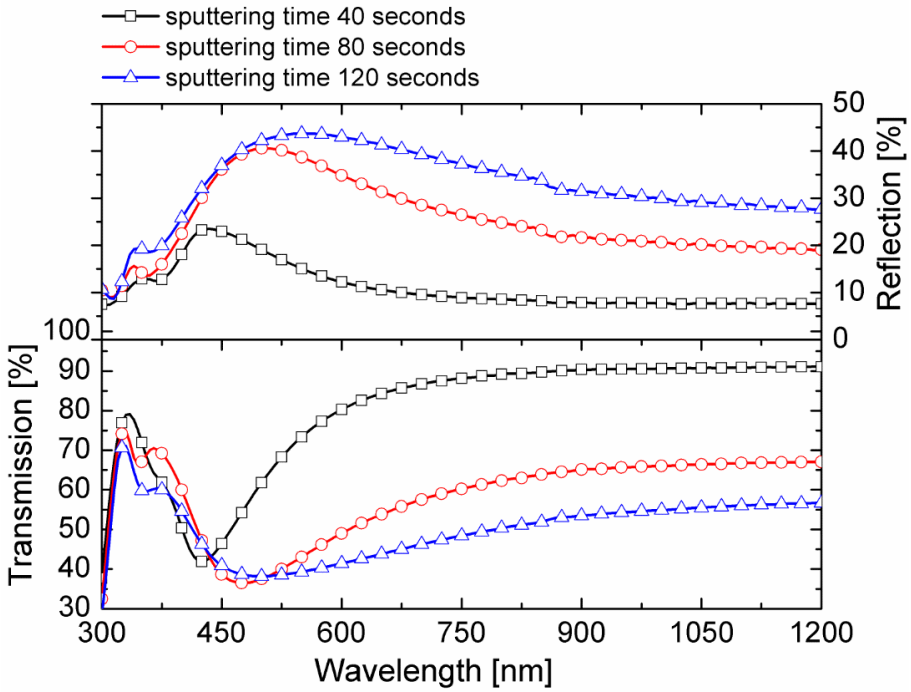

Figure 3.4.15: Transmission and reflection spectra of Ag nano-particles on glass substrates fabricated by varying the sputtering times. [47]

It can be seen that, for the particles with the smallest size (40 seconds), a peak in the reflection spectrum is observed at around 450 nm. This peak shifts to larger wavelengths as the sputtering time is increased. This is due to the increasing particle size that determine a shift in the plasmonic resonance frequency. Moreover, the higher size and shape distribution obtained for higher sputtering time determine a broader maximum width. In the infrared region, the transmission decreases for higher sputtering time (higher particle size) while the reflection increases: this is due to the fact that for diameters of around 1 μm, bulk silver behaviour starts to appear.

In figure 3.4.16 SEM images of the sputtered solar cells are shown.

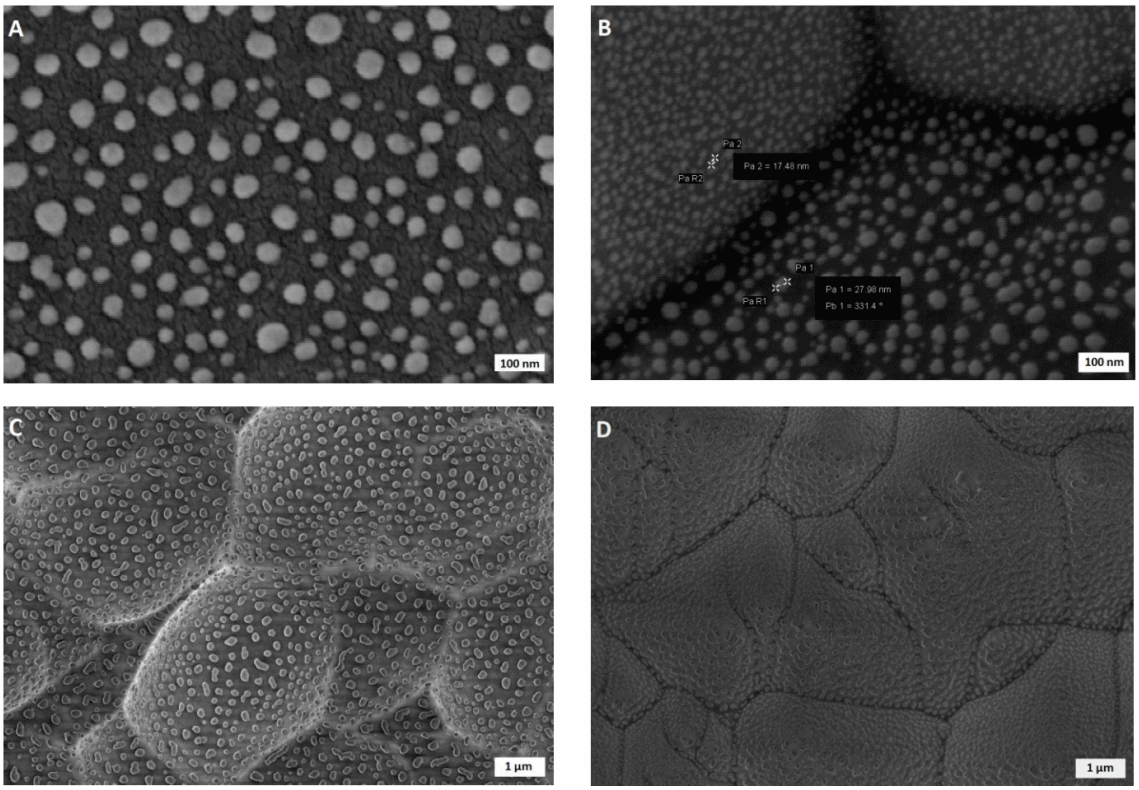

Figure 3.4.16: SEM images of solar cell surfaces patterned with silver, with a sputtering time of 40 seconds (A,B, scale bar 100μm) and 120 seconds(C,D, scale bar 1μm) and annealed at 300°C. Figure A and C refers to polycrystalline silicon substrate while figure B and D refers to monocrystalline silicon substrate. [47]

Monocrystalline solar cells have an higher surface roughness with respect to polycrystalline solar cells and this will cause thinner films to form on monocrystalline cells, having, after annealing, smaller particles. With a small sputtering time (40 seconds), hemispherical nano-particles with a diameter between 10 and 50 nm formed on top of both substrates. If the sputtering time was increased (120 seconds), larger nano-particles formed due to the interconnections between smaller aggregates and a maximum size of 500 nm was reported.

The optical behaviour of the coated solar cells is similar to the one observed previously for the polished silicon. In figure 3.4.17 the reflection spectra of the produced cells are shown, compared with the uncoated ones.

As observed for the polished silicon substrate, the cells show resonance peaks whose wavelengths shifts to higher values if the sputtering times (and so the particles sizes) are increased. Due to the higher roughness of monocrystalline solar cells, smaller nano-particles with the same sputtering time are formed (compared with polycrystalline counterpart). The consequences of this are observed in figure 3.4.17: for the same sputtering time, coated monocrystalline cells show lower resonance wavelengths and also lower reflectance value with respect to the polycrystalline cells.

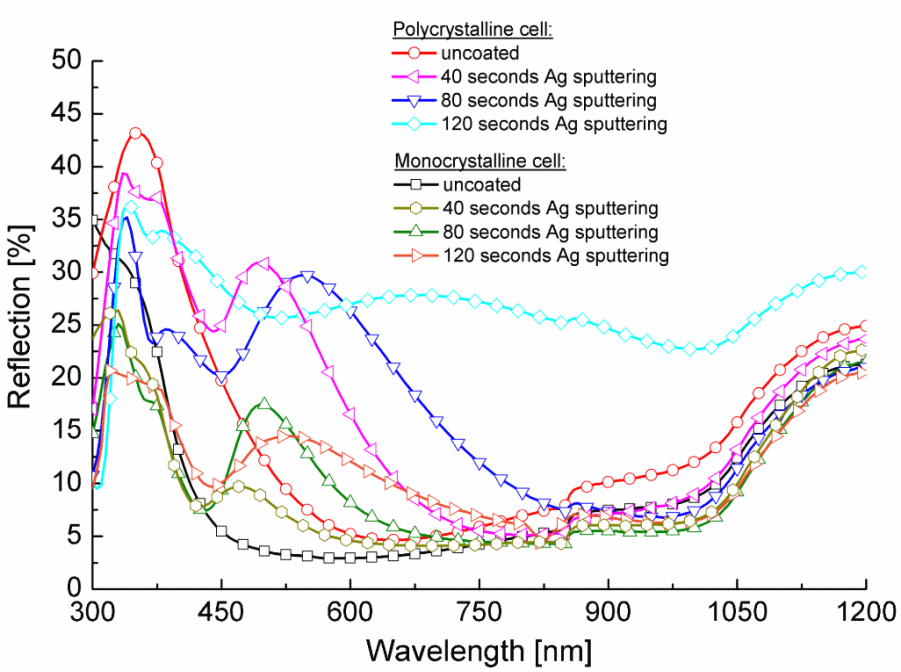

Figure 3.4.17: Measured reflectance spectra of the fabricated solar cells (poly- and monocrystalline) depending on the sputtering time and compared to uncoated devices. [47]

This effect is highly visible for polycrystalline cells sputtered for 120 seconds: in the near infrared spectral region, the reflection values are substantially increased. Here the bulk Ag behaviour (observed for larger particles) start to appear. In figure 3.4.18 the photographs of the produced cells are shown.

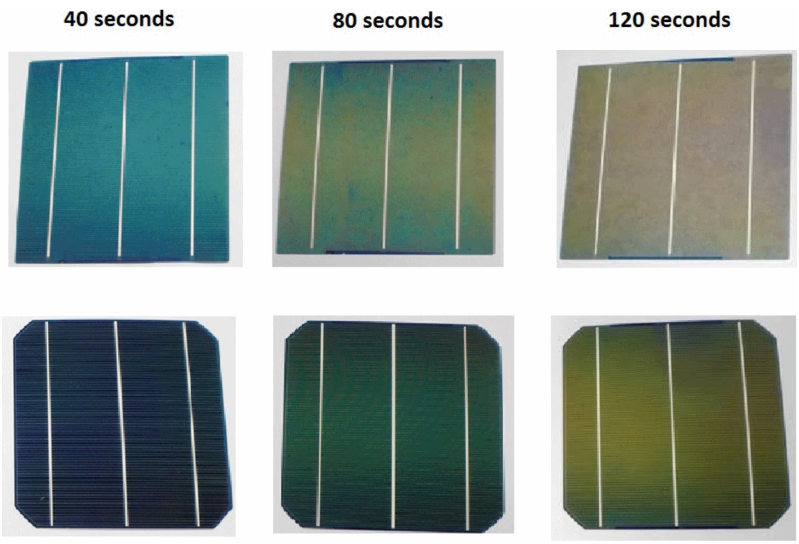

Figure 3.4.18: Photograph of industrial polycrystalline (first row) and monocrystallan (second row) Si cells sputtered with Ag nanoparticles. The effect on the colour of different sputtering time is shown. [47]

It can be observed that increasing the sputtering time, the growing size of

the deposited nano-particles yield different colours, as expected. In the top row, polycrystalline cells are shown while monocrystalline cells are shown in the second row. With a sputtering time of 40 seconds, a green colour is observed for polycrystalline cells while the same time has almost no effect on the colour of monocrystalline cells. If the sputtering time is increased to 80 seconds, in the first case a mixture of green and yellow is observed, with in the second (mono-Si) a greenish colour starts to appear. Finally for a sputtering time of 120 seconds, sputtered polycrystalline cells shows a magenta-brownish colour while the same process produce a combination of green and brown on monocrystalline cells. As observed, the produced colours show a relatively low colour purity, as confirmed from the low level of reflection observed at the resonance wavelength and for the wider line-width (at resonance) observed for longer sputtering times (higher particle sizes).

As expected, the produced colours seem to be independent from the viewing angle, as shown in figure 3.4.19. Here the centre of a monocrystalline solar cell was covered with an Ag nano-particle film. If observed from different perspective, the uncoated region shows different colours, due to the dielectric anti-reflective coating. The colour of the coated region, instead, appear to be the same if observed from different angles.

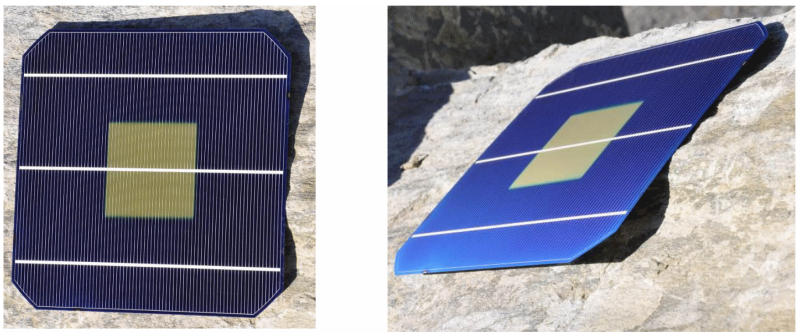

Figure 3.4.19: Photograph of a monocrystalline solar cell with a 5x5 cm^2 portion coated with Ag nanoparticles, observed at different angles. [47]

3.5 Colorfull perovskite solar cells with nanoporous photonic crystal

In 2015, Wei Zhang et al. proposed the realization of colourful perovskite solar cells by integrating a porous photonic crystal (PC) scaffold within the photoactive layer of an opaque perovskite solar cell.[48] The idea was to exploit the interference of coherently scattered light by building a multilayer of porous PC scaffold, with different refractive index, and then infiltrating the absorbing perovskite in the interspace between particle. The alternating refractive index causes the final structure to show resonance peaks in the reflectance spectrum (in the visible range) and then a colourful visual appearance.

In figure 3.5.20 a scheme of the built solar cell together with a secondary SEM image of its cross section are shown.

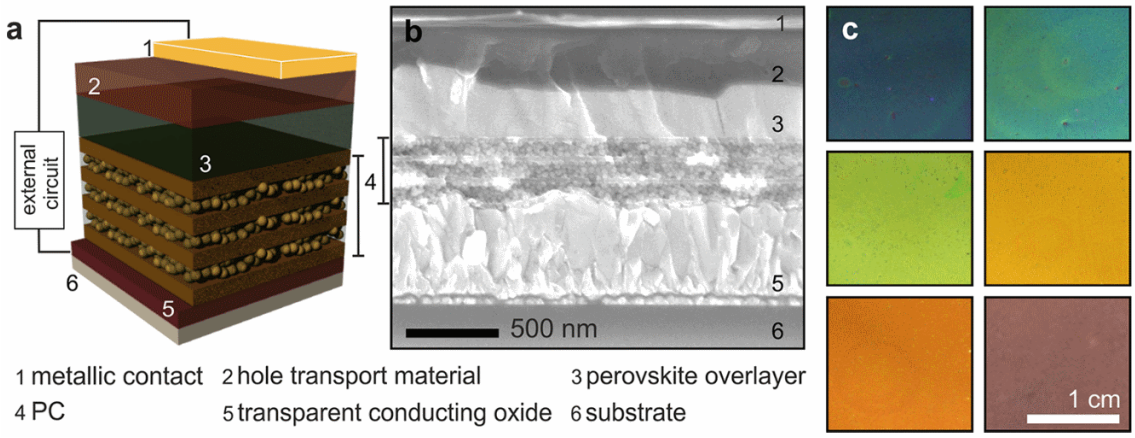

Figure 3.5.20: Schematic representation of the PC-based perovskite solar cell (a). It is possible to identify the different layers: glass substrate (6), fluorinated tin oxide (5), scaffold of alternating layers of porous TiO_2 and porous SiO_2 (4) to build the PC structure within which $CH_3NH_3PbI_{3-x}Cl_x$ is infiltrated, spiro-OMeTAD as hole transport material (3) and top contact made by gold (1) on top of fluorinated tin oxide (2). The SEM images of the cross section of the structure is shown (b) as well as the colours of the device with different PC structures. (figure from [48])

As shown, the structure was deposited over a glass substrate (6) on top of which a fluorinated tin oxide (FTO) was deposited as a transparent conducting oxide (5). Then porous TiO_2 and porous SiO_2 layers were deposited on top of each other to build the scaffold (4). $CH_3NH_3PbI_{3-x}Cl_x$ was then infiltrated in this structure. The hole conducting layer was build using spiro-OMeTAD (3) and finally the top contact was build depositing gold contact on top of a FTO layer (1 and 2 respectively).

Due to the electric transport properties of perovskite, the thickness of the porous scaffold was limited to a value of 400 nm. A higher value was said to deteriorate the efficiency of the device [49]. From this starting point, a fist attempt was to stack different kinds of nanoparticle layers [50]. Efficient solar cells were obtained but the infiltration of perovskite caused the refractive index contrast to be substantially lowered. An increased number of layers did not solve the problem since the final performance was poor. A trade-off had to be found between scaffold thickness and

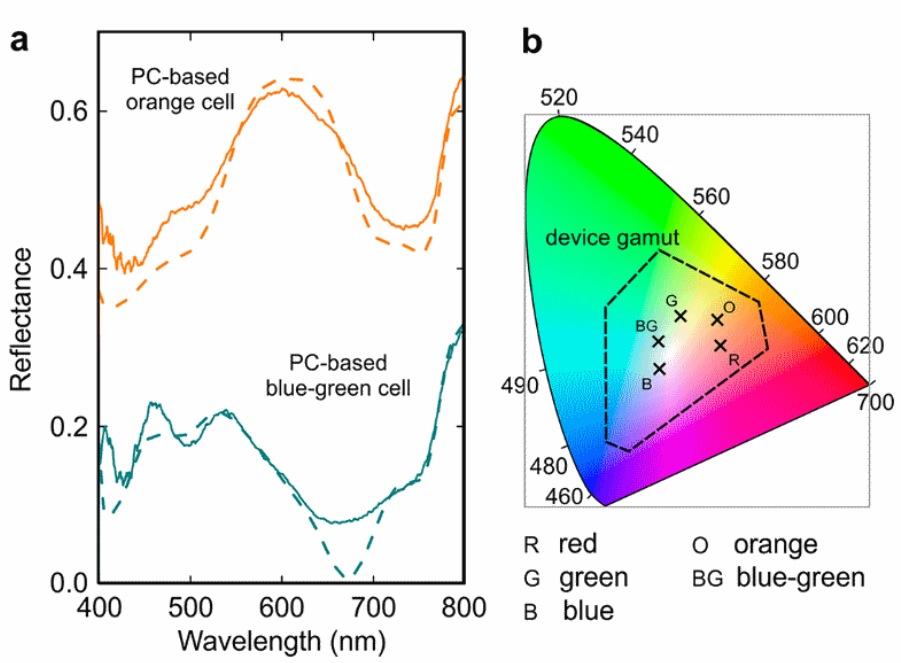

Figure 3.5.21: (a) Simulated (dashed lines) and measured (solid lines) reflectance spectra of the PC-based orange and blue-green perovskite cells. Orange curves are vertically shifted by $\Delta R = 0.3$. (b) CIE 1931 chromaticity space, showing the colour hues of the PC-based (R) red (0.41, 0.34), (O) orange (0.41, 0.40), (G) green (0.33, 0.41), (BG) blue-green (0.29, 0.35), and (B) blue (0.29, 0.30) cells. [48]

high reflectance after infiltration. To do this, the structure in 3.5.20 was proposed: the scaffold was build by alternating TiO_2 layers with open porosity of 4 % and SiO_2 layers with open porosity of 50 %. The different porosity caused the two layer to have refractive indexes of 1.25 and 2.38, at $\lambda = 500$ nm, respectively. A shift in the effective refractive index of the structure was observed after infiltration.

A theoretical model was developed to simulate the proposed design, based on transfer matrix formalism[51]. The reflectance spectra of the two coloured cells (orange and blue-green) were calculated as well as the electric field distribution inside the structure (figure 3.5.21 a, b and c).

As can be seen, the experimental data well approximate the theoretical value for reflectance. In both cells, peaks were seen at different wavelengths in the visible spectrum. Since the colour of the device is the result of the convolution of the reflectance spectrum with the photopic response of the human eye, the expected colour coordinate were calculated and displayed on the CIE 1913 chromaticity diagram in figure 3.5.21.d (black crosses). In the same diagram the full range of colours obtainable with this structure are included in the dashed polygon line. Ideally, by changing thickness of the layers building the porous scaffold, the colours included in this area could be achieved. The reported examples achieved with different PC structures are shown in figure 3.5.20.c.

The dependence of the perceived colour with respect to the viewing angle was calculated and is shown in figure 3.5.22.

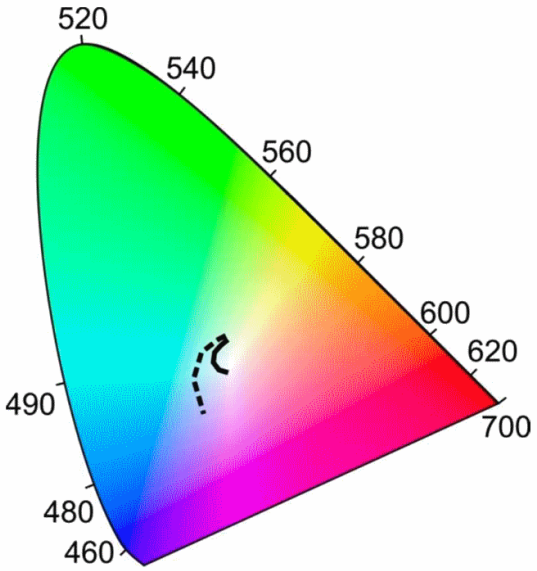

Figure 3.5.22: CIE 1913 chromaticity space, showing the calculated colour hues of the PC-based perovskite cells for the range of angles of incidence comprised between 0° and 60° with respect to the surface normal. The solid line refers to the PC integrated within the device while the dashed line refers to the directly illuminated PC, without any coating. [48]

The results show a small dependency on the viewing angle, with was further reduced if the photonic structure was integrated within the solar cell (solid line), with respect to the case where light impinges directly on the PC structure (dashed line).

The electrical characterization of the proposed structure is shown in figure 3.5.23. The measured external quantum efficiency with respect to the wavelength is shown for the orange and blue-green cells, as well as for a reference cell made with a mesoporous SIO_2 scaffold with thickness of 370 nm. In the spectral region where the coloured cells show a peak in reflection, the EQE is reduced, compared with the reference one. In figure 3.5.23. d-g, some performance parameter for solar cells with respect to the colour displayer are reported. The values were measured under simulated AM1.5G sunlight. It can be observed that the short circuit current density (J_{sc}) is the parameter most influenced by the increase of the PC lattice parameter. While the colour is turned from blue to red, the J_{sc} decrease from values around 12 mA/cm^2 to 7 mA/cm^2 and the same trend is obviously observed for the power conversion efficiency (PCE) since the open circuit voltage only slightly change as the colour is varied. In general though, the best performing devices showed PCE over 6 %, with a peak of 8.8 % for the blue cells. This was compared with the PCE of the reference perovskite cells built with a 370 nm mesoporous SiO_2 scaffold. In this reference case an average PCE of 9.5 % was reported with a peak of 10.5 % .

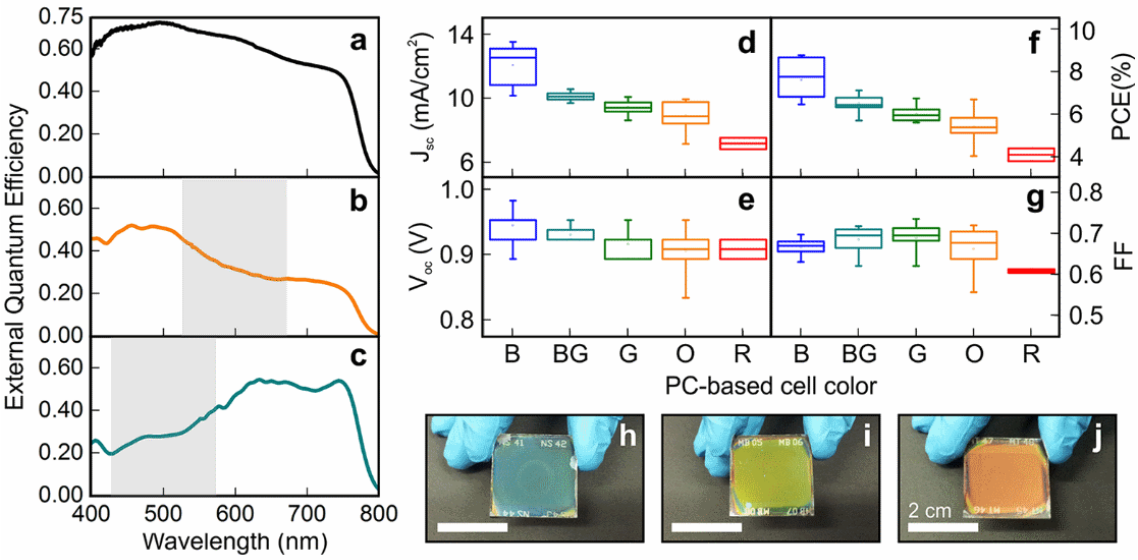

device color		J_{sc} (mA/cm^2)	PCE (%)	V_{oc} (V)	FF
blue	best	13.4	8.8	0.98	0.67
	average	12.1 ± 1.2	7.6 ± 0.9	0.94 ± 0.02	0.67 ± 0.02
blue-green	best	10.4	7.0	0.95	0.71
	average	10.1 ± 0.3	6.5 ± 0.4	0.93 ± 0.02	0.68 ± 0.03
green	best	9.9	6.7	0.92	0.74
	average	9.4 ± 0.4	6.0 ± 0.4	0.92 ± 0.02	0.69 ± 0.03
orange	best	9.9	6.6	0.95	0.71
	average	8.9 ± 0.9	5.4 ± 0.8	0.91 ± 0.03	0.66 ± 0.05
red	best	7.6	4.5	0.93	0.62
	average	7.2 ± 0.5	4.1 ± 0.4	0.91 ± 0.02	0.61 ± 0.01

Figure 3.5.23: Electrical characterization and device performance analysis. The EQE of the orange (b) and green-blue (c) PC-based perovskite solar cells is reported, compared with the EQE of a reference nonphotonic structured SiO_2 scaffold-based perovskite solar cell ((a)). The grey areas shows the regions where PC-based cells show high reflectance. (d-g) Box-plot of the device performance indicators for the different PC-based cells: (d) short-circuit current density (J_{sc}), (e) open circuit voltage (V_{oc}), (f) power conversion efficiency (PCE), and (g) fill factor (FF). (h-j) Photographs of the fabricated devices showing (h) blue, (i) green, and (j) orange colours. [48]

Nanoporous one-dimensional photonic crystals for coloured dye-sensitized solar cells In 2012, Colonna et al. reported the fabrication of dye-sensitized solar cells integrated with a one-dimensional photonic crystal (1DPC) structure exploited both as a light trapping and colour filtering layer.[52] The cells were prepared depositing by screen printing a TiO_2 film on top of a conductive FTO glass substrate. On top of this, the 1DPC structure was fabricated by alternating SiO_2 and TiO_2 layers, deposited by spin coating of nanoparticle suspensions. Then the structure was immersed into a dye solution and then the counter-electrode was fabricated by spin screen printing of colloidal platinum paste on top of a conductive FTO glass. Then the liquid electrolyte was inserted into the device. The prepared devices displayed different colours when observed from the front and rear contact side, with the colours depending on the thickness of the layer building the 1DPC structure as well as on the corresponding refractive indexes. It was observed that the cell appearance showed

high dependence on the incidence angle. Moreover, it was showed that the integrated 1DPC structure, besides acting as a colour filtering layer, allowed also an increase in the short circuit current, thanks to the fact that a portion of the non-absorbed photons are reflected back to the active layer by the PC structure. Relative increase in the short circuit current up to 44 % with respect to the reference cells was reported, obtaining a maximum photocurrent of around 8 mA/cm^2.

3.6 Morpho butterfly inspired coloured BIPV modules

In 2017, Bläsi et al. reported an promising technique inspired by the structural colours characterizing the wings of Morpho butterflies to achieve large, uniformly coloured PV modules with a good independence from the angle of observation.[53] Morpho butterfly's wings showed a 3D structure made of vertical ridges with horizontal lamellae attached to them. The structure shows an high level of complexity since the lamellae are almost equidistant from each other while the ridges to which they are attached to, do not seem to follow any regularity. The horizontal lamellae act as a Bragg grating causing interference in the incident light while the finite width of the ridges cause the angular spread by diffraction. The ridges' height irregularity suppresses the interference effects between the ridges by reducing the spatial correlation between the ridges[54]. In figure 3.6.24 a schematic image shows the structure of the butterfly wings and the effects related to its components. This

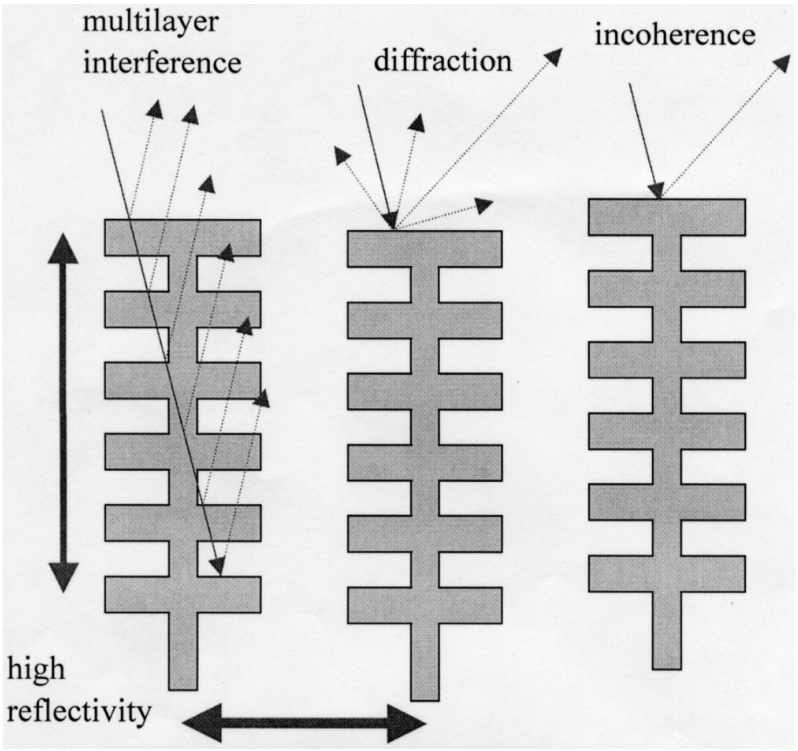

Figure 3.6.24: Schematic representation of the microscopic structure characterizing the Morpho butterfly wings and the optical phenomena related to the visualize structural colour. (figure from [54])

highly complex structure is hard to manufacture with the right accuracy but it was demonstrated that the same effect can be achieved by depositing a multilayer Bragg grating on a substrate with defined roughness[55].

In order to integrate the functional layer in the PV module, the photonic structure was applied to the rear surface of the module glass, being sandwiched between the glass and a laminate sheet. This allows to integrate the functional layer in the production of the PV module by simply changing the front glass with a combination

of glass and the photonic structure. The front surface of the glass can be either planar or textured to reduce glare effects. In figure 3.6.25, a sketch of the structure of the PV module including the functional layer is shown.

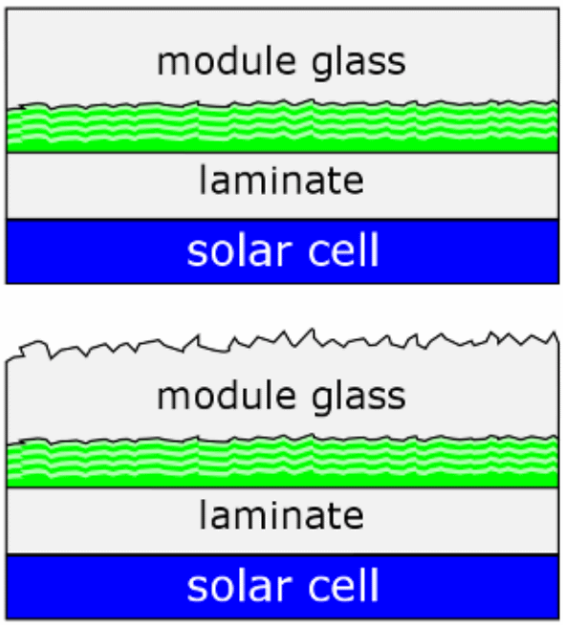

Figure 3.6.25: Schematic representation of the proposed design. The colouring layer (green) is sandwiched between the module front glass (flat or textured) and the laminate. (figure from [53])

Three cover glasses with different colour filters were fabricated. Red, blue and green colours were achieved. In figure 3.6.26 (left), a cover glass with a green filter is applied to a mini PV module by using a water film to avoid the formation of air gaps between the layers. On the left side of the glass, the filter is not applied and the dark grey cell is visible. The rest of the cell show a uniform and bright green colour, result from the applied filtering glass.

This glass was studied with angle dependent spectrometric reflectance measurements. The results are shown in figure 3.6.27(left). The reflectance spectra for different angle of incidence show a resonance peak around 550 nm. Moreover, for angles up to 50°, the peak only slightly shift to lower wavelengths, showing a good independence on the viewing angle. The same is confirmed in figure 3.6.27(right), where the measured reflectance spectra (for blue, red and green glass filter) are represented in CIE chromacity diagram. The higher shift observed for an angle of 60° was explained by the enhanced overall reflectance caused by the rear interface. In figure 3.6.26 (right) are shown the photograph of three coloured demonstrator modules compared with an uncoated one.

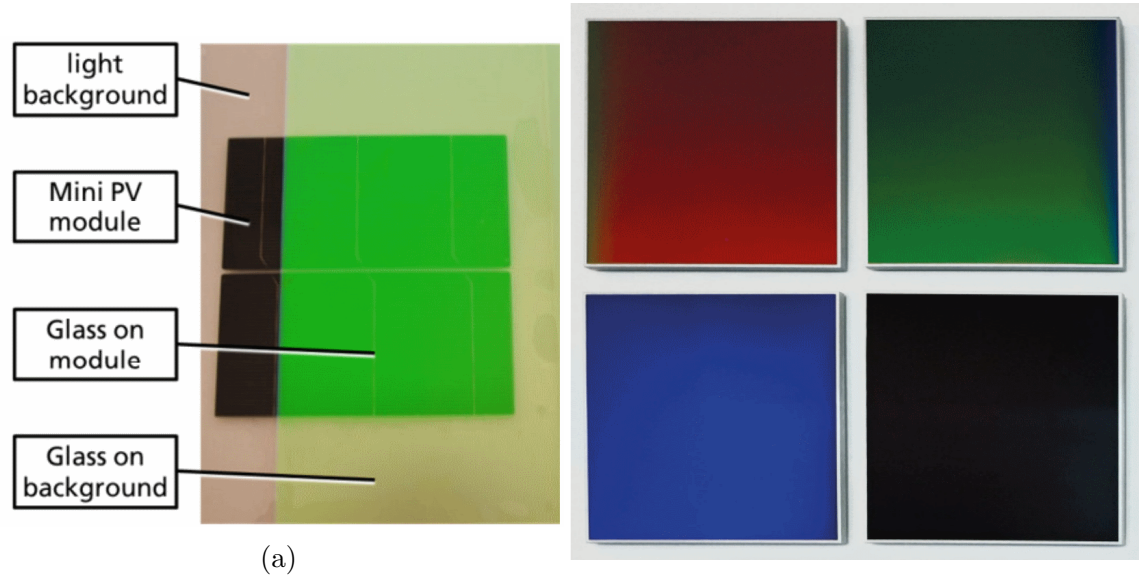

(a) (b)

Figure 3.6.26: (a) Photographs of the a mini-module covered with the colouring structure, applied with a water film. The uncovered part (left) shows the actual colour of the solar cell while the rest of the picture shows the resulting colour of the cell covered with the filter. (b) Photographs of the demonstrator modules where the contacts are made invisible. Three different colours are shown compared to an uncoated (black) module.(figure from [53])

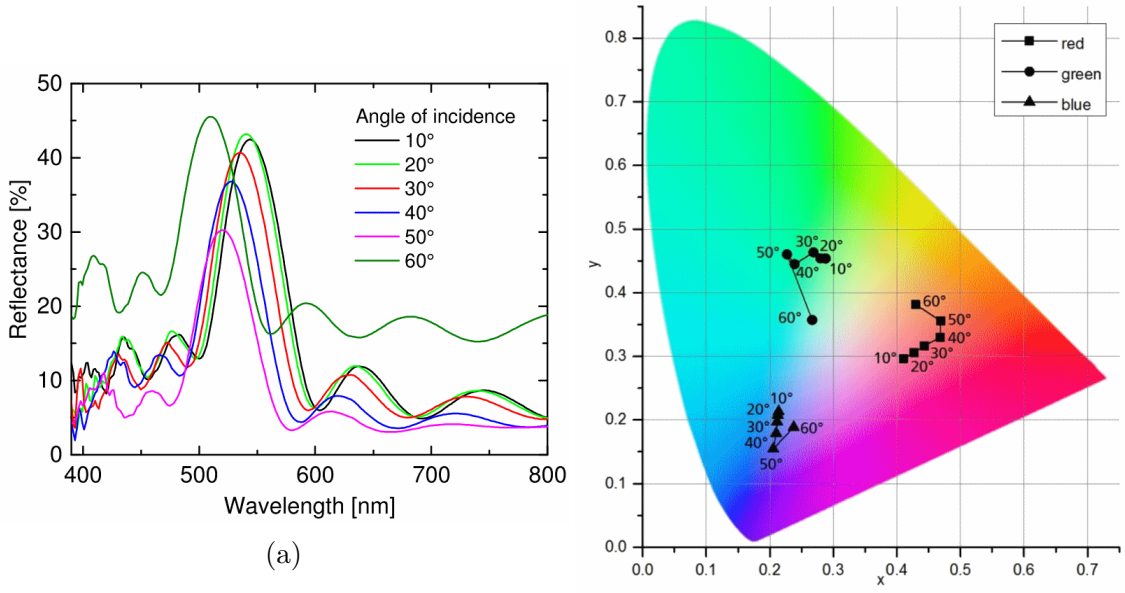

(a) (b)

Figure 3.6.27: (a) Measured reflectance spectra with respect to the angle of incidence for a class panel with a green colour layer. (b) Representation in the CIE chromacity diagram of the measured reflectance spectra of blue, green and red panels. (figure from [53])

In order to avoid the electrical interconnection between the cells to be visible,

back contact solar cells were used and the connectors were blackened. Moreover a low-reflective and deep-dark back-sheet foil was applied.

It was reported that the relative loss of generate solar power was around 7 %, with respect to the uncoated cover glass. No further information about the electrical performances of the produced modules was reported.

3.7 Summary

From the information gathered on the different proposed nanophotonic approaches for colourful solar cells, some general considerations can be made. In particular it was observed that the best results in terms of photovoltaic performance were obtained when the colouring filter was integrated in well-known and established photovoltaic technologies such as crystalline solar cells. This comes naturally from the fact that the colouring structure affects the solar cell operation mainly optically, reducing the amount of light being actually converted into electric power, so, if the starting structure is already well performing a better final result is reasonably expected.

Among this group, the absolute best data in terms of power loss was obtained with a double-layer anti-reflective coating but reasonably good results were obtained also by exploiting the resonant dielectric nanoscatterers. For what matters the coloured cells fabricated by sputtering the dielectric surface with metallic nanoparticles, not enough data were reported regarding the electrical characterization of the final devices, making it difficult to give an evaluation in this sense.

From the point of view of the visual appearance of the coloured devices, it was observed that, in general, these techniques, based on silicon solar cells, allow realizing mostly earthlike colourings, somewhat lacking in brightness and purity. A bright green colour was indeed realized through the dielectric nanoscatterers array, but no more information were given regarding the flexibility in the colour selection.

In this sense, much better results were observed when the colouring structure was integrated in the starting design of the solar cell, as for the case of the perovskite solar cells integrated with nanoporous photonic crystals, or of the thin-film optical cavity where tha amorphous silicon functioned both as absorbing media and as part of the design of the filter. The downside in this case was that much worse results in terms of performance of the final device were observed so that additional work will be needed to optimize these multifuntional devices making them attractive for real life applications.

Very promising appears the last reported approach, where the colouring filter is realized by mimicing the structural features of the morpho butterfly wings. In this case bright and uniform green, blue and red panels were obtained, simply positioning the realized coloured glasses on top of standard silicon solar modules. Even if no information was reported on the electrical characterization of the final coloured devices, a relative efficiency reduction of 7 % with respect to the uncoated glass was claimed which is very promising considering that highly efficient established solar panels were used.

From the point of view of the ease of integration of the proposed techniques in the photovoltaic manufacturing process, at the present moment, the most promising

routes are definitely to be found in the in the integration of the colouring filters with the well established silicon solar cells. In these cases, the integration of colour filters would virtually represent only an additional step in the manufacturing process of the standard photovoltaic devices. On the other hand, this would need a high level of product diversification which could be cost-inefficient if the demand for these device would be insufficient.

For all these reason, in the following sections a new approach will be analysed and proposed, based on the colour filtering properties of three dimensional photonic crystals. These structures show high, narrow-band reflectance peaks in the visible range, being tunable by changing the diameter of the building particles so that bright pure colours can be obtained. Moreover, outside of the material optical stob-band, low parasitic absorbance levels are observed.

4 Photonic crystals

In the previous sections, the most relevant studies aimed to realize colourful solar cells have been introduced. Many differences can be highlighted and each of them have advantages and drawbacks that make them more or less interesting in terms of applications.

In this work the attention have been directed especially towards structure that would work as optical filters yielding reflective colours. In particular, those structures that could be realized in a standalone procedure and then incorporated in the final steps of the manufacturing line of solar cells and module, of any kind. With this goal, a promising route would be to exploit the peculiar optical properties of photonic crystals (PCs), combining the self-assembling properties of nanoparticles with the facile pattern fabrication achievable by ink-jet printing. These structures have attracted more and more attention in the last decades for their ability to treat light as semiconductors treat electrons.

In the following sections the physical behaviour of photonic crystals will be introduced, giving the fundamental informations needed to understand how they works. The theoretical description will focus in particular on 3-dimensional (3D) photonic crystals since this is the kind on which the proposed solution is base on. Then a summary of the recent literature reporting studies on PCs will be given and then a new proposal of using this structures to obtain reflective colour filter for solar cells will be presented.

4.1 Theory

The perception of colour that we have is the results of an electromagnetic radiation stimulating the cone cells of our eye, producing a specific reaction, directly correlated to the wavelength(s) of light. In the majority of cases, the colour of objects depends on the portion of the visible light spectrum that is not absorbed by the material but is reflected and reach our eyes. There are cases though when not the absorption/reflection phenomena produce colours, but the scattering of light. This happens for example when the light is scattered by the air molecules in the sky: the small particles scatter light in all direction, but the smaller the wavelength the higher the amount of scattering, producing the well known blue colour (Rayleigh scattering)[56]. Another example is the scattering of light by particles whose size is bigger than the Rayleigh length, described by Gustav Mie. This is the case of colloidal dispersions such as milk[57]. When scattering of light is combined with interference phenomena, the so-called diffraction is observed. This is what happens in photonic crystals.

In general, a photonic crystal is an ordered crystalline structure within which a periodic modulation of the index of refraction is observed. Many examples of these structures can be found in nature but different artificial techniques of preparation have been realized. They can be divided into three types depending on their geometry: one-dimensional, two-dimensional and three-dimensional photonic crystals have been observed. The discriminant here is the number of directions in which the modulation of permittivity occurs.

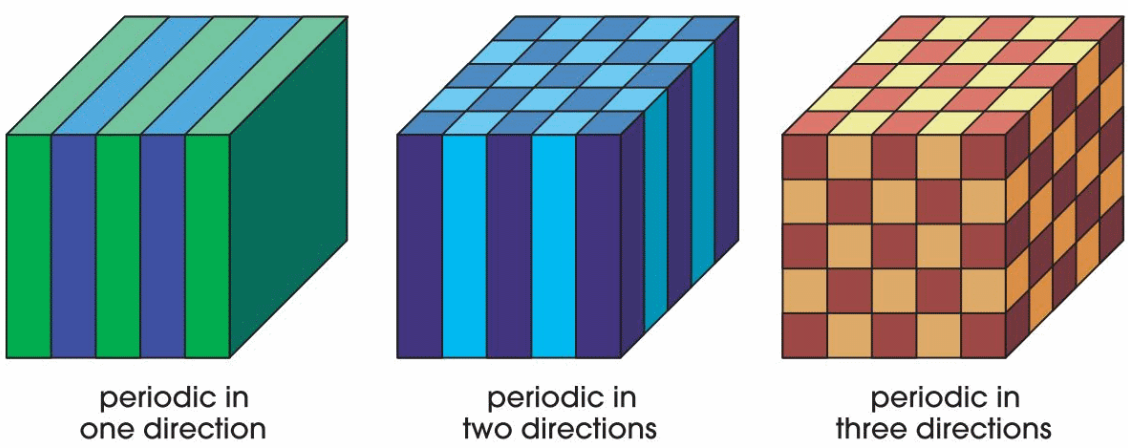

Figure 4.1.1: Schematic representation of 1-, 2- and 3-dimensional photonic crystals. The alternating colours represent materials with different dielectric constants. The periodic alternation of this constant in space give PCs their peculiar properties. (figure from [58])

In figure 4.1.1, the schematic representation of the different spacial periodicity found in PCs is reported. A fibre Bragg grating is an example of the 1D photonic structure. Here a structure formed from multiple layers of alternating materials with varying refractive index is constructed in a short segment of an optical fibre so that it reflects particular wavelengths of light and transmits all others[59]. Well-known examples of the other two types can be found in nature. An example of 2D photonic structures can be found on the hair-like setae covering certain types of polychaete worms. Here each seta shows an hexagonal lattice of voids which works as pseudo-photonic fibre causing a strong Bragg scattering[60]. An example of the effect of a 3D photonic crystal is given by the changing colours of the valuable stone opals. The microstructure of an opal consists of a number of microspheres arranged in a face centred cubic configuration and the modulation of the refractive index is observed in all direction. In this case, the effect is strongly angle-dependent and based on the observing orientation, different colours are observed.

The particular configuration of the scattering centres forbids some wavelengths to propagate through the medium. All these structures have in common a well ordered, periodically arranged structure which is also what it is observed in crystalline semiconductors. At the same time, looking at the behaviour of photons in photonic crystals and electron in semiconductor materials, a fundamental similarity is observed: the periodic modulation of the refractive index in a PCs acts on photons, as the periodic potential, within a semiconductor, acts on electrons. It is known that electrons in a crystalline semiconductor can be considered, in a simple approximation, as a free gas of particles under the influence of the periodic potential build by the crystal lattice. In this approximation, an energy band structure can be defined combining the energy and the wavevector of electrons propagating through the material. It is known that in semiconductors, an energy band gap exists between the valance and conduction band, defining a range of energies at which electrons cannot propagate within the semiconductor. The same applies to photonic crystals,

also called photonic bandgap materials (PBM), only here the periodic potential is replaced by the periodic refractive index and electrons are replaced by photons.

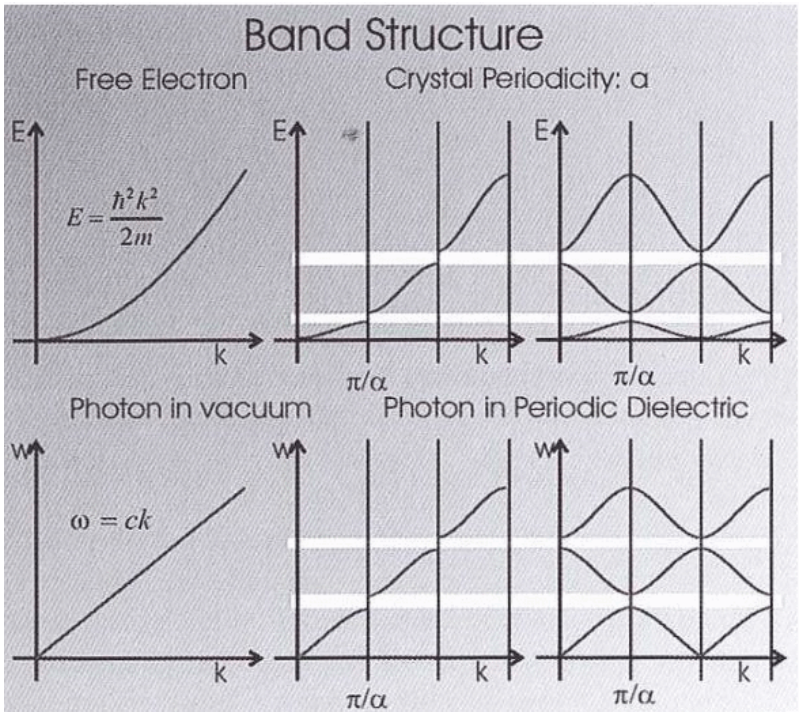

Figure 4.1.2: Examples of band diagrams for free electrons and electrons confined in a crystal lattice (top) and for photons in vacuum and in a periodic dielectric. (figure from [61])

In figure 4.1.2 a comparison between the band diagrams for electrons and photons is presented. Here it is clear the similarity between the two structures, with the energy bandgaps for both "particles" (electron and photons) highlighted in white. Another analogy with solid state materials is the phenomenon of X-ray scattering from their crystalline structure. Here X-rays are strongly absorbed by solid matter, except for a range of X-ray energies where the wavelengths of the radiation are comparable to the lattice spacing. In this cases, the radiation can be reflected if the Bragg condition is satisfied. The same selectivity in reflection is observed for PCs with the difference that here, the phenomenon happens at different orders of magnitude for the wavelengths since it depends on the particle diameter and the lattice planes spacing which is much higher in PCs. Following the same derivation of the Bragg condition for X-ray scattering it is possible to derive the Bragg law modified for the optical region.[62]

In figure 4.1.3 a schematic representation of the scattering of light between two lattice planes in a photonic crystals allows to derive geometrically the Bragg conditions for reflection modified for the optical region: the refractive index must be taken into account. Here two lattice planes and the physical paths of and incident beam of light with wavelength λ scattering inside the material are represented. Light is both reflected and refracted. An approximation is made considering that before the first

layer there is only air, refractive index $n_0 = 1$, and then a medium with an effective refractive index n_{eff} is encountered. This is a rather strong approximation since the three dimensional structure of the PC is not considered. Nevertheless, the Bragg condition that is derived is the one more often used to describe the relation between the reflection peak and the particle dimension of 3D photonic crystals.[63][64][65][66]

The derivation is done calculating the optical path Δ for the two waves going from A to D and A through B to C. The required condition to have constructive interference is that the optical path is equal to any integer value of the wavelength, $N\lambda = \Delta$. The optical path Δ is defined as the refractive index of the medium times the physical path:

$$\Delta = n_{eff} \cdot \delta. \tag{9}$$

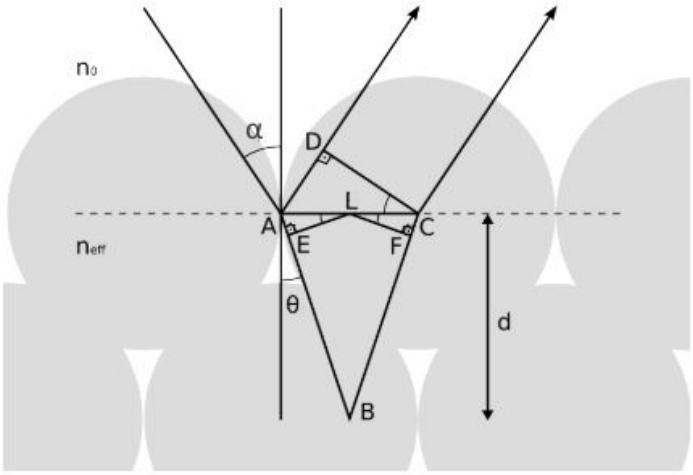

Figure 4.1.3

Looking at the picture, the physical path is:

$$\delta = ABC - AB = 2AE + 2EB - AD. \tag{10}$$

The triangles ADC and AEL are similar, and the ratio between corresponding sides is 2. This said:

$$\delta = E - 2EB - AD = AD + 2EB - AD = 2EB. \tag{11}$$

The segment EB is related to the interplanar spacing:

$$EB = d\cos(\theta). \tag{12}$$

Where θ is the Bragg angle. Now remembering the Snell law, $n_0 \sin\alpha = n_{eff} \sin\theta$,$n_0$ is the refractive index of air, n_{eff} is the effective refractive index of the PC, α is the incident angle with respect to the surface normal and θ is the Bragg angle, one finally have:

$$\Delta = n_{eff} \circ \delta = n_{eff} \circ 2EB = 2n_{eff} d\cos(\theta) = 2n_{eff} d\sqrt{1 - \sin^2\theta} = \tag{13}$$

$$= 2n_{eff}d\sqrt{1 - \frac{\sin^2\alpha}{n_{eff}}} = 2d\sqrt{n_{eff}^2 - \sin^2\alpha}. \quad (14)$$

where the air refractive index n_0 was considered equal to 1. Finally putting this together with the interference condition, $N\lambda = \Delta$ one have the Bragg's law modified for the optical region:

$$\lambda = 2d\sqrt{n_{eff}^2 - \sin^2\theta_i}. \quad (15)$$

Here N is taken equal to 1. If the wavelength of the incident light satisfy equation 15, the beam is reflected and cannot propagate through the material. Is is clear how this condition depend on the angle of incidence of the incoming light. The effective refractive index for such a structure is calculated by effective medium approximations (EMAs). There are different models that could be applied. One of them is Bruggeman's model which is usually applied for systems mad of multiple spherical components. In general, all these approximations assumes that the medium is homogeneous and have an effective refractive index which comes from the combination of the indexes of the components. In the case of 3D photonic crystal considered here, Bruggman's the effective refractive index is calculated from:

$$\Phi_{void}\frac{n_{void} - n_{eff}}{n_{void} + (d-1)n_{eff}} + \Phi_{part}\frac{n_{part} - n_{eff}}{n_{part} + (d-1)n_{eff}} = 0 \quad (16)$$

Here Φ_{void} and Φ_{part} are the volume fractions of the material filling the void between the particles and the volume fractions of the particles building the crystal, respectively. n_{void}, n_{part} and n_{eff} are the refractive indexes of the material filling the void, of the particles and the effective refractive index and d is the system dimensionality[67].

Due to their unique behaviour, photonic crystals find a number of different application to be implemented on their basis. Their ability of selectively scatter light make them interesting in applications where it is useful to control and manipulate light flow. Uses of photonic crystals can be found in the field of low and high reflection coatings on lenses and mirror in the form of thin-film optics as well as in manufacturing paints and inks with the ability of change their colour. Moreover, the properties of PBG material are responsive to change in external condition such as temperature or humidity. Patterns of responsive colloidal photonic crystals (CPCs) with multicolour shifting properties have been developed by inkjet printing mesoporous colloidal nanoparticle ink on a substrate. In these structures, the mesopores proportion of nanoparticles have been precisely adjusted so that, when exposed to vapour, the colour of these patterns would change[68].

4.2 Literature review

Many studies reported the implementation of colourful patterns realized by ink-jet printing of photonic crystals. Exploiting the abilities of nanoparticles of self assembling in ordered crystalline structure, by ink-jet printing it is possible to direct write, on several substrates, light modulating structures useful in many applications. In 2016, H. Nam et al. showed that anti-counterfeit marks and signatures could be realized by printing monolayers of self-assembled PCs, showing low visibility under daylight on a white substrate but recognizable on a black substrate under strong illumination (e.g direct flash light) [69]. In 2014, L. Bai et al. reported the realization of vapor responsive patterns made of colloidal PCs, by ink-jet printing mesoporous particles which optical response would change if exposed to water vapor, showing a colour switch in the printed image, useful for applications in dynamic displays and again in anticounterfeiting patterns.[70] In both these cases patterned PCs where successfully printed but some of the qualities generally desirable, in terms of coloured solar cells applications, are missing. A strong reflectance under daylight as well as a certain angle independence is usually desired, as discussed in some of the techniques reported in the previous chapter. In this direction, some relevant studies on ink-jet printed photonic crystals will be analysed, summarizing the most important results and findings.

4.2.1 Reflectivity and crystalline structure

The work developed by J. Park et al. in 2006 sets a relevant starting point. They reported the fabrication of arrays of hemispherical CPCs by ink-jet printing.[71] A scanning electron microscopy (SEM) image of the arrays is shown in figure 4.2.4.

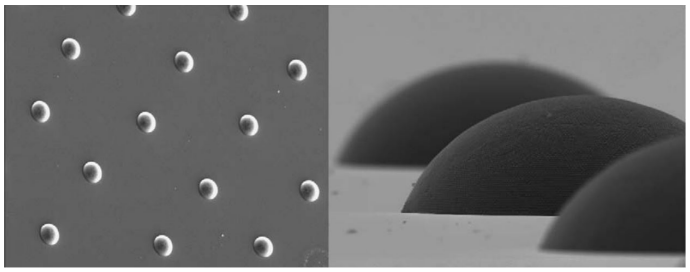

Figure 4.2.4: SEM images of the realized PCs arrays (figure from [71])

Within the domes, the printed particles, after the solvent evaporation, self-assemble in an highly ordered structure showing the typical optical behaviour of 3D photonic crystals. It was shown, inter alia, that the reflectance spectrum of the colloidal assemblies was directly dependent on their crystalline structure which, in turn, depends on the size of the building particles. In particular, the reflectance of a single dome was measured by microreflectance spectroscopy. In figure 4.2.5 are shown the reported reflectance spectra, in arbitrary unit, with respect to the building particle size and the wavelength of the incident light. The different spectra correspond to PCs domes made with different sized particles. Each one showed a peak in the reflectance at a wavelength that change when the particle size is changed. In this

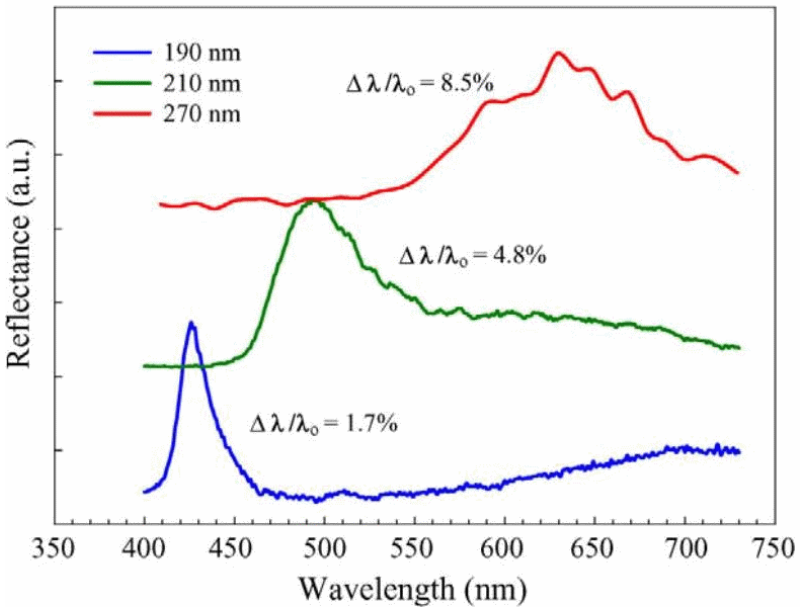

Figure 4.2.5: Reflectance spectra of the microdomes with respect to particle size and light wavelength. (figure from [71])

work, particles with diameters of 190, 210 and 270 nm were used and reflectance peaks at wavelengths of 426, 494 and 639 nm were found, respectively. These results were in accordance with the reported optical micrographs shown in figure 4.2.6. The domes showed bluish, blue-greenish and reddish hues if observed in reflection, as expected from the position of the reflectance peaks. Another relevant optical microscopic image was reported and shown in figure 4.2.6.d. Here the PCs array was clearly recognizable and blue and red coloured dots were observable.

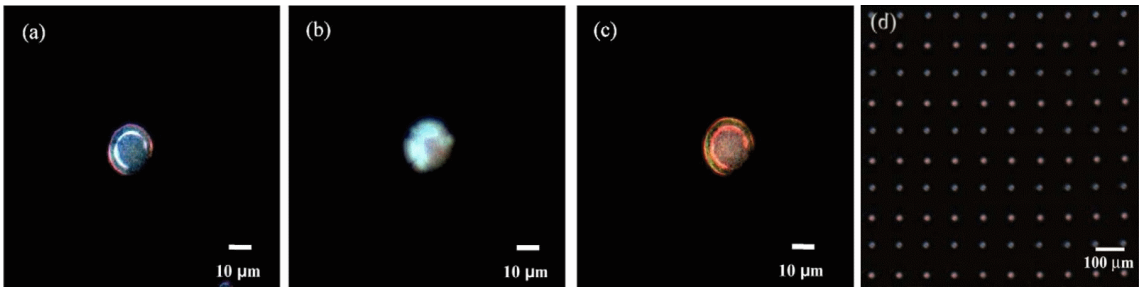

Figure 4.2.6: Optical micrographs of the printed microdomes. From left to right the size of the building particles is 190 nm (a), 210 nm (b) and 290 nm (c). Optical microscopy image of the PCs array showing blu and red hues corresponding to particles with 190 and 290 nm diameter (d). (figure from [71])

A consistent result was reported by L. Cui et al. in 2009. Here larger patterns were created by ink-jet printing colloidal PCs as it can be seen in figure 4.2.7.a.[72] Again different colours were obtained using different sized building particles. Figure 4.2.8 shows the SEM images of the patterned region (particle size of 280 nm): it is clear how the particle self-assembled in a ordered crystalline structure and again,

the dome shape of the printed assemblies was observed. It is also clear how the crystalline structure (and therefore the particle size) was strictly connected to the reflectance spectrum of the patterned regions, reported in figure 4.2.7.b. When the diameter of the building particles was increased the peak position in the reflectance spectra shifted to higher wavelengths. In particular for particles with a diameter of 180, 220 and 280 nm, peaks at wavelengths of 465, 541 and 646 nm, respectively, were found.

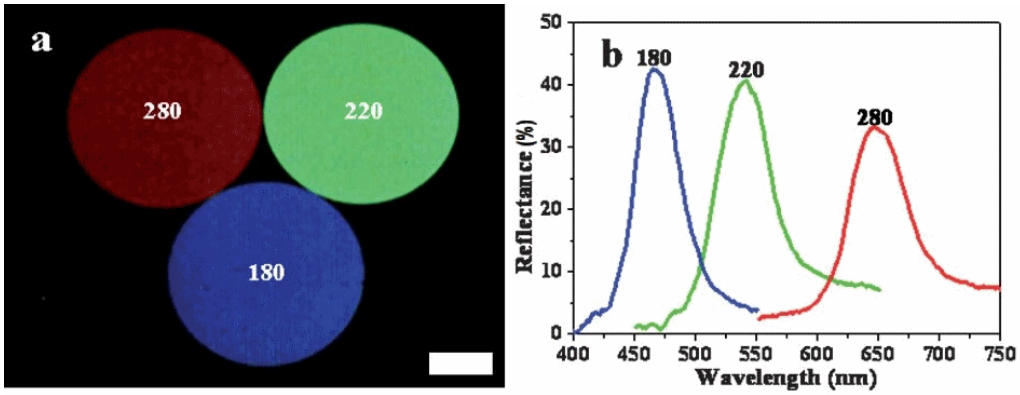

Figure 4.2.7: PCs patterned area showing tre different colours (scale bar 1 cm) (a) and relative reflectance spectra (b). (figure from [72])

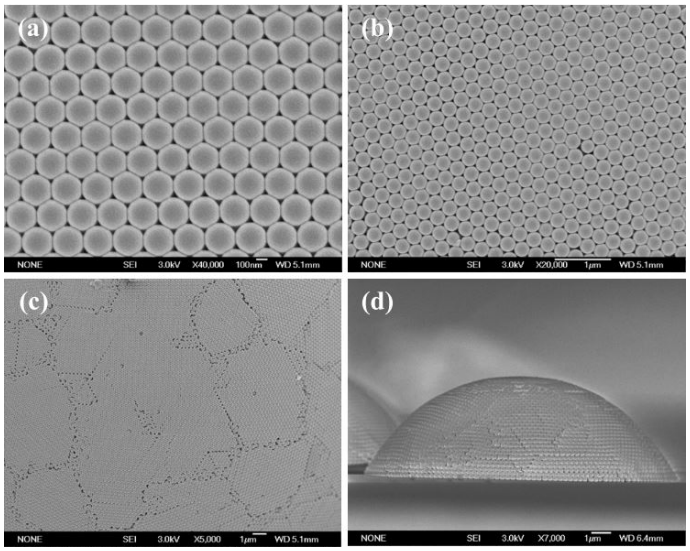

Figure 4.2.8: SEM images of the printed PCs. The top (a)-(c) and side (d) view confirm that the building particles (diameter of 280 nm) self-assemble in a ordered structure. (figure from [72])

A third relevant study was reported in 2014 by M. Kuang et al. Again, patterns and arrays of dome-shaped CPCs were prepared by ink-jet printing using three different sized particles, as it can be seen in figure 4.2.9.[73] The optical microscopy images showed the arrays of domes reflecting three different colours depending on the particle size. The SEM images showed once more that the particles self-assemble

in an highly ordered way. In figure 4.2.10 the reflectance spectrum corresponding to crystals having different sized building particles. In this case, even if not explicitly specified, the high level of measured reflectance suggests that the spectra have been obtained sampling single dots by microreflectance spectroscopy. Here, using particle with a diameter of 190, 223 and 281 nm, stopband positions at 466, 522 and 648 nanometers have been found.

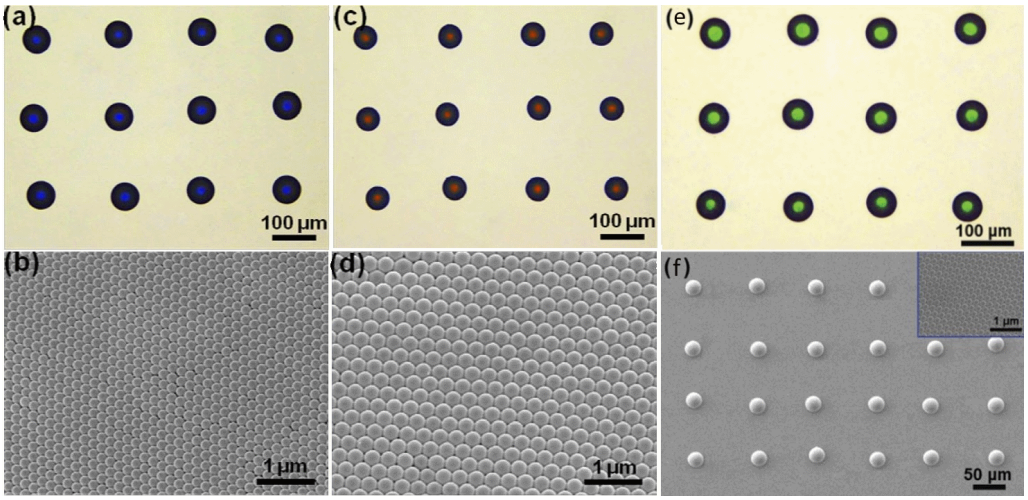

Figure 4.2.9: Optical microscope images of the printed CPCs domes (190 nm (a) , 281 nm (c) and 223 nm (e) and corresponding SEM images (b), (d) and (f), respectively. (figure from [73])

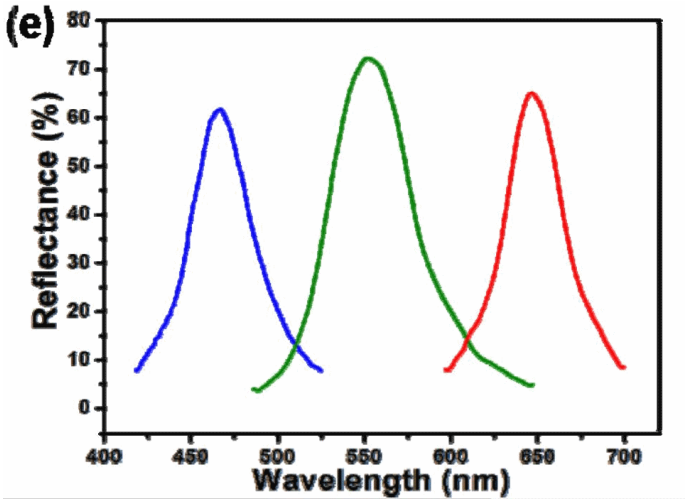

Figure 4.2.10: Reflectance spectra of the printed CPC. (figure from [73])

These results confirmed the expected behaviour of three dimensional photonic crystals, introduced theoretically in section subsection 4.1. The optical response of the printed aggregates was strongly connected to their crystalline structure. In all three studies, spherical polystyrene particles were used as building elements and it was observed that they self-assembled in a face centred cubic (FCC) crystalline structure. More about the ink formulation, printing and assembling process will be

discussed in the next section. Now let us keep the focus on the correlation between the so-called stop-band position (the position of the reflectance peak) and the crystalline structure of the printed aggregates. Recalling the Bragg law modified for the optical region, we expect that the position of the stopband is proportional to the interplanar spacing within the crystal:

$$\lambda_{peak} = 2d_{hkl}\sqrt{n_{eff}^2 - \sin^2\theta_i}. \tag{17}$$

Here λ_{peak} is the stopband position, n_{eff} is the effective refractive index of the crystal (see subsection 4.1), θ_i is the incident angle of light and d_{hkl} is the spacing between the crystal planes identified by the Miller indexes (hkl). In this case, a FCC crystalline structure is formed and the light impinges on the (111) plane. This means then:

$$\frac{1}{d_{hkl}^2} = \frac{1}{a^2}(h^2 + k^2 + l^2)d_{111} = \frac{a}{\sqrt{3}} = \frac{4r}{\sqrt{3}}\frac{1}{\sqrt{2}} = \frac{2D}{\sqrt{6}} \tag{18}$$

where a is the side of the cubic cell, and r is the radius of the particle (see figure 4.2.11). Finally, from the Bragg law:

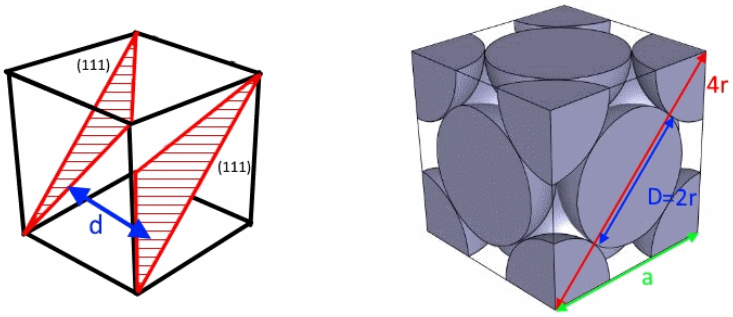

Figure 4.2.11: The (111) planes and the spacing between them (left) and the close packing of the (non-primitive) FCC unit cell with characteristic dimensions (right)

$$\lambda_{peak} = \frac{4D}{\sqrt{6}}\sqrt{n_{eff}^2 - \sin^2\theta_i} \tag{19}$$

where D is the particle diameter. Choosing particles with different diameter allows to tune the reflectance peak to the desired wavelength, selecting then the colour that the aggregates reflect when illuminated. Park et al. reported also that the broadening of the reflectance peak increase as the particle diameter is increased, as it can be seen in figure 4.2.5. This results was connected to the crystal quality of the aggregates, that would decrease for crystals built with bigger particles. The same effect, slightly less noticeable, can be recognized in the results reported by Cui et al. (r4.2.5.b. A strong connection between the degree of order within the crystal and the shape and position of the reflectance peak is evident.

4.2.2 Printing process, ink formulation and crystal formation

In figure 4.2.12 it is represented schematically the printing process: the colloidal ink droplets are jetted from the printhead nozzles; during the solvent evaporation (drying), the building particles self assemble in the dome shaped photonic crystals, previously shown in figure 4.2.4. As for the inks, generally colloidal suspensions are

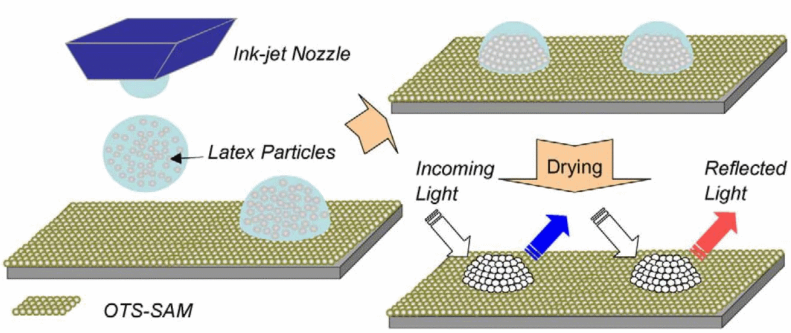

Figure 4.2.12: Schematic representation of the ink-jet printing of hemispherical photonic crystals. (figure from [71])

prepared dissolving monodispersed particles in a main solvent (usually water) to which certain additives can be added to control the solution properties, e.g. surface tension, boiling point and viscosity. These parameters have an important influence in terms of ink suitability for printing (should be tuned to fit the requirements defined by the printer manufacturer) and deposition process since they affect the wetting behaviour, the solvent evaporation and drying time of the ink droplets[74]. All the works previously considered reported the use of polymer latex suspensions as inks. Park et al. prepared an ink mixing mondispersed polystyrene particles (1.6 vol%) in a solvent of 70 wt% water and 30 wt% formamide. Then octyl alcohol was added to control surface tension. An ultrasonic treatment followed by a filtration (5-μm nylon mesh) was then performed. A similar formulation was used by Cui et al. in the fabrication of the large patterns showed in figure 4.2.7. Here core-shell latex spheres were prepared via batch emulsion polymerization. These particles are showed in figure 4.2.13 and have an hydrophobic polystyrene core surrounded by a poly(methylmethacrylate) (PMMA)/polyacrylic acid (PAA) shell. This more

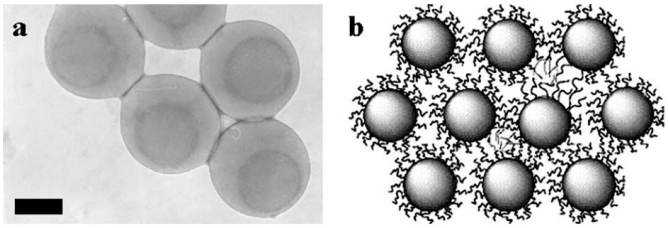

Figure 4.2.13: Transmission electron microscopy (TEM) image (a) and schematic representation of the core-shell poly-(St-MMA-AA). Scale bar 100nm. (figure from [72])

complex structure was chose to exploit the so called "paint on" effect: the shell coil

elasticity provide an additional assembly force that speed up the assembling process [75]. A water based latex suspension, with a particle concentration of 20wt%, was obtained and used as ink to perform the first printing tests, that showed a relation between the reflectivity of the patterned region and the ink contact angle (CA) of the substrate, as shown in figure 4.2.14.a.

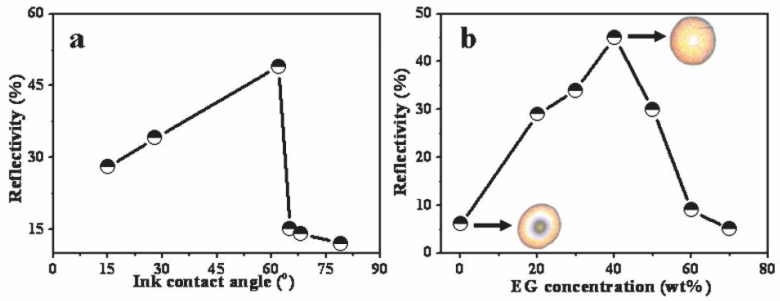

Figure 4.2.14: Relation between reflectivity peak and ink-substrate contact angle (a) and between reflectivity peak and ethylene-glycol (EG) ink concentraton (b). Inserts in (b) are the optical microscope images of the samples with EG contents of 0 and 40 wt% respectively (figure from [72])

It was found that increasing the contact angle, the reflectivity would increase. This phenomena was connected to the better crystalline quality of the printed latex aggregates. If substrates with an higher contact angle are used, the droplet spreading area decrease, suppressing the so called coffee-ring effect: when the initial substrate CA is low, during evaporation this angle decrease but the drop contact area remains almost the same, leading the particles to the perimeter of the this area. This way, ring-like aggregates will form[76][77]. As the contact angle becomes higher, the drying process is followed by a reduction of the contact radius, and hemispherical aggregates are more likely to be observed, with an higher degree of crystalline order. This leads to an higher reflectivity. In figure 4.2.14.a it can be observed that the reflectivity reached its maximum for a contact angle of 62° and then dropped for higher angles. This behaviour was linked to the fact that an higher contact angle leads to lower contact area that cause, inevitably, a lower coverage area of the printed region. This happens if the spacing between two dots is not reduced, i.e. the dot density is not increased. The importance of the ink CA on the substrate will be investigated in more details in the next section, where the problem of the viewing angle independence will be considered.

In figure 4.2.14.b, the relation between the reflectivity and the etylene glycol concentration (EG) of the ink is shown. In order to further reduce the coffee ring effect, an high boiling point solvent was added to the ink. Such an additive act as a drying control agent by producing Maragoni flow [74]. The surface tension gradient induce the Maragoni flow and if a solvent with low surface tension and high boiling point is user, the flow will be counterclockwise, and the drying solvent will transport particles to the center of the droplet, preventing the righ-shaped deposit pattern. In this case, ethylene glycol, EG (boiling point 198°C) was added to the ink and it was found that increasing its concentration, the homogeneity of the aggregates would improve, leading to an higher reflectivity, as shown in figure 4.2.14.b. The high boiling

point of EG also slows down the drying process and facilitate the self-assembling of the latex spheres, reaching an higher degree of crystalline order[78].

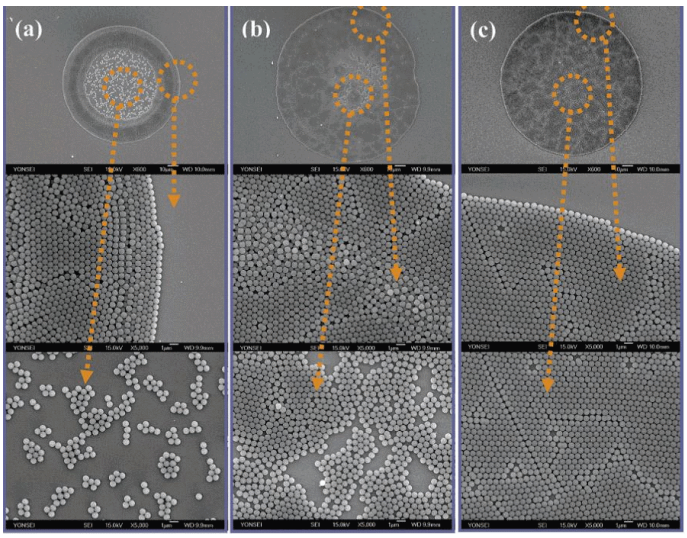

Figure 4.2.15: SEM images of deposit patterns using silica particle-based inks on an hydrophilic Si wafer: (a) water-based ink; (b) water/diethylene glycol (DEG)-based ink; and (c) water/ formamide (FA)-based ink. The ink concentration was 4 vol % for all three inks. (figure from [79])

In figure 4.2.15, SEM images of deposit patterns obtained with different inks compositions are shown; using an water-based ink, the drying process leads to coffee rings patterns, with the particles aggregating near te perimeter of the droplet; if higher boiling point solvents are used, e.g. diethylene glycol (DEG) and formamide (FA) (boiling points 245 and 210 °C, respectively), more homogeneous and ordered aggregates are observed. The decrease in the reflectivity observed for EG concentration higher than 40 wt% was attributed to a too much high dilution of the latex suspension.

Finally it is worth mentioning the ink formulation used by Kuang et al. Also in this case monodispersed polystyrene particles were dispersed into mixing solvent of deionized water (60 wt%) and ethylen glycol (40 wt%) which was used as the high boiling point solvent and with latex concentrations ranging from 3 x 10-4 wt% to 15 wt%,

4.2.3 Wide viewing angle and substrate contact angle

Until now the relation between the stopband position of the printed PCs and the angle of the incident light, described in the optical Bragg law 19, have not been considered. The fact that the reflectance peak position change when PCs are illuminated from different angle is one of the main properties of these materials. It terms of appearance the result is that a photonic crystal structure will show a different (structural) colour when observed from different angles. This behaviour is sometimes useful in terms of applications (e.g. anti-counterfeiting marks) but represent a problem if one desire to produce an optical coating that reflects a uniform and angle independent colourful pattern.

In this direction H. Gu at al. reported in 2013 the fabrication of angle independent photonic crystals made by replication of colloidal crystal beads (CCBs) showing spherical symmetry.[80] In figure 4.2.16.a the optical images of the CCBs array is shown while in figure 4.2.16.b the surface of a single bead is shown by SEM imaging.

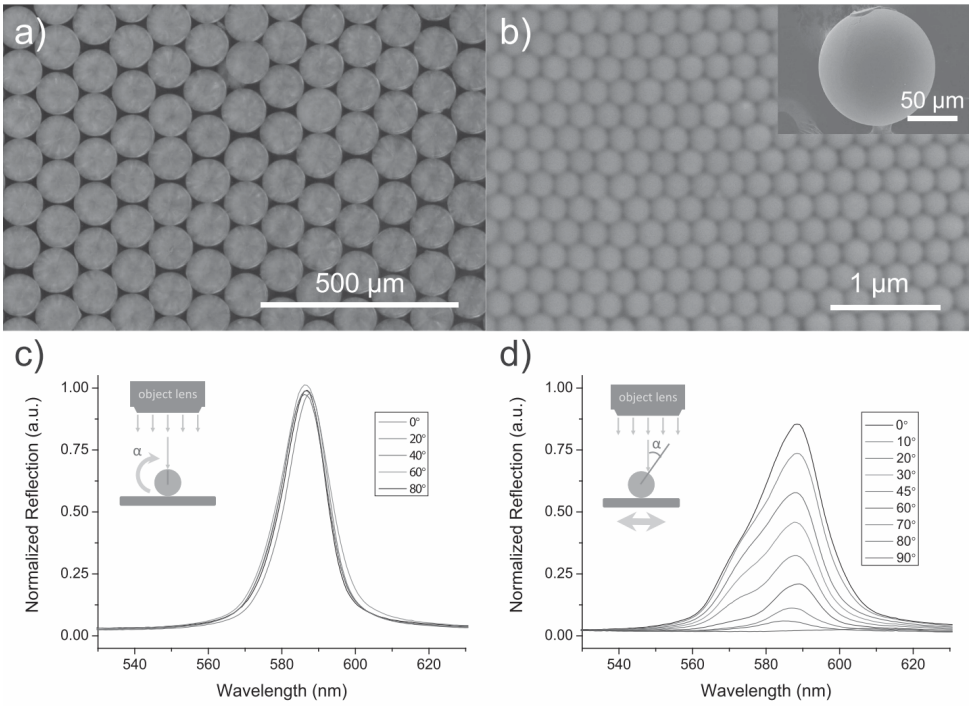

Figure 4.2.16: Optical images of the arrays of colloidal crystal beads (a) and SEM images of the surface of a single bead (b). Reflectance spectrum of a single bead detected from different surfaces (c) and from different position under the lens of the microscope. (figure from [80])

The beads were prepared from microfluidic colloidal droplet templates using silica particles as building materials. During the drying process, the colloidal nanoparticles in the droplets self-assemble into spherical aggregates, showing high crystalline order. It was observed that the particle on the beads surface assembled with hexagonal symmetry and the same ordering extended to the centre of the beads. The optical properties of the beads were characterized using microscope equipped with a fibre optic spectrometer. In figure 4.2.16.c the normalized reflection spectra taken from different surfaces are reported. The beads showed an almost identical reflection spectrum at different detection angles. Moreover, the reflection peak position would remain the same even if the beads were put at different locations in the viewing field of the microscope, as it is shown in figure 4.2.16 and confirmed from the optical microscope images shown if figure 4.2.17. The different values shown by the reflection peaks were ascribed to the non-uniformity of the incident light, which intensity decreased from the centre to the edge of the viewing field.

These results suggest that the spherical symmetry can be exploited to obtain photonic crystal structures that retain their optical appearance even from different observation angles. Similar findings were reported by M. Kuang et al. in their work on ink-jet printed dome-shaped CPCs, mentioned in the previous sections. It was

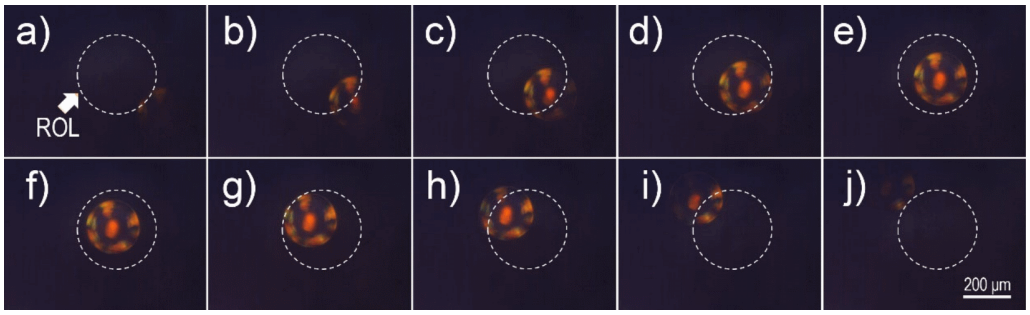

Figure 4.2.17: Mycroscope images of yellow CCB at different position under the region of the light spot (ROL). (figure from [80])

found that increasing the high-to-diameter (H/D) ratio of the printed domes, the reflectance peak position remains unchanged if detected from different angles. In particular, the best results were found with an H/D close to 0.5, i.e. if the domes becomes similar to hemispheres, the optical behaviours result again independent on the detection angle. Again the relation between spherical symmetry and angle independence is observed. In figure 4.2.18.a the position of the reflectance peak is reported with respect to the detection angle, for PC domes with different H/D ratios. As said, the best result is obtained for a H/D ratio close to 0.5, but good level of independence is found already at a value of 0.375. The same results are confirmed in figure 4.2.19, where the variation of the reflectance spectrum with respect to the detection angle is shown for three different H/D ratios. Moreover, the photograph reported in figure 4.2.19.d, show how the dome-shaped PCs patterns reflect a constant green colour at different detection angles.

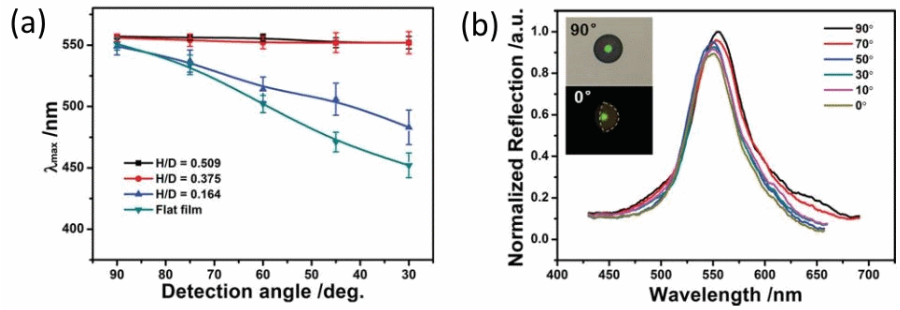

Figure 4.2.18: a) Reflectance peak position variation with respect to the detection angle, at different H/D ratio. b) Reflectance spectrum at different detection angles fot PC domes. Insets are the top-view (up) and side-view (down) otpical microscopy images of a single PC dome. (figure from [73])

In order to understand how to control the H/D ratio of the printed domes, tests were performed printing latex based PCs on different substrates with different contact angles. The results are reported in figure 4.2.20. It was shown that when the contact angle of the substrate increase from 18°± 5.7°, 39°± 4.9°, 67°± 3.6° to 93°± 1.9°, the H/D ratio increases from 0.0328, 0.0769, 0.164 to 0.509. This behaviour comes from the fact that in if the ink contact angle on the substrate is high enough, the sliding

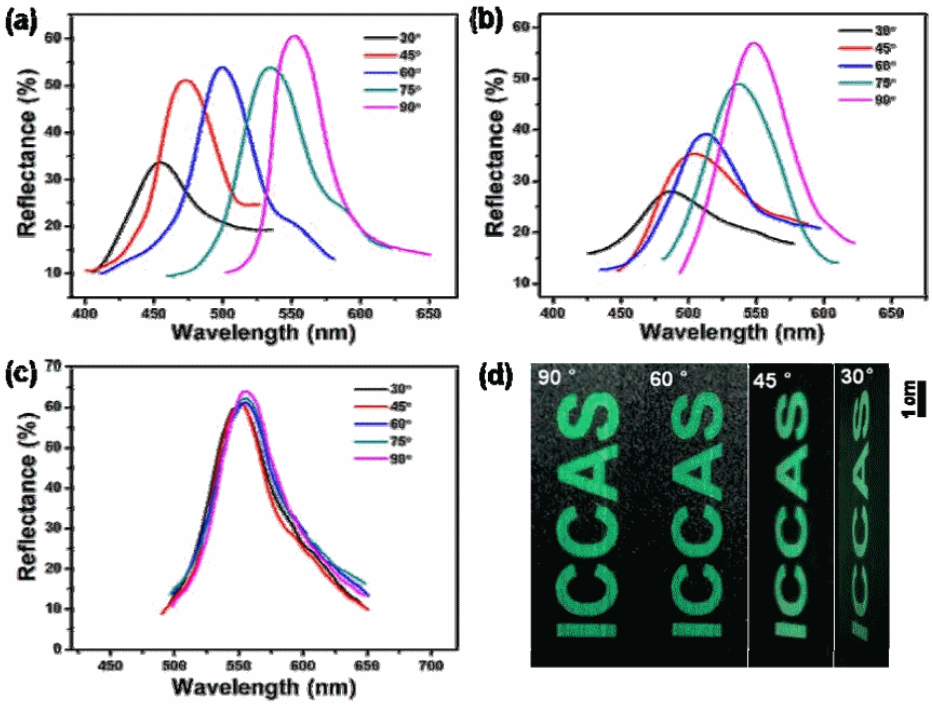

Figure 4.2.19: Reflectance spectrum of (a) flat PC film, (b) printed PC domes with H/D ratio of 0.164 and (c) printed PC domes with H/D ratio of 0.375. (d) Photographs off patterned PC domes taken at different viewing angles. (figure from [73])

of the three phase contact line (TCL) is observed, i.e. the contact line between ink, air and substrate moves toward the centre of the drop, leading to a smaller contact area, forcing the particles to aggregate in a hemispherical shape rather then a flat film. This behaviour is confirmed in figure 4.2.20.e, where the relationship between the ratio of final deposit dimension to initial deposit dimension and the receding contact angle. It is clear how with contact angles higher than 26°, the TCL start to slide instead of being pinned, leading to dome-shaped aggregates.

Different substrates have different wettabilities and in order to change the ink contact angle, this wettability must be adjusted. This can be done by treating the substrates with different surfactants. Octadecyltrichlorosylane (OTS) is a chemical often used as a coating on glass or plastic substrates and increase their hydrophobicity.

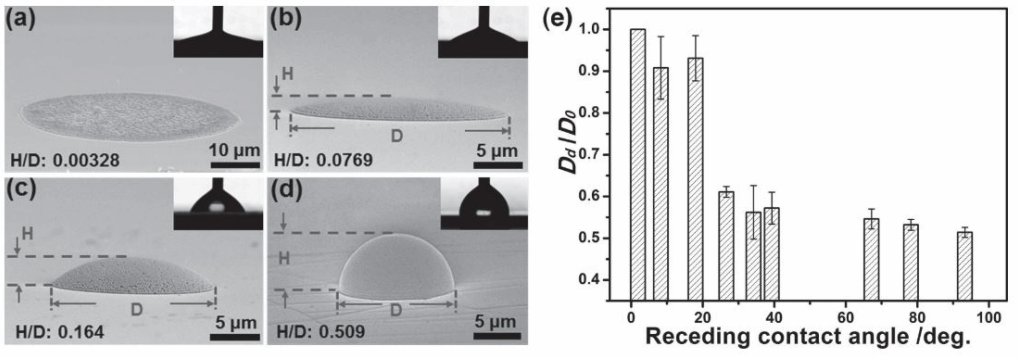

Figure 4.2.20: SEM images of the deposited PC on substrate with contact angles of (a)18°± 5.7°, (b) 39°± 4.9°, (c)67°± 3.6° and (d) 93°± 1.9°. (e) Relation between the ratio between the final and initial deposit diameter with respect to the substrate contact angle. (figure from [73])

4.3 Summary

From the analysed literature it was found that three dimensional photonic crystals can be realized by ink-jet printing, using colloidal inks based on dielectric nanoparticles as silica or latex. The printed PCs show vivid and uniform structural colour in reflection. The colour of the printed structures can be selected using different sized nanoparticles as building material. By controlling the ink contact angle on the substrate and the ink formulation, it is possible to realize hemispherical shaped aggregates that shows high crystalline order as well as angle independent reflectance. These properties suggests that ink-jet printed photonic crystals can represent a novel solution to realize optical filters that can be integrated in high efficiency solar cells in order to freely engineer their visual appearance reducing the optical losses (due to the colouring layer) to a minimum, since the colouring is achieved by reflecting a narrow band of the light spectrum rather then through absorbing phenomena.

5 Experimental part

In addition to the literature review on the nanophotonic approaches for colourful solar cells, this work includes an experimental part aimed to reproduce some of the findings from the literature on inkjet-printed three dimensional photonic crystals (PC), reported in the previous section, to evaluate if this technology can represent a viable option for the fabrication of colourful photovoltaics.

First, patterns of three-dimensional, dome-shaped PC aggregate were prepared by inkjet printing. Then the optical properties of the fabricated samples were characterized by means of an optical microscope and a UV-VIS-NIR spectrometer. After this, the effect the prepared structures the solar cell performance as a colouring layer was investigated by means of external quantum efficiency measurements.

5.1 Drop-On-Demand Piezoelectric Inkjet Printer

For the preparation of the PC patterns, a FUJIFILM Dimatix Material Printer DMP-2850 was used. With this printer, fluidic materials can be deposited on many different rigid or flexible flat substrates (e.g. plastic, glass, ceramic, silicon). The most relevant specifications of the instrument are hereby symmarized, as reported by the manufacturer[81]:

General features

- Flat substrate, xyz stage, inkjet deposition system
- User-fillable piezo-based inkjet print cartridges
  - Capacity: Up to 1.5 ml
  - Materials Compatibility: Many water-based, solvent, acidic or basic fluids
  - Number of nozzles: 16 nozzles, 254 spacing, single row
  - Drop volume: 10 pL (also 1 pL option is available)
- Built-in drop jetting observation system
- Fiducial camera for substrate alignment and printed quality checking
- Variable jetting resolution and pattern creation PC-controlled with Graphical User Interface (GUI) application software
- Printable area: 210 mm x 260 mm
- Substrate thickness: Up to 25 mm
- Software editors: pattern, piezo drive waveform, cleaning cycle, substrate setting

5.2 Materials

Based on the information gathered from the literature, it was decided to use polystyrene microspheres as building materials for the PC. A monodisperse polystyrene

suspension was purchased from Polysciences, Inc.[82] The dispersion characteristics, as reported from the manufacturer are:

Polystyrene particle dispersion (Polysciences, Inc)

- Mean diameter and standard deviation: 0.20 ± 0.01 μm
- Particle concentration: 2.5 % solids (w/v)
- Solvent: aqueous suspension with minimal surfactant

In addition to the polystyrene dispersion, in the final ink formulation a certain percentage of etylene glycol (CH_2OH_2) was added as a high boiling point surfactant, to decrease the surface tension of the final solution and to slow down the evaporation of the printed droplets (see subsubsection 4.2.2).

The formulated ink was printed on a glass substrate treated with octadecyltrichlorosilane (OTS, chemical formula $CH_3(CH_2)_{17}SiCl_3$) since an high ink/substrate contact angle was desired in order to obtain dome-shaped, highly ordered photonic crystal aggregates (see subsubsection 4.2.3). Common microscope glass sides were covered with OTS by atomic layer deposition (ALD). The coated glasses showed advancing and receding contact angles of 98º and 80º, respectively.

5.3 Preparation

Ink formulation For the ink formulation, the recipe reported by Kuang et al. will be considered as a main reference (see subsubsection 4.2.2). For clarity, we report it here as it was given in the reference paper: "The printing inks were prepared by dispersing the polystyrene particles (with latex concentration of 3 x 10-4 wt% - 15 wt%) into mixing solvent of deionized water (60 wt%) and ethylene glycol (40 wt%). The ink was treated ultrasonically and filtrated through a 1.5 μm nylon mesh before use."[73]. Here, a relation between the polystyrene concentration C and the final size of the printed dome was reported (figure 5.3.1). It was decided to follow the work of Kuang et al. as a reference since the inkjet printer used for the domes preparation was very similar to the one available in our case, making the obtained results easily comparable. It was decided to set the goal for the final particle concentration to 10 wt%. It was observed, during the preparation, that an higher concentration could lead to a final ink with a too high viscosity, with the risk of exceeding the limits declared by the printer manufacturer or in general making the printing process more difficult to optimize. It must be pointed out that, for the sake of this work, where a simple proof of concept is sought, a full comprehensive characterization of the prepared ink was omitted.

The purchased polystyrene dispersion had a starting particle concentration of 2.5% solids (w/v). For this reason, first the dispersion was partially evaporated at 70°C in order to increase the particle concentration. Then, being the particle dispersed in water, a 40% of etylene glycol was added to obtain the final ink composition. Finally, the solution was filtered with a 5 μm nylon filter before being directly used to fill the printer cartridges.

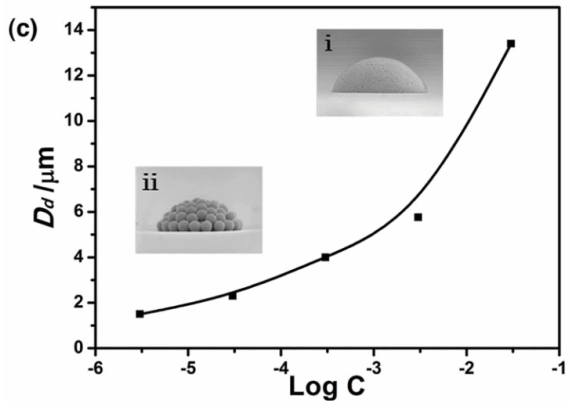

Figure 5.3.1: Relationship between the final diameter Dd of the printed PC domes and the logaritm of the particle consentration C of the ink. The insets show the SEM images of the printed domes with diameter of (i) 13.3 μm and (ii) 1.6 μm, obtained with a particle concentration of 3wt% and 3x10^{-4} wt%, respectively (figure from [73])

Dome-shaped PC patterns The first step was to optimize the cartridge setting with respect to the prepared ink (see subsection 2.2). With the software provided by the printer manufacturer it is possible to accurately modify the voltage waveform applied to the piezolectric elements of the cartridge as well as change the maximum voltage applied to each one of the cartridge nozzles. In figure 5.3.2 is shown a configuration that worked well with the prepared ink, providing a uniform drop jetting. In figure 5.3.3 the drops formation process obtained with the reported setting is shown. As it can be seen, the drop formation and volume is rather uniform between different nozzles.

With the reported settings, several patterns of inkjet-printed PC were prepared. The primary parameter to be adjusted is the distance between the printed domes (dot spacing). The Dimatix DMP 2850 allows to adjust the dot spacing in the range from 5 μm to 254 μm, the latter being the distance between two nozzles. The spacing variation is achieved by horizontally rotating the cartridge (manually activated rotating scale) by an angle calculated by the software once the dot spacing is selected. By setting different drop spacing it is possible to change the distance between each printed dome.

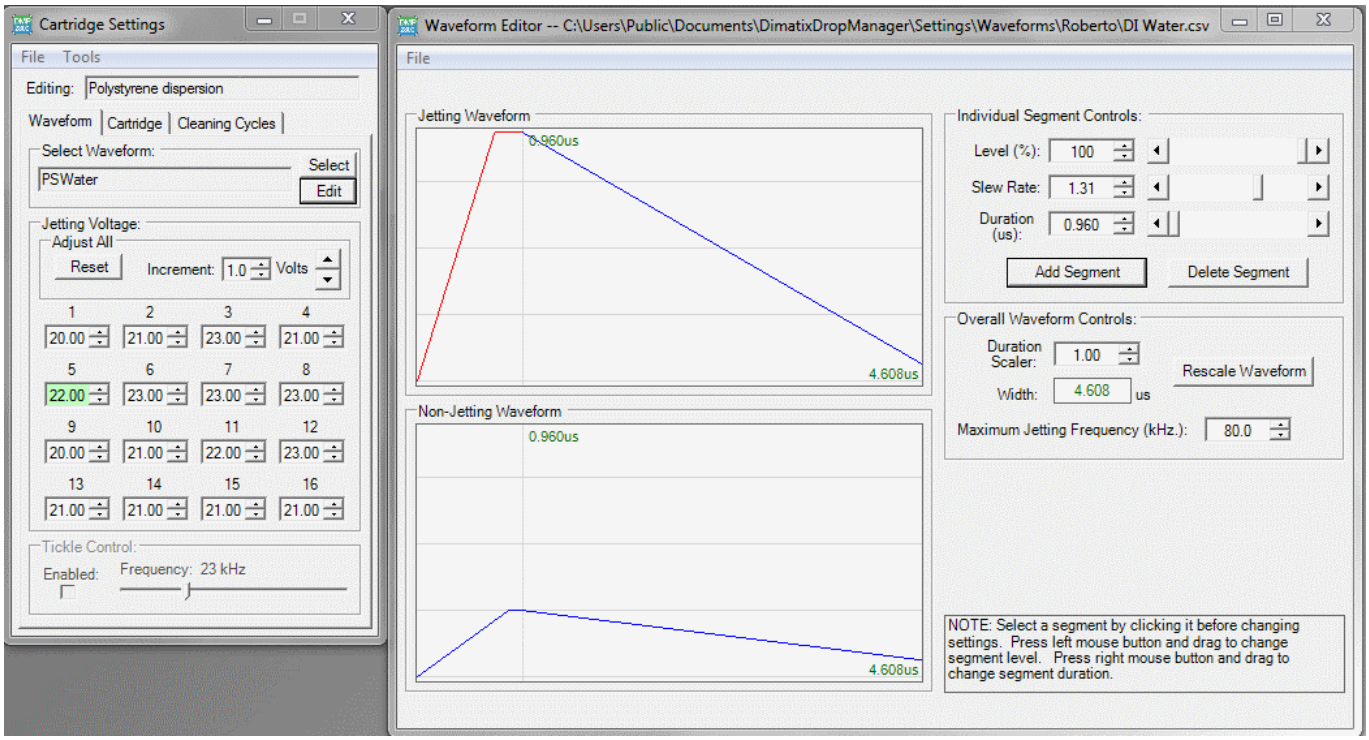

Figure 5.3.2: The cartridge settings (left) as well as the waveform applied to the piezoeletric elements of the cartridge (right) are shown.

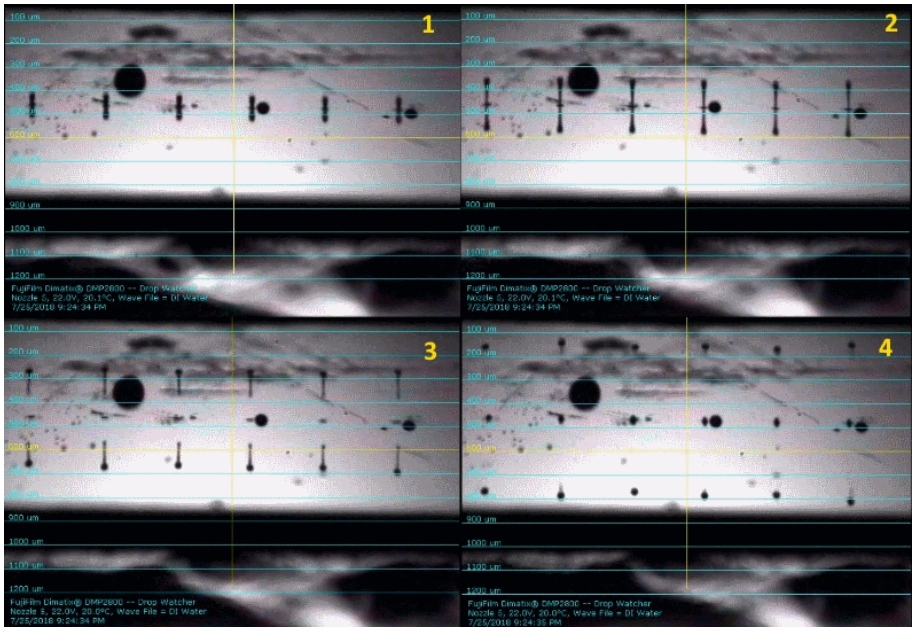

Figure 5.3.3: Drop jetting obtained with the applied waveform photographed at four different consecuting moments. Uniform drops are formed travelling with the same vertical velocity.

The minimum achievable distance between two printed domes is strongly related to the impact behaviour of the ink drops on the surface as well as the evaporation process (see subsection 2.2). In figure 5.3.4, an optical microscope image of the inkjet-printed domes is shown. In this case, a drop spacing of 50 μm was imposed. This led to the formation of different sized domes resulting both from the evaporation of single drops of ink as well as from the merging of multiple drops. It is also possible to identify the maximum spreading area reached by each ink drop before the evaporation of the solvent (green circles). Measuring their dimensions it was found that the domes resulting from single ink drops have a final diameter of around 20 μm. The ratio between the diameter of the initial spreading area with respect to the final diameter of the corresponding dome was rather uniform for each dome and equal to around 2. From these observations it is clear that if the imposed dot spacing is too low, domes with different sizes will form from the merging of multiple drops, affecting the uniformity of the printed arrays.

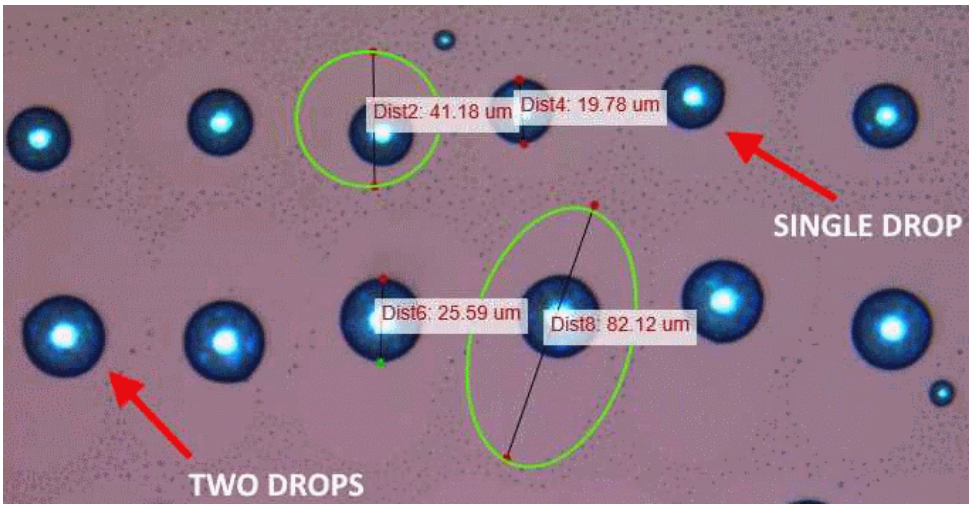

Figure 5.3.4: Optical microscope image of the printed PC domes. Domes resulting from single ink drops as well as from the merging of multiple drops can be observed. The diameters of two different sized domes are shown as well as the diameter of the maximum spreading area of the droplet before the evaporation of the solvent (green circles).

To overcame this problem and at the same time increase the dome density on the substrate (reducing the dot spacing), it was decided to perform successive prints, setting a larger dot spacing and shifting the starting point at each print. The strategy is represented schematically in figure 5.3.5. A drawback in this case could be that a certain time must be waited between two prints so that the evaporation process reduces the drop volume and some space is "freed up" for the drops printed in the second stage.

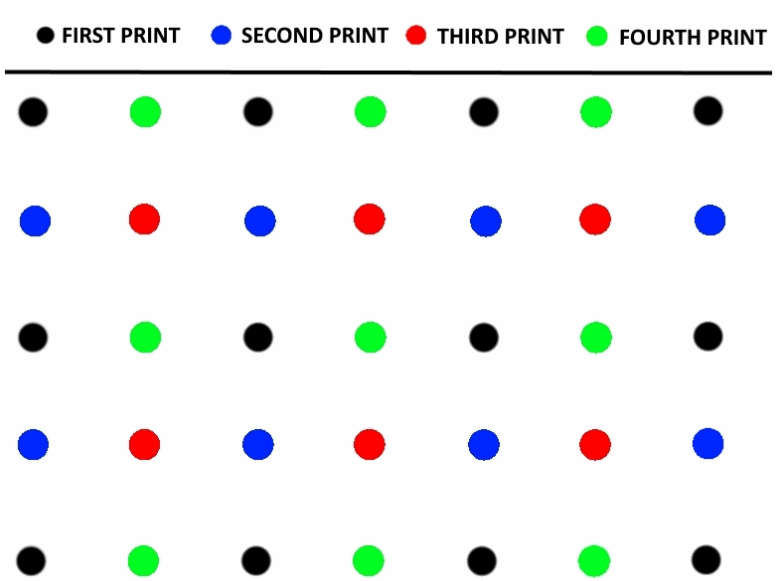

Figure 5.3.5: Printing strategy to avoid drop merging while reducing the spacing between the domes. The same pattern is printed in successive prints, changing each time the starting point.

With the proposed strategy, pattern of dome-shaped photonic crystal were printed on a glass substrate. The optimized samples had a dot spacing (mean) of 42.8 μm, a dome density of 53141 domes/cm^2 with a mean dome diameter of 18 $\pm$ 0.15 μm and were obtained by performing two successive print with dot spacing of 60 μm shifting, the second time, the starting point of 30 μm in x and y directions.

5.4 Measurements

Optical characterization Optical microscope images of the fabricated PC patters were collected with a Leica DM4500 optical microscope, investigating the printing quality as well as the structural features of the printed domes. Some of the results reported in the reference literature were successfully reproduced.

The optical properties of the samples were inspected performing spectrometry measurements with a UV-Vis-NIR Agilent Cary 5000 spectrometer. The total hemispherical reflectance of the PC patterns were collected and compared with the results reported in the literature. Angle dependent reflectance measurement were not possible with the available instrument and this feature will be investigate qualitatively with optical microscope measurements at different angles.

Electrical characterization The characterization of the solar cells integrated with the fabricated PC patterns, exploited as colouring coatings, was performed with a QEX7 Solar Cell Spectral Response/Quantum Efficiency/IPCE Measurement System from PV Measurements, Inc. A high-efficiency monocrystalline silicon cell was used as a reference. The EQE spectrum of the bare cell was collected as well as the short circuit current density J_{sc}. The effect on the cell performances of the

colouring layer were investigated measuring the EQE and the J_{sc} both for the cell covered with the bare glass slides and with the fabricated PC colour filters.

6 Results

Optical characterization of the printed dome-shaped PC The optical properties of the final samples were investigated collecting the total hemispherical reflectance spectra. In figure 6.1, the reflectance spectra of the PC patterned glass are reported and compared with the values for the bare glass substrate. It is clear how the PC patterns acts as an optical filter in the visible region, showing a reflectance peak at 467 nm (11.3%), with a relative increase with respect to the bare glass of around 3% (at the peak). In the infrared region, the reflectance results slightly

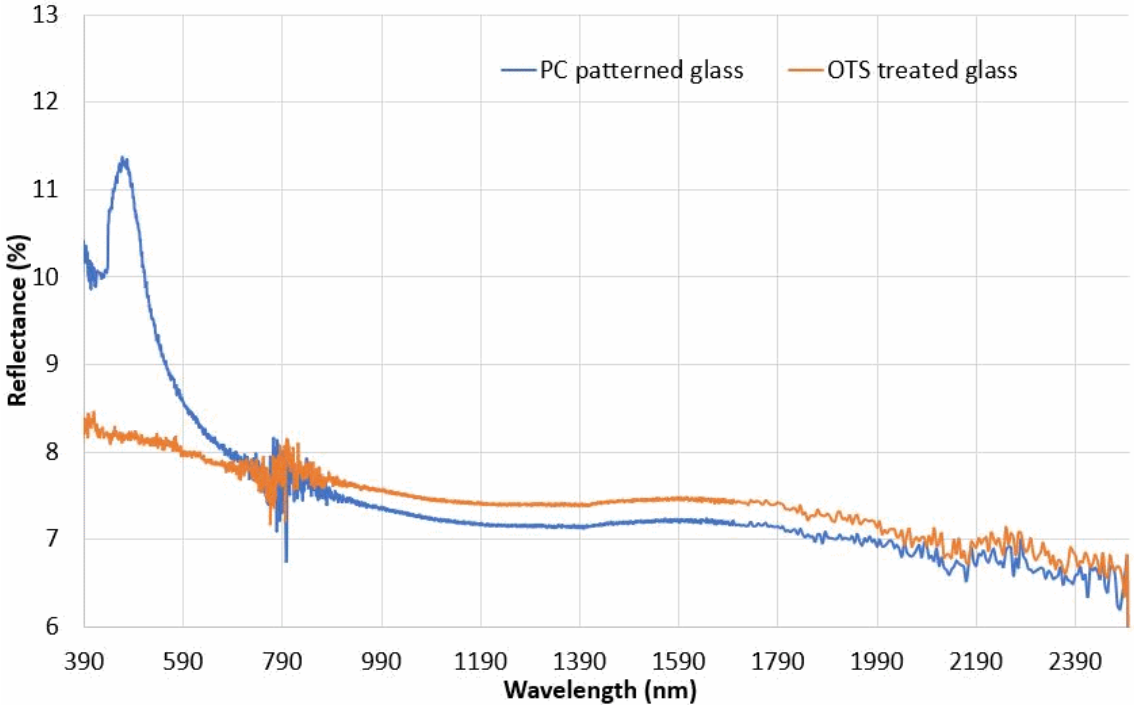

Figure 6.1: Total hemispherical reflectance of the PC patterned glass substrate (blue line) compared to the reflectance of the bare glass (orange line). The prepared samples shows a peak in the reflectance at 467 nm. The reflectance in the infrared region is slightly reduced compared to the values for the bare glass

reduced (1%) with respect to the bare glass while in the ultraviolet part of the spectrum, an increase in the reflectance starts to appear, probably caused by the scattering between the radiation and the polystyrene particles building the domes. It can be noticed that the reflectance value, at the peak wavelength, is very small if compared to the results published in the reference literature, where values between 40% and 70% (peak) were reported (see subsubsection 4.2.1). On the other hand, from the data published in the reference papers, it was unclear whether the reported reflectance spectra referred to the single PC domes or to the whole PC patterned areas.

Some more information can be gathered analysing in details the composition of the samples fabricated in this work. In figure 6.2, an optical image of the final PC pattern is reported. It can be observed how the dome do not cover the whole substrate

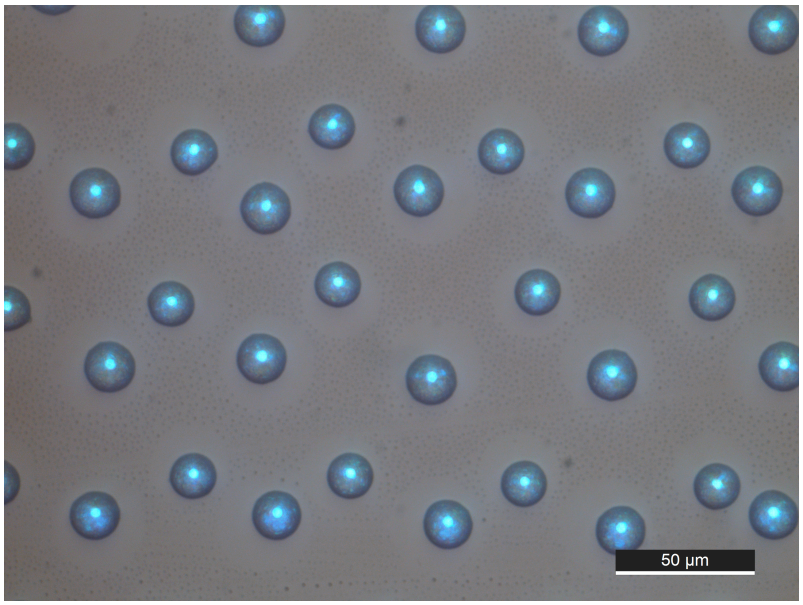

Figure 6.2: Optical microscope image of the printed domes. The medium diameter of the domes is 18 ±15 μm. The dome density was 5.31 x 10 ^{8} domes/cm^{-2} with a mean dome diameter of 18 ±0.15 μm. The domes reflects visible light showing a colourful appearance.

surface. In particular a dome density of 53141 domes/cm^2 was achieved, obtaining a dome coverage area of around 13.5 %. For this reason, an approximation was proposed considering that the total sample reflectance is the result of the combination of the reflectance of the single domes (on glass) with the reflectance of the glass substrate, weighted by their surface coverage fraction. Then the total reflectance of the samples can be expressed as:

$$R_{tot} = \phi_{dome} R_{dome-glass} + (1 - \phi_{dome}) R_{glass}, \tag{20}$$

where R_{tot} is the total sample reflectance, ϕ_{dome} is the surface fraction covered by the domes, $R_{dome-glass}$ is the reflectance of the dome-covered glass area and R_{glass} is the reflectance of the bare glass substrate. Then, based on the measurements performed on the fabricated patterns, $R_{dome-glass}$ can be experimentally determined and an estimation can be done on the theoretical total reflectance that could be obtained by increasing the dome density. In figure 6.3, the theoretical calculated total reflectance of the PC pattern with respect to the dome density is reported, compared to the measurements performed on the prepared samples. From the simulation it can be seen how increasing the dome coverage area ϕ_{dome}, an increase in the total reflection at the wavelength peak is expected. For a high value of the surface coverage fraction, ϕ_{dome}= 80 %, the simulated peak reflectance reach a value of 26 %. This value is still lower compared to the data published in the reference literature.

The first explanation for this result can be formulated considering the main differences between the ink formulation and substrate properties used in the different works. In our case, the ink used to prepare the PC domes had a concentration of polystyrene particle of 10 % which was lower than the maximum concentrations of 15 % and 20 % reported in the reference papers (see subsubsection 4.2.2). A higher

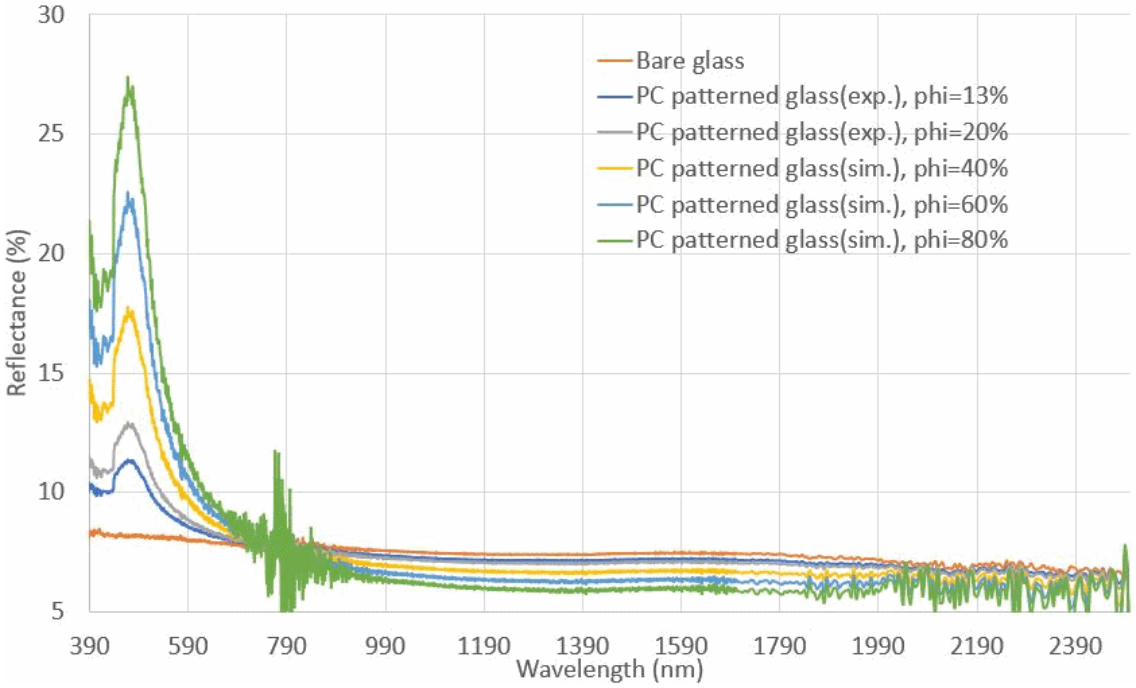

Figure 6.3: Simulated total reflectance based on the fraction of the substrate covered by PC domes (Phi, in %). The measured value are also reported for comparison.

particle concentration means that the number of particles contained in a single ink droplet will be higher so that, after the solvent evaporation, the self-assembling process will lead to PC domes having a bigger size, at the same substrate contact angle (see section 5.3). Another important factor is to be found in the substrate contact angle. From the analysis of the published literature, it was observed that the shape of the dome, i.e. the ratio between the height and the diameter of the domes, depends on the contact angle. If this can improve the crystalline quality of the PC, preventing the formation of coffee-ring aggregates, at the same time it can increase of the peak reflectance of the printed PC patterns (see subsubsection 4.2.2). Establishing a relation between the reflectance peak, the particle concentration of printed ink, and the contact angle between the ink and the substrate, is one of the directions for future tests and investigations.

From the microscope image reported in figure 6.2, some considerations on the structural quality of the printed PC pattern can be done. As expected from the analysed literature, the increased hydrophobicity of the glass substrate, achieved with the OTS treatment, cause the polystyrene particles to aggregate in hemispherical, highly ordered structures. The crystalline quality of the aggregates is confirmed by the fact that the domes clearly reflect light in the visible range, as already observed in the spectrometry measurements. Moreover, the particles are expected to aggregates in a FCC lattice, with the surface showing the hexagonal arrangement corresponding to the <111> planes. A remarkable confirmation is obtained considering the optical Bragg law introduced in subsubsection 4.2.1, where the wavelength at which the reflectance peak appears was expressed as a function of the particle dimension and

of the effective refractive index of the PC aggregates.

$$\lambda_{peak} = \frac{4D}{\sqrt{6}}\sqrt{n_{eff}^2 - \sin^2\theta_i} \tag{21}$$

Here D is the particle diameter, n_{eff} is the effective refractive index of the PC structure and θ_i is the incidence angle of the light. The effective refractive index was calculated with the Bruggeman model (see subsection 4.1), obtaining a value of n_{eff} = 1.4 while in our case the polystyrene particles had a diameter of 200 μm. The incidence angle was considered equal to 0°, since the samples were measured with near-normal incident angle. The Bragg law gives a value of the peak wavelength of λ_{peak} = 461 nm compared to the experimental value of 467 nm.

The macroscopic appearance of the solar cell covered with the PC pattern is shown in figure 6.4.

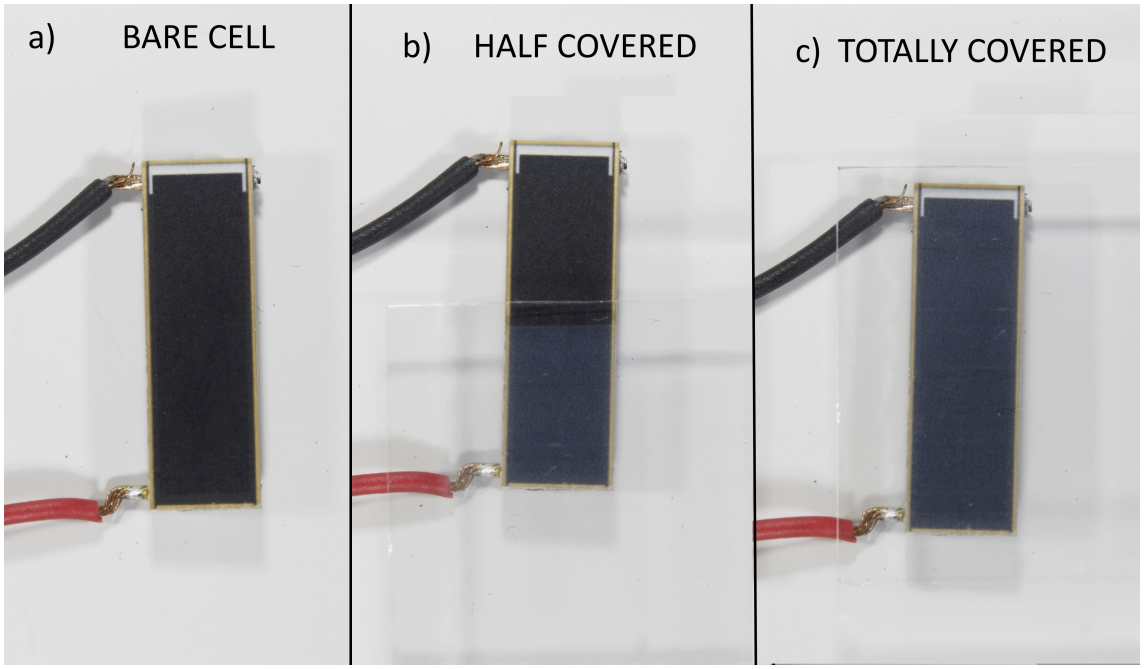

Figure 6.4: (a) Digital photograps of the bare Si solar cell used as reference, (b) of the solar cell half covered with the patterned glass substrate and (c) of the completely covered solar cell.

It can be seen how the patterned glass acts as a colouring filter for the solar cell. Visually, the covered regions appear grey-bluish, even if the saturation and brightness of the displayed colour are very low when compared to the much more promising results reported in the literature (sect subsection 4.2)

Starting from the measured reflectance spectra, and using the simulated spectra obtained by varying the dome coverage area, the RGB coordinates of the corresponding displayed colours were calculated. The resulting coordinates and corresponding colours are reported in figure 6.5, panels a-e. It can be observed how the increment in the dome coverage area (phi) causes the reflectance spectra to produce a cyanish colour with an increased saturation.

Moreover, if the effect of the glass substrate is eliminated from the measured reflectance spectra of the prepared PC pattern, the reflectance related only to the array of deposited material (without the glass) can be estimated and used to calculate the corresponding RGB coordinates. This was done considering that the total transmittance of the multi-material structure made by PC domes and glass substrate, can be estimated as:

$$T_{tot} = T_{domes} T_{glass} \tag{22}$$

where T_{tot} is the total transmittance of the structure, T_{domes} is the transmittance of the array of PC domes and T_{glass} is the transmittance of the glass substrate.Then, considering negligible absorbance so that the transmittance can be expressed as:

$$T = 1 - R \tag{23}$$

the reflectance of the domes will be:

$$R_{dome} = \frac{R_{tot} - R_{glass}}{1 - R_{glass}} \tag{24}$$

where R_{tot} is the total measured reflectance and R_{glass} is the measured reflectance of the bare glass substrate (see figure 6.1). The corresponding RGB coordinates and colour are reported in figure 6.5, panel f. This gives only a theoretical indication on what would be the expected colour of of a ideal layer layer of PC domes, as it was observed without any substrate. It is remarkable how this colour is very close to the

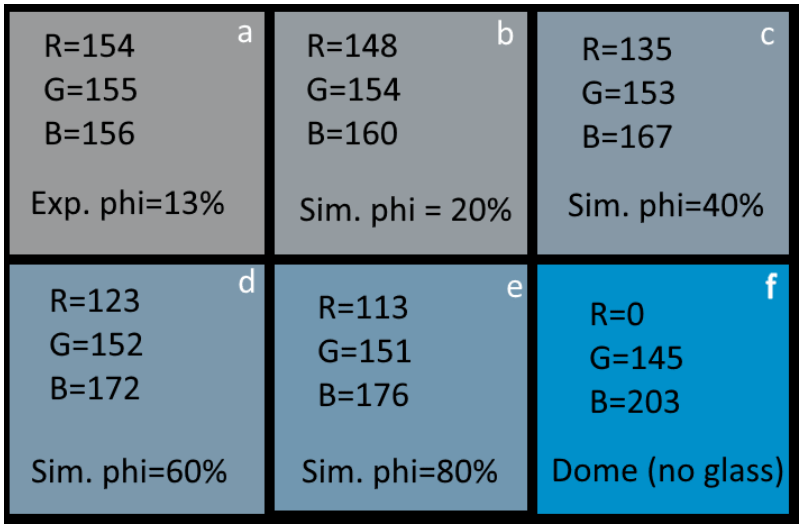

Figure 6.5: RGB colour coordinates corresponding to the measured reflectance of the PC patterns(a) and simulated reflectance(b-e) varying the dome coverage area (phi, in %). (f) RGB colour coordinates corresponding to the calculated reflectance spectra of the domes after the substrate effect was eliminated.

one displayed by the domes when observed with the optical microscope (figure 6.2).

Finally, the angle dependence of the optical properties of the printed PC pattern was investigated. Unfortunately the available spectrometer (UV-Vis-NIR Agilent

Cary 5000) did not allow to perform angle-dependent reflectance measurements so this feature was analysed qualitatively by observing the printed PC pattern at different viewing angles. In figure 6.6, microscopic images of the printed domes observed at two different angles are reported. It is clear how the colour of the printed

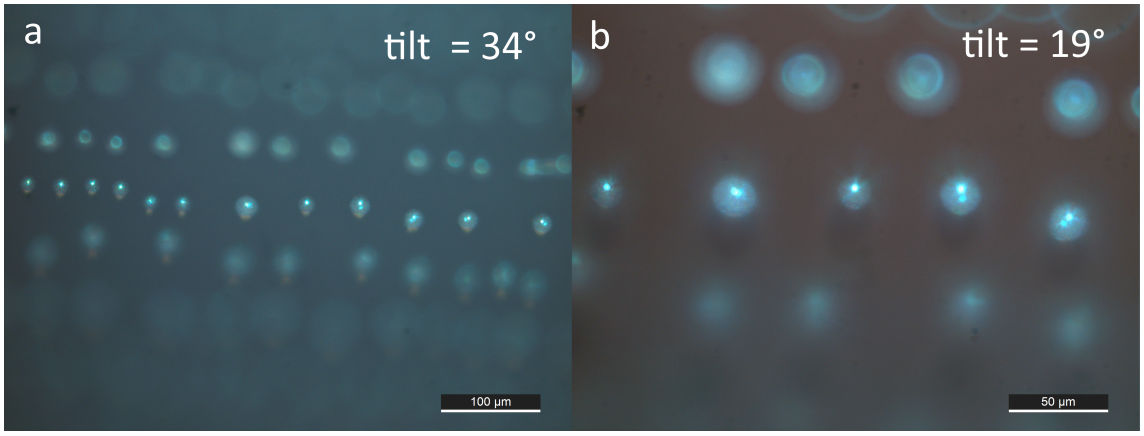

Figure 6.6: Optical microscope images of the PC patterned glass tilded by (a) 34° and (b) 19°. (note the different scales)

domes does not change if observed from different directions. At first sight, this evidence is in line with the expectation that the reflectance by the domes should be angle-independent, according to the reference literature. The same considerations can be done looking at the digital pictures of the PC patterned glass applied on the reference Si solar cell, taken at different angles (figure 6.7). The visual appearance remains the same at different tilting angles.

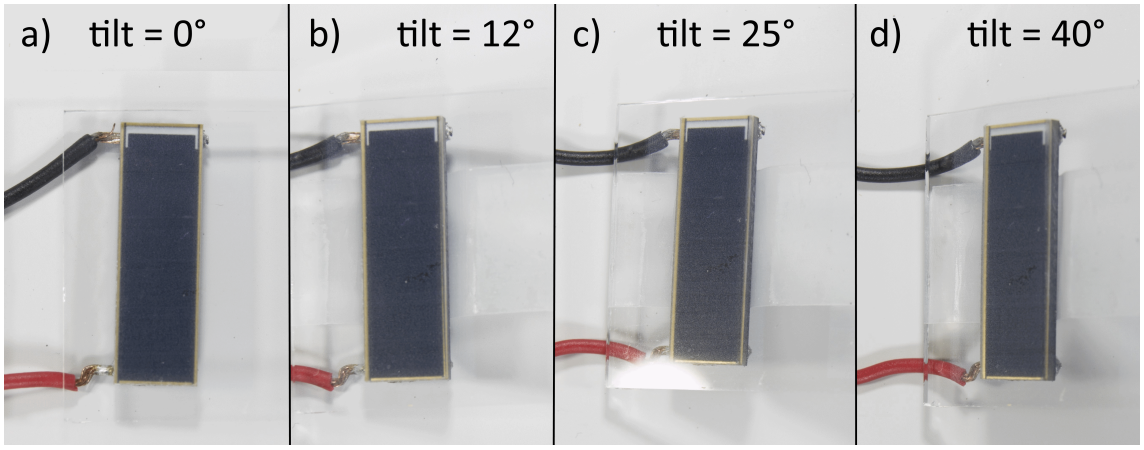

Figure 6.7: Photographs of the PC patterned glass applied on top of the reference Si solar cell, tilted by (a) 0°,(b) 12°,(c) 25°,(d) 40°

Electrical characterization of the m-Si solar cell integrated with the PC patterned glass To investigate the consequences on the electrical performance of a solar cell, when the PC patterned glass is applied as a colouring coating, EQE measurements were performed. In figure 6.8, the EQE of the bare reference m-Si solar cell as well as the EQE of the cell covered with the PC patterned glass and with the bare glass substrate are reported.

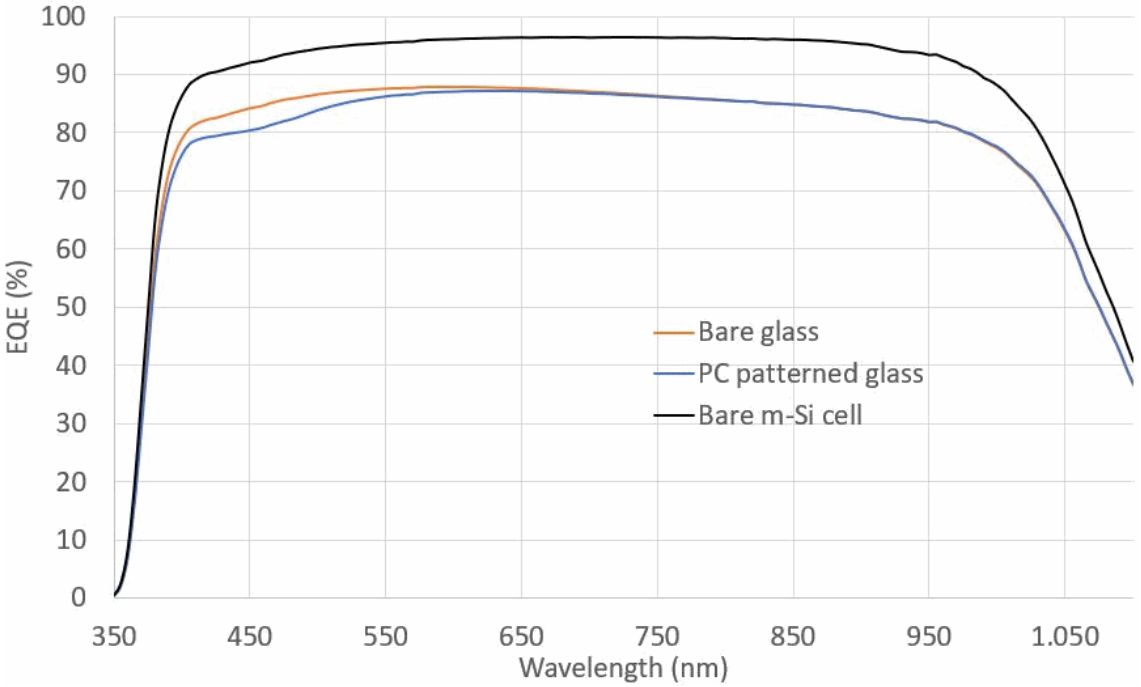

Figure 6.8: Measured EQE of the bare m-Si solar cell, the bare glass covered cell and the cell covered with the PC patterned glass.

As expected, the bare glass decreased EQE about 9 % in most of the visible range and in the near-UV, where the EQE is high, with a corresponding relative reduction of around 10 % in the estimated short circuit current density that reduces from 38.93 mA/cm^2 to 34.97 mA/cm^2. When the solar cell is covered with the PC patterned glass, an additional reduction in the EQE is observed for the wavelengths corresponding to the PC stop-band, where the reflectance has a peak. It is clear how the solar cell performance is not affected by the PC outside this range. The short circuit current of the coated m-Si cell reduces from 38.93 mA/cm^2 (bare cell) to 34.64 mA/cm^2, with a relative decrease of 11 %.

Finally, using the measured external quantum efficiency data, the reflectance of the bare glass and of the PC patterned sample have been calculated from:

$$R_x = 1 - T_x = 1 - \frac{EQE_x}{EQE_{SiCell}} \tag{25}$$

where the subscript x can refer to the PC patterned sample and to the bare glass substrate. Then, based on the same approximation done before (see equation 20), the reflectance spectra corresponding to different values of dome coverage areas

(phi) have been simulated. Figure 6.9 shows the comparison between the results (measured and simulated) obtained from the spectroscopy measurements reported in the previous section and the results (measured and simulated) obtained from the EQE measurements.

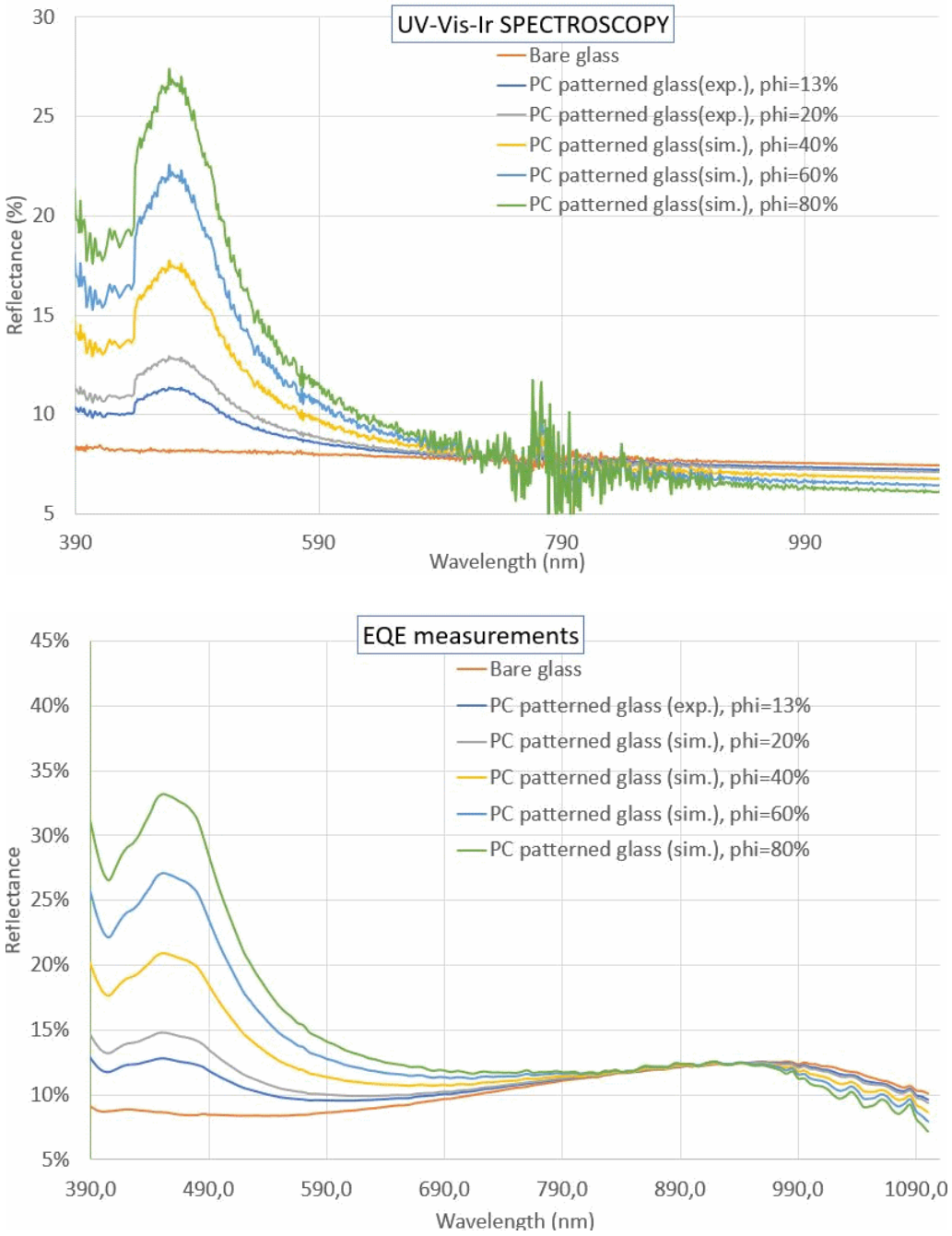

Figure 6.9: The measured and simulated reflectance spectra (at different dome coverage area, phi, in %) obtained from the spectroscopy measurements (top) and from the EQE measurements (bottom)

Comparing the two plots it can be observed that the results based on the spectroscopy measurements shows a reduction in the reflectance in the infrared region, as the coverage area is increased. On the other hand, the results obtained from the EQE measurements show a small reflectance peak in the same region. This difference it is expected since the two spectroscopy measurements have been carried on the PC patterned glass alone, while the EQE measurements refer the PC patterned glass applied on top of the m-Si solar cell. In general, in both cases the peak at the stopband position is clearly visible, confirming the theoretical expectations.

In order to estimate the effect of more densely occupied PC patterns on the performance of the solar cell, the data obtained from the EQE measurements have been used. Figure 6.10 shows the simulated variation of the EQE when the coverage area is increased, including the value of the measured EQE for comparison.

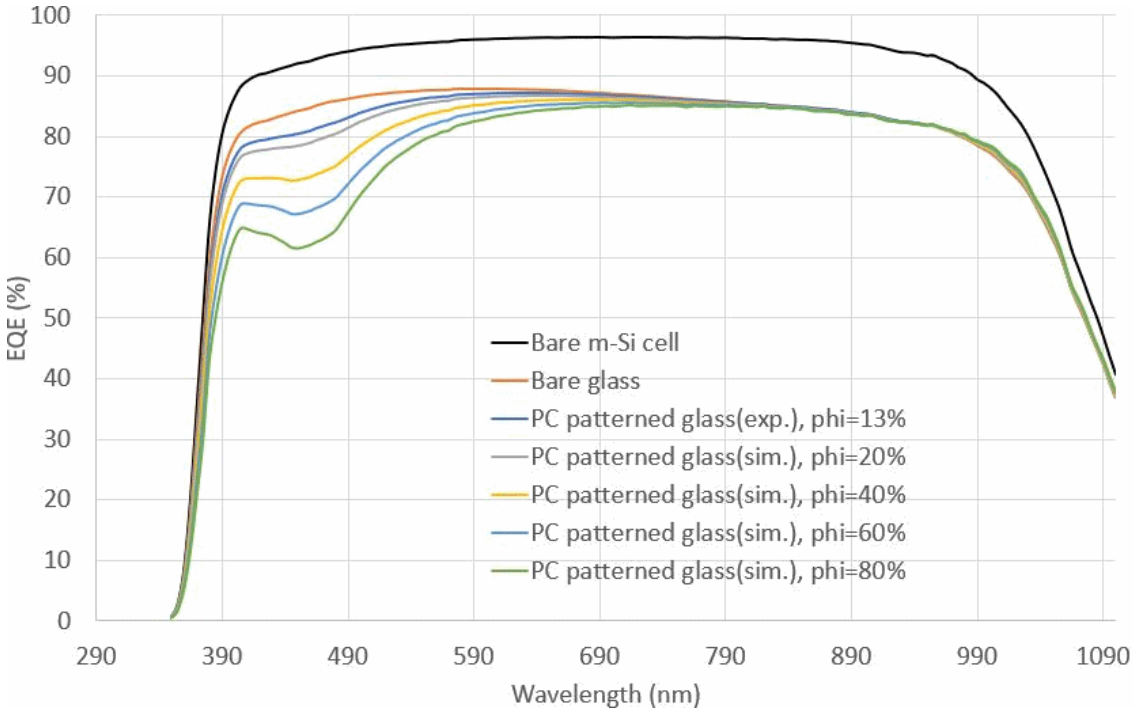

Figure 6.10: The simulated EQE of the solar cell covered with a PC patterned glass having different coverage area (phi, in %) is shown. The measured EQE for the bare m-Si solar cell the glass covered solar cell and the PC patterned covered solar cell (phi = 13 %) are also reported for comparison.

Dome coverage area [%]	Peak reflectance [%]	Simulated J_{sc} [mA/cm^2]	Measured J_{sc} [mA/cm^2]	ΔJ_{sc} [%]
Bare m-Si cell			38.93	
Bare glass			34.97	10
13	11.4		34.64	11
20	12.9	34.11		13
40	17.8	33.13		15
60	22.6	32.15		18
80	27.4	31.17		20

Table 2: Table representation of the deposition techniques as well as the material used to realize the layers composing the structure.

As expected, if the coverage area is increased, the simulation shows an increasing reduction in the EQE for the wavelengths corresponding to the PC stop-band. For the rest of the spectrum, the EQE remains very close to the measured values, confirming that the effect of the PC pattern is expected only at the stop-band wavelengths. With the simulated EQE spectra, it possible to calculate the expected reduction of the corresponding short circuit current. The results are shown in table 2. The simulation shows that maximizing the reflectance to 27.4 %, with a coverage area of 80 %, the short circuit current density would decrease to around 31.2 mA/cm^2, with a maximum relative loss of 20 %.

7 Summary and conclusions

The scope of this work to investigate the different proposed techniques to realize reflective colours for the fabrication of colourful solar cells. The importance of this topic is strictly related to the increasing interest in colourful photovoltaic for building-integrated applications. In particular, the ability to selectively change the visual appearance of a PV module, minimizing the performance loss to a minimum, is an highly required condition that would allow to realize multi-purpose PV devices that would work both as building materials (e.g. building façades and decorative elements) and as energy producing elements, contributing to the building energy efficiency.

Thanks to the advances in nanotechnology, in the literature, different techniques have been suggested to exploit the optical mechanisms of structural colours to produce reflective colour filters opposed to the common colouring techniques where light absorbing material are used (dyes or pigment). In general, the optical phenomena exploited can be divided in multi-layer interference, thin-film interference, light diffraction, plasmonic resonance and narrow-band reflectance in photonic crystals.

The most common solution is to realize a double-layer anti-reflective coating on top of a standard c-Si solar cell. By optimizing the thickness of the anti-reflective layers, the reflectance spectra of the final device can be tuned to achieve different colours. From the point of view of the device performance degradation due to the colour variation, with a maximum relative loss in the short circuit current density and power conversion efficiency of around 4 % with respect to the reference solar cell, it gives the best observable results among all the analysed techniques. This is mostly due to the fact that the device is obtained starting from a well-known standard c-Si solar cell, for which the power generation is stable and highly efficient. The obtained colour palette is strictly related to the corresponding reflectance spectra: peak reflectance in the visible range, between 10 % and 20 %, and visual appearance characterized by earth-like colours, which is a consequence of the presence of multiple peaks in the reflectance spectrum. While in many real life applications earth-like colours are preferred, there are also applications where high colour purity is desired, like digital printing.

Equally good results in terms of device performance were obtained by patterning the front surface of a heterojunction c-Si solar cell with an array of Si nanocylinders that showed a light scattering resonance peak in the visible range. Here the best final device showed a relative reduction in the short circuit current of 16 % with respect to the reference solar cell with corresponding relative reduction in the power conversion efficiency of 14 %. The tunability of the displayed colour depends on the geometric features of the realised Si nanocylinders array. A solar module with a bright green colour was reported.

Another solution proposed in the literature is to exploit the thin-film interference appearing in nanometric Fabry-Perot resonating structures. Here a completely personalized design was proposed, with the active material represented by a nanometric thin a-Si film. The fabricated device had an overall thickness of the order of micrometers, reducing notably the overall amount of material needed for the solar cell

fabrication. The proposed design showed a power conversion efficiency of 3 % with an a-Si layer thickness of 25 nm, compared to the reference value of 10 % obtained for a single-junction cell using a 250 nm thick, intrinsic a-Si layer as active material. Cyan, magenta and yellow cell were obtained showing a good level of colour purity and uniformity.

As in the previous case, again a personalised cell design was observed in the fabrication of colourful solar cells based on the integration of perovskite solar technology with nanoporous one-dimensional photonic crystals (1DPC). In this case the colour filtering comes from the ability of photonic crystal to reflect a narrow band of wavelength in the visible range, thanks to a periodic modulation of the refractive index of the structure. The nanoporous 1DPC were used as a scaffold for the perovskite active material and blue, green and orange devices were fabricated. The device performances showed a power conversion efficiency between 8.8 % and 6.6 % compared with the reference value for a perovskite solar cell of 10.5 %, with a relative reduction of 16 % and 37 %, respectively. The cells showed bright colours with a reasonably high level of colour purity.

Two other proposed techniques were analysed for which no electrical characterization was reported in the literature. One is the case of colouring a standard c-Si solar module by coating the surface with a layer of nanosized silver particles. The plasmonic resonance appearing at the interface between the metal nanoparticles and the dielectric substrate lead to the appearance of peaks in the reflectance spectra of the fabricated device, the position of which was directly dependent on the corresponding sputtering time. Yellow, green and brown earth-like colours were reported. Finally, the realization of a colouring front glass exploiting a design that reproduced the structural features observed in the Morpho butterfly's wings was reported. Here the reported device were highly promising in terms of colour uniformity and tunability and bright red, blue and green colour filters were shown. With this technique, it was reported that a relative loss in the power generation efficiency was around 7 %.

In the experimental part of the work, a new approach for realizing coloured solar cells was proposed, suggesting the realization of colour filters by inkjet printing of three dimensional photonic crystals. It was observed, from the literature review, that by realizing patterns of dome-shaped, highly ordered colloidal photonic crystals it is possible to tune the reflectance of the substrate by changing the diameter of the colloidal particles building the photonic crystals. As a proof-of-concept, a demonstration device was fabricated covering a monocrystalline silicon solar cell with a photonic crystal patterned glass. The device was optically and electrically characterized. It was observed that an optical filter can be realized with this technique, with a reflectance spectrum showing a peak in the visible wavelength region. The spectral position of the reflectance peak can be accurately defined based on the diameter of the particles used to build the PC. Based on the measurements performed on the device, it was estimated that a level of peak reflectance of around 26 % could be achieved by increasing the fraction of the substrate surface covered by the PC domes, compared to the experimental value of 11.3 %, with a corresponding relative reduction in the short circuit current density of 20% and 11%, respectively.

From the informations produced by the experimental work on dome-shaped PC

printed by ink-jet printing, it can be concluded that this technique represent a promising route for achieving non-absorbing colour filter for colourful photovoltaics. In particular, it is suggested that the single PC domes could be considered as the pixel of a digital image: by combining red, blue and green PC-based inks highly customizable digital images could be transferred on the cover of PV devices, massively improving the design freedom.

An exciting challenge future works could be to understand how the main features of the printed PC-domes (dimension, crystalline structure, shape) determine the brightness and saturation of the PC-based printed patterns.

References

[1] S. Lufkin E. Rey C. Ballif, L. Perret-Aebi. Integrated thinking for photovoltaics in buildings. *Nature Energy*, 3(6):438–442, 2018.

[2] F. Frontini E. Saretta M. Donker F. van den Vossen W. Folkerts I. Zanetti, P. Bonomo. Bipv-product overview for solar building skins-status report 2017. *BIPV-Building Integrated Photoboltaics*, 2017.

[3] Pveducation.org. https://www.pveducation.org. Accessed: 2018.

[4] Pvlightouse.com. https://www2.pvlighthouse.com.au/resources/courses/altermatt/The%20Solar%20Spectrum/The%20global%20standard%20spectrum%20(AM1-5g).aspx. Accessed: 2018.

[5] Sunpower.com. https://us.sunpower.com/sites/sunpower/files/media-library/spec-sheets/sp-sunpower-maxeon-solar-cells-gen3.pdf. Accessed: 2018.

[6] Mohamed El-Ahmar, Abou-Hashema M. El-Sayed, and Ashraf Hemeida. Mathematical modeling of photovoltaic module and evalute the effect of varoius paramenters on its performance. pages 741–746, 12 2016.

[7] Wikipedia.org. https://en.wikipedia.org/wiki/Theory_of_solar_cells. Accessed: 2018.

[8] Green Martin A., Hishikawa Yoshihiro, Dunlop Ewan D., Levi Dean H., Hohl-Ebinger Jochen, and Ho-Baillie Anita W.Y. Solar cell efficiency tables (version 51). *Progress in Photovoltaics: Research and Applications*, 26(1):3–12.

[9] Kiran Ranabhat, L Patrikeev, A.A. Revina, K Andrianov, Valery Lapshinsky, and Elena Sofronova. An introduction to solar cell technology. 14:481–491, 01 2016.

[10] Paul Calvert. Inkjet printing for materials and devices. *Chemistry of Materials*, 13(10):3299–3305, 2001.

[11] Singh Madhusudan, Haverinen Hanna M., Dhagat Parul, and Jabbour Ghassan E. Inkjet printing—process and its applications. *Advanced Materials*, 22(6):673–685.

[12] Alan Faulkner-Jones and Wenmiao (Will Shu. Biological cell printing technologies. 8:35–57, 03 2012.

[13] Kuang Minxuan and Song Yanlin. Inkjet printing of photonic crystals. pages 183–211, 2017.

[14] Slideshare.net. https://www.slideshare.net/biofabrication_unipi/2015-1112-inkjet-printing-part2-56368631. Accessed: 2018.

[15] Kinoshita Shuichi and Yoshioka Shinya. Structural colors in nature: The role of regularity and irregularity in the structure. *ChemPhysChem*, 6(8):1442–1459.

[16] Yuanjin Zhao, Zhuoying Xie, Hongcheng Gu, Cun Zhu, and Zhongze Gu. Bio-inspired variable structural color materials. *Chem. Soc. Rev.*, 41:3297–3317, 2012.

[17] Barbara Swatowska, T Stapinski, Kazimierz Drabczyk, and PIOTR PANEK. The role of antireflection coatings in silicon solar cells – the influence on their electrical parameters. XLI:487, 01 2011.

[18] Armin G Aberle. Overview on sin surface passivation of crystalline silicon solar cells. *Solar Energy Materials and Solar Cells*, 65(1):239 – 248, 2001. PVSEC 11 Part I.

[19] Hemant Kumar Raut, V. Anand Ganesh, A. Sreekumaran Nair, and Seeram Ramakrishna. Anti-reflective coatings: A critical, in-depth review. *Energy Environ. Sci.*, 4:3779–3804, 2011.

[20] Justin Henrie, Spencer Kellis, Stephen M. Schultz, and Aaron Hawkins. Electronic color charts for dielectric films on silicon. *Opt. Express*, 12(7):1464–1469, Apr 2004.

[21] Z. Feng P.P. Altermatt H. Shen Y. Chen, Y. Yang. Color modulation of c-si solar cells without significant current-loss by means of a double-layer anti-reflective coating. *27th European Photovoltaic Solar Energy Conference and Exhibition*, 2012.

[22] L Zeng, Y Chen, Wenjun Ge, and H Shen. Optimization of multi-layer antireflection coatings for multicrystalline silicon solar cells. 01 2012.

[23] J. Camassel and A. Tiberj. Strain effects in device processing of silicon-on-insulator materials. *Applied Surface Science*, 212-213:742 – 748, 2003. 11th International Conference on Solid Films and Surfaces.

[24] B Lenkeit, S Steckemetz, F Artuso, and R Hezel. Excellent thermal stability of remote plasma-enhanced chemical vapour deposited silicon nitride films for the rear of screen-printed bifacial silicon solar cells. *Solar Energy Materials and Solar Cells*, 65(1):317 – 323, 2001. PVSEC 11 Part I.

[25] Tadatsugu Minami, Tetsuharu Utsubo, Tsuyoshi Yamatani, Toshihiro Miyata, and Yoshiaki Ohbayashi. Sio2 electret thin films prepared by various deposition methods. *Thin Solid Films*, 426(1):47 – 52, 2003.

[26] A. El amrani, I. Menous, L. Mahiou, R. Tadjine, A. Touati, and A. Lefgoum. Silicon nitride film for solar cells. *Renewable Energy*, 33(10):2289 – 2293, 2008.

[27] Z. Chen, Z. Lv, and J. Zhang. Pecvd sio2/si3n4 double layers electrets on glass substrate. *IEEE Transactions on Dielectrics and Electrical Insulation*, 15(4):915–919, August 2008.

[28] Ebuka S. Arinze, Botong Qiu, Nathan Palmquist, Yan Cheng, Yida Lin, Gabrielle Nyirjesy, Gary Qian, and Susanna M. Thon. Color-tuned and transparent colloidal quantum dot solar cells via optimized multilayer interference. *Opt. Express*, 25(4):A101–A112, Feb 2017.

[29] Yifeng Chen, Yang Yang, Zhiqiang Feng, Pietro P Altermatt, and Hui Shen. Color modulation of c-si solar cells without significant current-loss by means of a double-layer anti-reflective coating. *27th EUPVSEC*, 2012.

[30] S. Seo e L. J. Guo K.-T. Lee, J. Y. Lee. Colored ultrathin hybrid photovoltaics with high quantum efficiency. *Light: Science & Applications*, 3:8e215, 2014.

[31] Verena Neder, Stefan L. Luxembourg, and Albert Polman. Efficient colored silicon solar modules using integrated resonant dielectric nanoscatterers. *Applied Physics Letters*, 111(7):073902, 2017.

[32] C. Prietl W. Waldhauser F. P. Wenzl G. Peharz, B. Grosschädl. Tuning the colors of c-si solar cells by exploiting plasmonic effects, 2016.

[33] M. Vaughan. *The Fabry-Perot Interferometer: History, Theory, Practice and Applications*. Series in Optics and Optoelectronics. Taylor & Francis, 1989.

[34] Seung Yeop Myong. Improvement of pin-type amorphous silicon solar cell performance by employing double silicon-carbide p -layer structure. 95:1525, 02 2004.

[35] Youjun He, Hsiang-Yu Chen, Jianhui Hou, and Yongfang Li. Indene-c60 bisadduct: A new acceptor for high-performance polymer solar cells. *Journal of the American Chemical Society*, 132(4):1377–1382, 2010. PMID: 20055460.

[36] J. Meyer, K. Zilberberg, T. Riedl, and A. Kahn. Electronic structure of vanadium pentoxide: An efficient hole injector for organic electronic materials. *Journal of Applied Physics*, 110(3):033710, 2011.

[37] Shah A. V., Schade H., Vanecek M., Meier J., Vallat-Sauvain E., Wyrsch N., Kroll U., Droz C., and Bailat J. Thin-film silicon solar cell technology. *Progress in Photovoltaics: Research and Applications*, 12(2-3):113–142.

[38] Kyu-Tae Lee, Sungyong Seo, Jae Yong Lee, and L. Jay Guo. Ultrathin metal-semiconductor-metal resonator for angle invariant visible band transmission filters. *Applied Physics Letters*, 104(23):231112, 2014.

[39] E. Vallat J. Meier U. Kroll J. Hötzel J. Bailat J. Steinhauser M. Marmelo G. Monteduro L. Castens S. Benagli, D. Borrello. High-efficiency amorphous silicon devices on lpcvd-zno tco prepared in industrial kai tm-m r-d reactor. *24th European Photovoltaic Solar Energy Conference, 21-25 September 2009, Hamburg, Germany*, pages 2293 – 2298.

[40] Mikhail A Kats, Romain Blanchard, Patrice Genevet, and Federico Capasso. Nanometre optical coatings based on strong interference effects in highly absorbing media. *Nature materials*, 12(1):20, 2013.

[41] Hui Joon Park, Ting Xu, Jae Yong Lee, Abram Ledbetter, and L Jay Guo. Photonic color filters integrated with organic solar cells for energy harvesting. *Acs Nano*, 5(9):7055–7060, 2011.

[42] Verena Neder, Stefan L. Luxembourg, and Albert Polman. Efficient colored silicon solar modules using integrated resonant dielectric nanoscatterers. *Applied Physics Letters*, 111(7):073902, 2017.

[43] Mie Gustav. Beiträge zur optik trüber medien, speziell kolloidaler metallösungen. *Annalen der Physik*, 330(3):377–445.

[44] Qian Zhao, Ji Zhou, Fuli Zhang, and Didier Lippens. Mie resonance-based dielectric metamaterials. *Materials Today*, 12(12):60 – 69, 2009.

[45] Andrey E. Miroshnichenko Leonid A. Krivitsky Yuan Hsing Fu Vytautas Valuckas Leonard Gonzaga Yeow Teck Toh Anthony Yew Seng Kay Boris Luk'yanchuk Arseniy I. Kuznetsov Ramón Paniagua-Domínguez, Ye Feng Yu. Generalized brewster effect in dielectric metasurfaces. *Nature Communications*, 7(10362), 2016.

[46] J. van de Groep and A. Polman. Designing dielectric resonators on substrates: Combining magnetic and electric resonances. *Opt. Express*, 21(22):26285–26302, Nov 2013.

[47] C. Prietl W. Waldhauser F. P. Wenzl G. Peharz, B. Grosschädl. Tuning the colors of c-si solar cells by exploiting plasmonic effects. *Proc.SPIE*, 9937:9937 – 9937 – 8, 2016.

[48] Wei Zhang, Miguel Anaya, Gabriel Lozano, Mauricio E. Calvo, Michael B. Johnston, Hernán Míguez, and Henry J. Snaith. Highly efficient perovskite solar cells with tunable structural color. *Nano Letters*, 15(3):1698–1702, 2015. PMID: 25650872.

[49] James M. Ball, Michael M. Lee, Andrew Hey, and Henry J. Snaith. Low-temperature processed meso-superstructured to thin-film perovskite solar cells. *Energy Environ. Sci.*, 6:1739–1743, 2013.

[50] Silvia Colodrero, Manuel Ocaña, and Hernán Míguez. Nanoparticle-based one-dimensional photonic crystals. *Langmuir*, 24(9):4430–4434, 2008. PMID: 18366232.

[51] Miguel Anaya, Gabriel Lozano, Mauricio E. Calvo, Wei Zhang, Michael B. Johnston, Henry J. Snaith, and Hernán Míguez. Optical description of mesostructured organic–inorganic halide perovskite solar cells. *The Journal of Physical Chemistry Letters*, 6(1):48–53, 2015. PMID: 26263090.

[52] Daniele Colonna, Silvia Colodrero, Henrik Lindström, Aldo Di Carlo, and Hernán Míguez. Introducing structural colour in dscs by using photonic crystals: interplay between conversion efficiency and optical properties. *Energy & Environmental Science*, 5(8):8238–8243, 2012.

[53] Benedikt Bläsi, Thomas Kroyer, Oliver Höhn, Martin Wiese, Claudio Ferrara, Ulrich Eitner, and Tilmann Kuhn. Morpho butterfly inspired coloured bipv modules. 09 2017.

[54] Shuichi Kinoshita, Shinya Yoshioka, Yasuhiro Fujii, and Naoko Okamoto. Photophysics of structural color in the morpho butterflies. 2002.

[55] Kyungjae Chung, Sunkyu Yu, Chul-Joon Heo, Jae Won Shim, Seung-Man Yang, Moon Gyu Han, Hong-Seok Lee, Yongwan Jin, Sang Yoon Lee, Namkyoo Park, and Jung H Shin. Flexible, angle-independent, structural color reflectors inspired by morpho butterfly wings. *Advanced materials (Deerfield Beach, Fla.)*, 24(18):2375—2379, May 2012.

[56] Jonathan M. Blackledge. Chapter 6 - scattering theory. pages 160 – 197, 2005.

[57] Otto Glatter. Chapter 10 - light scattering from large particles: Lorenz-Mie. pages 187 – 221, 2018.

[58] J.D.Joannopoulos , R.D.Meade , and J.N.Winn . *Photonic Crystals: Molding The Flow of Light*. 01 1995.

[59] Andreas Othonos. Fiber bragg gratings. *Review of Scientific Instruments*, 68(12):4309–4341, 1997.

[60] Peter Vukusic. Photonic structures in biology. 10 2004.

[61] Geoffrey A Ozin, André Arsenault, and Ludovico Cademartiri. *Nanochemistry*. The Royal Society of Chemistry, 2008.

[62] Jr. title = Duane M. Moore, Robert C. Reynolds.

[63] A. Reynolds, F. López-Tejeira, D. Cassagne, F. J. García-Vidal, C. Jouanin, and J. Sánchez-Dehesa. Spectral properties of opal-based photonic crystals having a sio_2 matrix. *Phys. Rev. B*, 60:11422–11426, Oct 1999.

[64] Takashi Yamasaki and Tetsuo Tsutsui. Spontaneous emission from fluorescent molecules embedded in photonic crystals consisting of polystyrene microspheres. *Applied Physics Letters*, 72(16):1957–1959, 1998.

[65] C.Lopez, L.Vazquez, F.Meseguer, R.Mayoral, M.Ocana, and H.Miguez. Photonic crystal made by close packing sio2submicron spheres. *Superlattices and Microstructures*, 22(3):399 – 404, 1997.

[66] A. Richel, N. P. Johnson, and D. W. McComb. Observation of bragg reflection in photonic crystals synthesized from air spheres in a titania matrix. *Applied Physics Letters*, 76(14):1816–1818, 2000.

[67] Khardani M., Bouaïcha M., and Bessaïs B. Bruggeman effective medium approach for modelling optical properties of porous silicon: comparison with experiment. *physica status solidi c*, 4(6):1986–1990.

[68] Ling Bai, Zhuoying Xie, Wei Wang, Chunwei Yuan, Yuanjin Zhao, Zhongde Mu, Qifeng Zhong, and Zhongze Gu. Bio-inspired vapor-responsive colloidal photonic crystal patterns by inkjet printing. *ACS Nano*, 8(11):11094–11100, 2014. PMID: 25300045.

[69] H. Nam, K. Song, D. Ha, and T. Kim. Inkjet-printing-based structural coloring for anti-counterfeit applications. pages 1417–1420, June 2015.

[70] Ling Bai, Zhuoying Xie, Wei Wang, Chunwei Yuan, Yuanjin Zhao, Zhongde Mu, Qifeng Zhong, and Zhongze Gu. Bio-inspired vapor-responsive colloidal photonic crystal patterns by inkjet printing. *ACS nano*, 8(11):11094–11100, 2014.

[71] Jungho Park, Jooho Moon, Hyunjung Shin, Dake Wang, and Minseo Park. Direct-write fabrication of colloidal photonic crystal microarrays by ink-jet printing. *Journal of Colloid and Interface Science*, 298(2):713 – 719, 2006.

[72] Liying Cui, Yingfeng Li, Jingxia Wang, Entao Tian, Xingye Zhang, Youzhuan Zhang, Yanlin Song, and Lei Jiang. Fabrication of large-area patterned photonic crystals by ink-jet printing. *J. Mater. Chem.*, 19:5499–5502, 2009.

[73] Kuang Minxuan, Wang Jingxia, Bao Bin, Li Fengyu, Wang Libin, Jiang Lei, and Song Yanlin. Inkjet printing patterned photonic crystal domes for wide viewing-angle displays by controlling the sliding three phase contact line. *Advanced Optical Materials*, 2(1):34–38.

[74] Jingxia Wang, Libin Wang, Yanlin Song, and Lei Jiang. Patterned photonic crystals fabricated by inkjet printing. *J. Mater. Chem. C*, 1:6048–6058, 2013.

[75] Jonathan G. McGrath, Robert D. Bock, J. Michael Cathcart, and L. Andrew Lyon. Self-assembly of "paint-on" colloidal crystals using poly(styrene-co-n-isopropylacrylamide) spheres. *Chemistry of Materials*, 19(7):1584–1591, 2007.

[76] Jingxia Wang, Libin Wang, Yanlin Song, and Lei Jiang. Patterned photonic crystals fabricated by inkjet printing. *J. Mater. Chem. C*, 1:6048–6058, 2013.

[77] Hwa-Young Ko, Jungho Park, Hyunjung Shin, and Jooho Moon. Rapid self-assembly of monodisperse colloidal spheres in an ink-jet printed droplet. *Chemistry of Materials*, 16(22):4212–4215, 2004.

[78] Jungho Park and Jooho Moon. Control of colloidal particle deposit patterns within picoliter droplets ejected by ink-jet printing. *Langmuir*, 22(8):3506–3513, 2006. PMID: 16584221.

[79] Jungho Park and Jooho Moon. Control of colloidal particle deposit patterns within picoliter droplets ejected by ink-jet printing. *Langmuir*, 22(8):3506–3513, 2006. PMID: 16584221.

[80] Gu Hongcheng, Zhao Yuanjin, Cheng Yao, Xie Zhuoying, Rong Fei, Li Jiaqi, Wang Baoping, Fu Degang, and Gu Zhongze. Tailoring colloidal photonic crystals with wide viewing angles. *Small*, 9(13):2266–2271.

[81] Fujifilmusa.com. http://www.fujifilmusa.com/products/industrial_inkjet_printheads/deposition-products/dmp-2800/index.html. Accessed: 2018.

[82] Polysciences.com. http://www.polysciences.com/default/polybead-microspheres-020956m. Accessed: 2018.